Summer 2017

# Advanced analytical strategies to determine biomedical parameters for medical diagnostics, drug delivery, and therapy

Sisi Chen

# ADVANCED ANALYTICAL STRATEGIES TO DETERMINE BIOMEDICAL PARAMETERS FOR MEDICAL DIAGNOSTICS, DRUG DELIVERY, AND THERAPY

by

SISI CHEN

A DISSERTATION

Presented to the Faculty of the Graduate School of the

MISSOURI UNIVERSITY OF SCIENCE AND TECHNOLOGY

In Partial Fulfillment of the Requirements for the Degree

DOCTOR OF PHILOSOPHY

in

CHEMISTRY

2017

Approved by

Dr. Klaus Woelk, Advisor

Dr. Paul Nam

Dr. Jeffrey Winiarz

Dr. Vadym Mochalin

Dr. Richard Brow

## PUBLICATION DISSERTATION OPTION

Part of this dissertation consists of the following two articles that have been published as follows:

Page 13-35 has been published in Sensors and Actuators B: Chemical.

Page 36-59 has been published in Analytical Methods.

## ABSTRACT

Biomedical parameters are critical for diseases prognosis, diagnosis and therapy. Many research groups have dedicated their studies to develop analytical instrumentation and apply analytical methods to determine biomedical parameters that have the potential to help with disease control and increase public health. This dissertation focuses on three major aspects of analytical strategies development and applications: 1) detection of pH changes caused by nanotoxicity (induced by $TiO_2$ nanoparticles) using newly developed micro-pH sensor, 2) quantification of renal cell carcinoma (RCC) biomarkers by high-performance liquid chromatography – tandem mass spectrometry (HPLC-MS/MS), and 3) nuclear magnetic resonance (NMR) studies of porous wall hollow glass microspheres (PWHGMs) that have the potential to be used as drug delivery carriers. Firstly, a dual-core fiber-optic pH micro-probe was developed which can be used within the biologically relevant pH range from 6.20 – 7.92 ($R^2$ = 0.9834). Secondly, a targeted HPLC-MS/MS protocol was developed to simultaneously monitor four urinary biomarkers for RCC and applied to human urine specimen analysis. Thirdly, a vacuum-based loading system was developed to charge PWHGMs with specific materials followed by a washing procedure. Immiscible binary model systems (n-dodecane/water and chloroform/water) as well as isopropanol- acetic acid esterification and the hydrolysis of isopropyl acetate were investigated to obtain NMR evidence for material loading into PWHGMs and their subsequent release into the surrounding solutions. In addition, microspheres loaded with $H_2O$ were suspended in $D_2O$ to obtain quantitative information about the release kinetics from PWHGMs. The results demonstrate that NMR is a particularly useful tool to study developments and applications of PWHGMs in the targeted and controlled drug delivery.

# ACKNOWLEDGEMENTS

I would like to express my sincere gratitude and respect to my advisor, Dr. Klaus Woelk. Without his continuous support, this dissertation would never be possible. He always ensured that I learned the basic knowledge for my studies, developed appropriate laboratory and research skills, and enhanced my ability for critical thinking and problem solving. I deeply thank him for providing great help and support when I felt frustrated and encouraging me to pursue my goal. His guidance in all aspects of my graduate work was invaluable and will always be appreciated. He is the best advisor that I have ever met.

I would also like to thank my committee members Dr. Paul Nam, Dr. Jeff Winiarz, Dr. Vadym Mochalin, and Dr. Richard Brow for their professional knowledge and support on analytical techniques as well as in the materials sciences. Their great advice, suggestions and support during my Ph.D. research work and life are deeply appreciated.

I would like to express my deepest thanks and respect to Dr. Rex II Gerald. He is a great scientist from whom I learned a lot not only in science but also for my life. I also thank Dr. Jie Huang for establishing the collaborations with MoSci.

I would like to thank the Administrative Assistants of the Chemistry Department, who were constantly eager to help with the formal process of my Ph.D. degree, and provided timely information.

At last, I am deeply, sincerely grateful to my family, especially to my dearest mom, Lili Chen. Without her continuous care, support, encouragement, and love, I would have never been successful in pursuing a Ph.D. degree. I would also like to thank all my friends, especially my significant other Jiaming Geng, for their help and support. My life and my Ph.D. work would have never been this joyful and meaningful without them.

# TABLE OF CONTENTS

Page

SECTION

# LIST OF ILLUSTRATIONS

# LIST OF TABLES

PAPER II Page



SECTION

# NOMENCLATURE

| Symbol | Description |
|---|---|
| $H_2O$ | water |
| $D_2O$ | deuterium oxide (deuterated water) |
| $CHCl_3$ | chloroform |
| $C_{12}H_{26}$ | n-dodecane |
| $CH_3COOH$ | acetic acid |
| $(CH_3)_2CHOH$ | isopropanol |
| $H_2SO_4$ | sulfuric acid |
| $(CH_3)_2CHOOCCH_3$ | isopropyl acetate |

# 1. INTRODUCTION

## 1.1. ADVANCED ANALYTICAL STRATEGIES IN BIOMEDICAL STUDIES

Biomedical studies are a dynamic and challenging area that is highly relevant to the understanding and treatment of human diseases. It involves research from disease diagnosis to therapy, focusing on the interaction between cells, molecules, and organs. Scientists have been contributing with every possible effort to solve biomedical issues and problems with various analytical instruments and techniques. Conventional analytical instruments, such as high-performance liquid chromatography coupled with mass spectrometry (HPLC-MS) or tandem mass spectrometry (HPLC-MS/MS), gas chromatography coupled with mass spectrometry (GC-MS) or tandem mass spectrometry (GC-MS/MS), nuclear magnetic resonance (NMR) spectroscopy and others have been widely applied in biomedical studies. For example, with its advantages of high efficiency, high throughput, and ultra-high sensitivity, HPLC-MS and HPLC-MS/MS are leading the way in studies for antihypertensive treatment [1], proteomics [2], metabolomics [3], and biomarker discovery [4]. GC-MS and GC-MS/MS are state-of-art instrumentation techniques that are applied in many areas of biomedical studies such as pharmacokinetics [5], drug delivery [6]. NMR spectroscopy is a very powerful tool for elucidating the structures and dynamics of both small and large molecules (even macro-molecules) [7]. In biomedical research and medical diagnostics, NMR spectroscopy has been widely used in the form of magnetic resonance imaging (MRI), which offers valuable information on disease diagnosis and evaluation [8]. Although all of these techniques have their specific advantages and disadvantages, several studies report how they can be applied to

complement each other in biomedical studies [9-11]. Meanwhile, there are emerging new and innovative technologies and techniques that are intended to solve very specific biomedical problems. Fiber optic sensors (FOS) for example have been attracting considerable interest due to the effect that physical or chemical parameters can change the properties of light propagating in the fiber. The high elasticity and small size allow designing miniaturized FOS with metrological characteristics (e.g., accuracy, sensitivity, and frequency response) adequate for most common biomedical applications [12].

## 1.2.IMPORTANCE OF NICHE CELLULAR ENVIRONMENT PH MEASUREMENT IN DISEASE DIAGNOSIS

The human body is designed to maintain a very delicate pH balance in its fluid, tissues and systems. Even though most biological reactions essential to life take place in an aqueous environment, the blood plasma and interstitial fluids surrounding the cells are most sensitive to pH imbalance. When pH of these fluids is maintained within a narrow range of 7.35 to 7.45, our body's immune system is operating in optimal conditions and is able to fight off illness and disease. Moreover, enzymes that catalyze the chemical reactions of life require a specific pH in order to function, and if the pH is imbalanced significantly, biochemical like proteins can be denatured and become non-functional, resulting in diseases or death. Organisms are composed of many different type of cells and one of the most important mechanism that helps pH balance is the buffer system inside the cytoplasm of cells [13]. To better and thorough understand diseases and biomedical cases, studies can be done narrowly down to cellular level. Therefore, measurement of parameters at cellular level is highly important. Among all cellular

parameters, cytosolic proton concentration (e.g. pH) has been acknowledged as an indicator for fundamental cellular events, because many biology processes are pH sensitive, such as cell differentiation, division, migration and death [14-16]. In the complement, cellular pH will change or dysregulate if cells undergo abnormal processes, such as external stimuli (i.e. toxic materials), cancer development. Therefore, pH measurement is critical to understand cell behaviors and predict any irregular events. Cellular pH is regulated through different antiports and symports [17]. The NHEs are a family of membrane proteins and play a crucial role in many biological processes [18], including pH regulation. Other regulators, such as $Cl^-/HCO_3^-$ antiports, $HCO_3^-/Na^+$ symports, are also essential for intracellular pH regulation. The dysfunction of these regulators will lead to pH dysregulation and thus cause disease or death. Therefore, accurate, real-time pH measurements are key to further understand cell behaviors, and eventually benefit disease prognosis and treatment.

## 1.3.THE IMPORTANCE OF BIOMARKERS FOR DIAGNOSIS AND THERAPY

The definition of biomarker has evolved over the past decades, and the World Health Organization has now broadly defined them as "A biomarker is any substance, structure or process that can be measured in the body or its products and influence or predict the incidence of outcome or disease" [19]. More specific for medical studies, the National Cancer Institute has defined a biomarker as "a biological molecule found in blood, other body fluids, or tissues that is a sign of a normal or abnormal process or of a condition or disease". In clinical studies, biomarkers are often identified as indicators of the presence, severity, or state of a disease, which renders them important in medical

research. As such, biomarkers typically differentiate an affected patient from a person without the disease. Consequently, biomarkers can be present in many different forms, including particular proteins or peptides [20-24], antibodies [25-28], cell types [29-32], metabolites [33-36], lipids [37-39], hormones [40-42], enzyme levels [43-45], and physiological states [46, 47]. However, biomarkers can also be used to evaluate the effectiveness of therapies with regard to mediating the adverse effects of a disease. For example, using biomarkers to monitor the response of patients to a specific drug, it is possible to determine whether the treatment of the disease is effective. This information could result in a valuable early detection of negative drug response or could potentially bring enhancement in drug efficiency to patients. Ultimately and most importantly, biomarkers are used to detect changes in physiological conditions that correlate with the risk, progression, or remediation of a disease [23, 48-50]. In addition to prognosis and diagnosis of biomarkers, they can also be used for local and targeted therapy. For example, interleukin-33 (IL-33) is a functional ligand for ST2, a member of the interleukin-1 receptor family. IL-33/ST2 is a promising cardiovascular biomarker with a newly proposed mechanism of communication between intramyocardial fibroblast–cardiomyocyte [51]. This may be a therapeutic target to slow down the rate of further heart failure. Another example is Bevacizumab, a MoAb binding vascular endothelial growth factor (VEGF) that has been reported as an effective molecule for treatment of ovarian cancer [52]. Therefore, biomarkers can be directly delivered to target tissues or body sites for disease therapeutic effects to obtain high efficiency disease treatments.

Many efforts have been devoted to the discovery and determination of biomarkers in biological samples and tissues [53]. Mass spectrometry (MS) has been extensively

used as a diagnostic tool in clinical laboratories for many decades. When it is applied in biomarker discovery, it is largely used in proteomic studies [54, 55]. MS can provide accurate mass to charge ratios for different fragments of biomarkers. In addition, different types of mass analyzers can further assess each fragment, providing valuable proteomic-pattern information that makes it possible to discriminate between diseased patients and healthy individuals. Other analytical techniques such as nuclear magnetic resonance (NMR) spectroscopy [56, 57], are also being used in biomarker discovery and quantification.

## 1.4.THE DEVELOPMENT OF DRUG DELIVERY SYSTEM FOR IMPROVEMENT IN DISEASE THERAPY

Drugs have been used to improve human health for many centuries if not millennia. The application of targeted drug delivery to specific infected sites has significantly changed in the past decades and is expected to have an even greater impact in the future. Targeted drug delivery systems are engineered technologies for specific and controlled drug delivery of therapeutic agents [58]. The development of drug delivery system is to reduce the side effects that drugs may have on healthy tissues, which often prevents the optimal medication for diseases such as cancer [59], neurodegenerative disease [60], and infectious diseases [61]. Traditional drugs may be taken orally, by inhalation or injection, or by absorption through the skin. Each method has advantages and disadvantages and, for a specific disease, not all methods can be applied for the available medication. Therefore, improvements of current delivery methods, or targeted delivery alternatives to these methods are of particularly interest to research and development. Nanotechnology is emerging as a novel platform for drug delivery and is

widely expected to change the landscape of biotechnology for the foreseeable future [62-64]. Several delivery vehicles have been designed based on nanomaterials such as liposomes [65], polymers [66], nanotubes [67], and nanoparticles [68]. The newly developed vehicles for drug delivery should achieve several goals such as improving the delivery of poorly water-soluble drugs [69], the delivery of drugs to target sites or specific tissues [70], or the co-delivery of two or more drugs for combination therapy [71]. With regards to all of these merits, the newly designed drug delivery systems aim to largely improve the accuracy of delivery, the efficiency of therapies, and the time for recovery.

## 1.5.APPLICATIONS OF MICROSPHERES IN CANCER TREATMENT

Cancer is a disease in which abnormal cells grow fast and have the potential to invade other tissues or sites. The American Cancer Society reported that cancer is the second leading cause of death and it has been a worldwide disease that has attracted researchers' attention for many several decades. Scientists have been contributing with every effort to find solutions for cancer treatments. Traditional cancer treatments with anticancer drugs have limitations because of their lack of selectivity for tumor tissue and often cause side effects resulting in reduced cure rates. Consequently, targeted therapies have become more significant for cancer treatment, which can reduce side effects and increase the effectiveness of cure. Cancer microspheres technology is emerging as a novel and up-to-date methodology in cancer treatment [72]. There are many advantages of microspheres, such as targeted delivery of drugs and treatment directly at desired sites. The targeted treatment is achieved by a very specific size of the microspheres relative to

the blood vessels of the targeted organ. For example, glass microspheres are used as vehicles to treat liver cancer with radiation. Yttrium-90 (Y-90) doped glass microspheres are increasingly used for liver cancer treatment [73, 74]. Y-90 microspheres have two forms: one is composed of tiny glass beads embedded with Y-90 (TheraSphere®) whereas the other is composed of tiny polymer beads filled with Y-90 (SIR-Spheres®). Both types of microspheres have been approved by the Food and Drug Administration (FDA) in 1999 and 2002 respectively [75]. They function as emitters of beta particles that penetrate 2.5 mm into the surrounding tissue and have 2.6-day half-life [76]. The sizes of Y-90 microspheres are typically 20 – 60 μm in diameter. They are applied by infusion via the hepatic artery and preferentially lodge in the tumor's blood vessels, while sparing normal tissue which typically has larger blood vessels [77]. Microspheres have also been used for other types of cancers, such as breast cancer [78], colorectal cancer [79], lung cancer [80], ovarian cancer [81], bladder cancer [82] and others. Therefore, microspheres are an efficient carrier system for treatments of many types of cancers and can be tailored for very specific targeted treatments.

## 1.6.POROUS WALL HOLLOW GLASS MICROSPHERES

Biomaterials have been playing a pivotal role in biomedical research during recent years. Among the different types of biomaterials, certain glass materials are known to be biocompatible and have been used safely in applications requiring permanent implantation [83]. Since the first generation of such glass materials was developed in the 1960s, they have been widely used in dental [84], orthopedic [85, 86], and tissue engineering applications [87, 88]. Recently, more studies have focused on the "third

generation" of glass materials, which are designed for therapies to achieve tissue regeneration and tissue repair without invasive surgery [89]. Glass materials have also been proposed as delivery system for drugs [90], growth factors [91], and proteins [92]. Biocompatible glass microspheres are spherical particles with diameters in the micrometer range. Recently, porous-wall hollow glass microspheres (PWHGMs) have attracted the interest of researchers due to their specifically engineered hollow-cavity $SiO_2$ structure that consists of 1-μm thick porous walls [93]. The centers of the hollow cavities can be filled with different materials for various applications. PWHGMs were originally fabricated to be used by the Department of Energy (DOE) for national security and energy applications, as well as waste management and environmental remediation projects [93, 94]. Because of their unique properties, such as high and controllable permeability, low density, the storage cavity and large surface area, PWHGMs have been used in storage batteries [95], material adsorption [96], gas sensors [97], hydrogen storage [98], security technology [99] and others. The pores (i.e., open channels) in the wall and the hollow cavities of PWHGMs render them a potential vehicle for drug delivery [100], and more recent studies have reported the use of PWHGMs for biomedical applications, especially for cancer therapy [100, 101]. In addition to drug delivery applications, the hollow cavities of microspheres can serve as containers for biomarkers to achieve targeted delivery for specific prognosis and diagnosis of diseases.

## 1.7.NUCLEAR MAGNETIC RESONANCE (NMR) SIGNIFICANCE IN THE STUDIES OF PWHGMS

PWHGMs were characterized largely by optical microscopy, scanning electron microcopy (SEM) [102], transmission electron microcopy (TEM) [103], confocal laser

scanning microscopy (CLSM) [104], and dynamic light scattering [104]. However, these techniques only provided the characterization of the surface, shell thickness, and pore sizes of PWHGMs. To obtain information about what has been loaded inside the cavities of PWHGMs for targeted biomarker and drug delivery, an analytical technique is needed that can provide specific information about the loaded materials and its releasing kinetics. NMR spectroscopy is one of the most powerful analytical tools and it is widely used in pharmaceutical [105], biomedical [106] and chemical investigations in industry and academia. Unequivocal analytical evidence can be provided from NMR spectra, such as chemical structures, dynamics, and conformational information [107], which makes NMR stand out ahead of many other techniques. In addition, most NMR techniques are inherently quantitative as signal intensities are directly related to the number of nuclei under investigation. Unlike other commonly used analytical techniques, sample preparation for NMR spectroscopy is generally simple and no sample separation such as in high performance liquid chromatography (HPLC) or gas chromatography (GC), is needed. Moreover, NMR is a non-destructive technique and thus is most suitable for kinetic studies and analyses [108]. NMR spectroscopic techniques have been widely used in drug discovery, where detailed insights into interactions between molecules and a matrix is desired [109]. However, no NMR study on PWHGMs and their potential use in targeted drug or biomarker delivery is known. With the fundamental advantages of NMR and its versatility, more valuable information can be acquired from NMR spectra to fully evaluate the applicability of PWHGMs in targeted biomedical applications.

## 1.8.RESEARCH OBJECTIVES

This work aims to utilize several advanced analytical techniques, including traditional instruments and self-developed novel technique, to measure/determine medical parameters using in biomedical studies. These are achieved through three projects listed as following:

1. Designed and fabricated dual-core fiber-optic pH micro-probe used to measure pH value in niche environment where cells were treated with $TiO_2$ nanoparticles.
2. Developed a targeted HPLC-MS/MS method to simultaneously determine four urinary biomarkers of renal cell carcinoma and the application in the preliminary clinical studies.
3. Developed a vacuum-based loading system to charge PWHGMs with target materials as well as an effective washing procedure, and obtained NMR evidence of loaded materials in microspheres and its exchange with surrounding solutions as well as the kinetic releasing, which provide valuable information for the microspheres used in drug delivery.

## 1.9.DISSERTATION ORGANIZATION

This dissertation is comprised with three parts that individually describe three unique analytical techniques to determine three biological parameters. It is organized as follows.

In part one (Paper I), a dual-core fiber-optic pH micro-probe was designed and fabricated. The characterizations of the newly developed probe were done with inverted fluorescent microscope, scanning electron microscopy, and energy-dispersive X-ray

spectroscopy (EDS). The well-characterized pH probe was the applied to measure the pH change in the niche environment where cells were treated with different concentrations of $TiO_2$ nanoparticles. This study included the development a novel analytical technique and its application in nanoparticle toxicity.

In part two (Paper II), a target HPLC/MS-MS method was successfully developed to simultaneously determine quinolinic acid, 4-hydroxybenzoic acid, gentisic acid and α-ketoglutaric acid as RCC biomarkers in urine. The method was developed in 1% synthetic urine. The method was fully validated in real urine specimen with method detection limits, spiked recovery accuracy and reproducibility. Finally, the method was applied in urine specimens collected from 24 healthy people and 3 kidney cancer patients.

In part three, a vacuum-based loading system was established to load target materials into the microspheres. A follow-up washing procedure was developed to remove excess amount of materials from the outside of the microspheres. Unloaded and loaded microspheres were imaged by inverted optical microscopy. The unloaded microspheres were also characterized with field emission scanning electron microscopy (FESEM). Two binary systems, $C_{12}H_{26}/D_2O$ and $CHCl_3/D_2O$, were evaluated to obtain NMR evidence that material was loaded into the microspheres. Second, the esterification of isopropanol with acetic acid and its hydrolysis reactions were assessed with NMR spectroscopy to indicate the exchange of material from the inside of the microspheres with the surrounding solution. Microspheres loaded with water ($H_2O$) were submerged into $D_2O$ to study the microsphere release kinetics. NMR spectroscopy provided time-dependent data that could be fitted to a double-exponential raise to maximum curve. The

fitted curve showed two very specific release rates that may be due to the two specific sizes of the pores previously observed with the with field emission scanning electron microscopy (FESEM).

**PAPER**

# I. LOCAL PH MONITORING OF SMALL CLUSTER OF CELLS USING A FIBER-OPTIC DUAL-CORE MICRO-PROBE

Sisi Chen[1, 3], Qingbo Yang[1, 3], Hai Xiao[2,3], Honglan Shi[1, 3], Yinfa Ma[1, 3*]

[1]Department of Chemistry, Missouri University of Science and Technology, Rolla, MO, 65409, USA
[2]Department of Electrical and Computer Engineering, Clemson University, Clemson, SC, 29634, USA
[3]Center for Single Nanoparticle, Single Cell, and Single Molecule Monitoring,

Missouri University of Science and Technology, Rolla, MO, 65409, USA

[*] Corresponding Author
Department of Chemistry
Missouri University of Science and Technology
400 West 11th Street
Rolla, MO 65409
Tel: 573-341-6220
Fax: 573-341-6033
E-mail: yinfa@mst.edu

## ABSTRACT

Biological studies of tissues and cells have enabled numerous discoveries, but these studies still bear potential risks of invalidation because of cell heterogeneity. Through high-accuracy techniques, recent studies have demonstrated that discrepancies do exist between the results from low-number-cell studies and cell-population-based results. Thus the urgent need to re-evaluate key principles on limited number of cells has been provoked. In this study, a novel designed dual-core fiber-optic pH micro-probe was

fabricated and demonstrated for niche environment pH sensing with high spatial resolution. An organic-modified silicate (OrMoSils) sol-gel thin layer was functionalized by entrapping a pH indicator, 2′, 7′-Bis (2-carbonylethyl)-5(6)-carboxyfluorescein (BCECF), on a ~70 μm sized probe tip. Good linear correlation between fluorescence ratio of $I_{560\ nm}/I_{640\ nm}$ and intercellular pH values was obtained within a biological-relevant pH range from 6.20 to 7.92 ($R^2 = 0.9834$), and with a pH resolution of 0.035 ± 0.005 pH units. The probe's horizontal spatial resolution was demonstrated to be less than 2mm. Moreover, the probe was evaluated by measuring the localized extracellular pH changes of cultured human lung cancer cells (A549) when exposed to titanium dioxide nanoparticles ($TiO_2$ NPs). Results showed that the probe has superior capability for fast, local, and continual monitoring of a small cluster of cells, which provides researchers a fast and accurate technique to conduct local pH measurements for cell heterogeneity-related studies.

**Key words:** pH micro-probe; Fiber-optic sensor; Cell heterogeneity; Local/niche environment sensing; Organic modified silicates (OrMoSils); $TiO_2$ nanoparticles (NPs) cytotoxicity.

## 1. INTRODUCTION

Tissue and cellular level biological studies have enabled numerous scientific discoveries and biomedical applications. However, potential risks still exist when cell heterogeneity is taken into consideration, which may invalidate some of the fundamental principles that have been established previously [1-3]. The recent data generated by new high-accuracy techniques indicate that discrepancies do exist among those cell-

population based results [4-7], and thus there is an urgent need to re-evaluate some essential parameters with limited number of cells in order to truly realize precise medicine in the future.

The intra-/inter-cellular pH, as one of such key parameters, plays a key role in many cell behaviors and responses to surrounding stimuli [8]. The pH in cytosol and nucleus is normally adjusted to 7.2–7.4, and to 4.0-5.5 in endosomes and lysosomes [9, 10], and pH dysregulation leads to dysfunction of cells [11-14]. However, it is interesting to note that the intra- and extra-cellular pHs of tumor cells are regulated to be >7.4 and around 6.7-7.1, respectively [15-17], which is quite different from normal cells. These and more examples [18-21] demonstrate the significant roles that pH plays in many cell events. Unfortunately, current available techniques cannot provide the fast and local cellular pH measurements with high spatial resolutions that are necessary to distinguish potential heterogeneity among different cells. Conventional fluorescent dyes, like 2',7'-bis-(2-carboxypropyl)-5-(and-6-)-carboxyfluorescein (BCPCF) [22] and 2′,7′-Bis (2-carbonylethyl)-5(6)-carboxyfluorescein (BCECF) [17], are commonly used pH indicators, and in most cases they are hydrophobically modified for cytosolic but not for extracellular sensing. Particle-based nano-sensors, a new type of pH sensors, which can be embedded with Oregon Green (OG) and fluorescein, have been reported [23-25]. However, their potential toxicity of nanostructures to cells is still a problem for real time pH measurements while cells are still functioning. Other pH measurement approaches, such as fluorescence resonance energy transfer (FRET) based probes [26] and ion-sensitive field-effect transistor (ISFET) based sensors [27, 28], encounter more or less complexity and difficulties in their detecting principles and/or fabricating processes. In

addition, dealing with toxic heavy metal elements during probe development and manufacturing is also a concern in semiconductor-based approaches.

Fiber-optic-based sensors have been developed that are easy to fabricate, quick to respond, able to provide high spatial resolution detection, and have minimum invasiveness to cells [29-32]. A unique way of making fiber-optic-based pH sensors has been reported by using sol-gel coating techniques [33]. The novel point in using a sol-gel derived thin layer is that its nano- to micro-scale porous structure of the solidified networks can effectively entrap the pH indicating molecules. Furthermore, formed aerogel has high thermal stability and optical transparency, and is feasible for direct coating onto glass substrates [34].

In this study, a newly designed dual-core double-fiber twisted pH probe for quick fabrication and application was successfully fabricated and validated for niche cellular environment pH monitoring. The dual-core double-fiber configuration was fabricated by using a home-built twisting and gravitational-stretching system. A semi-spherical head design was applied in the new probe for maximum fluorescence reflection and collection, and the new probe head design was achieved by a distant fusion splicing method. Again, the pH sensitive dye BCECF was used and covalently entrapped in an organic-modified silicate (OrMoSils) sol-gel thin layer that was coated onto the sensing-head surface. The follow up scanning electron microscopic (SEM) imaging and energy-dispersive spectroscopy (EDS) characterization showed the successful fabrication of this probe, and probe validations in both standard pH buffers and cultured human lung cancer cells that were exposed to $TiO_2$ nanoparticles (NPs) were conducted in order to demonstrate the probe's applicability in many potential biomedical research areas.

# 2. MATERIALS AND METHODS

## 2.1. Fabrication and Coating of Micro-pH Probe

The dual-core micro-pH probe with a semi-spherical head shape was fabricated from two single mode optical fibers with core and cladding diameters of 62.5 and 125 μm (Corning, MA) using a homemade twisting and gravitational-stretching system (Figure. 1a). The cores of two optical fibers were fused with an optical fiber fusion splicer (Fujikura, Japan). In order to minimize background noise, one of the optical fibers served as an excitation laser transmission while the second fiber was used for fluorescence light collection. The pH-sensitive fluorescent dye 2′, 7′-Bis (2-carbonylethyl)-5(6)-carboxyfluorescein (BCECF) (LifeTechnologies Inc., New York) was mixed with an ultra-thin aerogel layer for pH sensing. The sol-gel dip-coating procedure was similar to our previous study [35, 36]. The chemicals used for coating, including dimethyl sulfoxide (DMSO), 2-succinimido-1,1,3,3 tetram-ethyluronium tetrafluoroborate (TSTU), N-ethyldiisopropylamine (Hünig's base), (3-Aminopropyl) triethoxysilane (APTES), tetraethoxysilane (TEOS), methyltrimethoxysi-lane (MTES), were purchased from Sigma-Aldrich (St. Louis, Missouri). The probe was acidified with concentrated nitric acid for 12 hours and washed with sufficient amount of Mili-Q (MQ) (EMD Millipore Corp., MA) water and pure ethanol. The probe was then dried at 100 ˚C for at least 3 hours. An alkoxides mixture was prepared with APTES, TEOS and MTES at a ratio of 4:1:1 (v/v) with catalytic amount (2% of total volume) of hydrochloric acid (0.1 M). The dried probe was dipped into the alkoxides mixture with a drawing rate of ~1 mm/s, and this process was repeated 8 – 10 times to obtain a sufficiently thick layer after curing. The mixture of BCECF, TSTU, and Hünig's base was reacted for one hour at

room temperature. The probe was then dipped into the dye solution for about 20 minutes and was incubated for 6 hours at 50 ˚C and then another 24 hours at 80 ˚C.

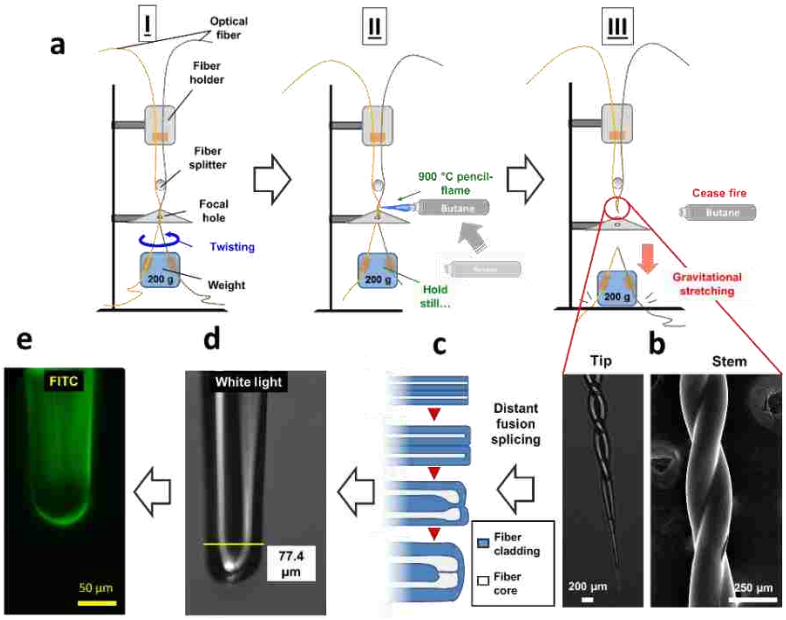


Figure 1. Procedures of fabricating dual-core twisted micro-pH probe. a) Fabrication of the probe stem by double-fiber twisting and gravitational-stretching using a home-built device; b) SEM and inverted microscopic images of fabricated probe stem and tip; c) schemes of how to fuse paralleled tapered fiber tips into the final dual core configuration using distant fusion splicing method; d) inverted microscopic image of fabricated dual core probe tip under white light; e) fabricated probe tip image under Fluorescein isothiocyanate (FITC) channel.

### 2.2. Characterization of Micro-pH Probes

The coated dual-core micro-pH probes were imaged by an inverted fluorescent microscope (Olympus IX51, Olympus, center valley, PA, USA) and scanning electron microscopy (SEM). The thin layer of coating on the probe's tip was characterized by energy-dispersive X-ray spectroscopy (EDS) (FEI, Hillsboro, OR, USA), including five scanned elements, carbon (C), nitrogen (N), oxygen (O), silicon (Si) and gold (Au). An inverted fluorescent microscope was used to take images of the probe under white light

and an FITC fluorescent channel, with which the BCECF dye can be examined. A quick-dry epoxy resin (EpoHeat, Buehler, Illinois) was used to embed the finished probes into the solidified resin, followed by cross-sectioning and fine grinding to just expose the probe head.

The pH probe was excited by a 488 nm continuous-wave (CW) Argon ion laser source (Spectra-Physics Lasers, Mountain View, California, USA), and a USB2000 spectrometer (Ocean optics, Dunedin, Florida) was used to collect the fluorescent signals at 560 nm. Before use, each fabricated probe was calibrated with a series of standard pH buffer solutions, which were prepared in 0.1 M phosphate buffer solution (PBS) (Life Technology, New York, USA). The pH values of the standard buffer solutions ranged from 5.86 to 8.45 with pH intervals around 0.2 that were first calibrated with Accumet AB15+ pH meter (Fisher Scientific, Pittsburgh, PA, USA). Afterwards, the coated dual-core double-fiber-twisted pH probe was dipped into pH solution for 15 ± 5 seconds to obtain a stable fluorescence reading, and the fluorescent spectrum was acquired. The probe was then rinsed with a sufficient amount of MQ water before the next measurement was conducted.

### 2.3. $TiO_2$ Nanoparticles and Characterization

The $TiO_2$ nanoparticles with sizes of 30 – 50 nm were purchased from Sigma-Aldrich (St. Louis, Missouri). The suspension of $TiO_2$ was prepared in cell culture medium without serum and sonicated 15 minutes by an ultrasonicator (FS-60H, 130W, 20 kHz; Fisher Scientific, Pittsburg, PA, USA). The $TiO_2$ nanoparticles were imaged and characterized by transmission electron microscopy (TEM) and EDS.

### 2.4. Spatial Resolution Test of Micro-pH Probe

$TiO_2$ NPs were measured 3.5 mg in total, and were slowly dosed directly onto one single point (diameter < 1mm) at the bottom of a dish that was pre-cultured with A549 cells. The pH of three different local points in the same dish, at distances from the NP-dosing spot of 0 mm, 2 mm and 10 mm, were continuously monitored using our probe for 4 hours. Meanwhile, a separate dish that was also dosed with same amount of $TiO_2$ NPs but without cell cultures was also monitored to evaluate pH variation caused by NPs.

### 2.5. Cell Culture Conditions and Treatment with $TiO_2$

The adenocarcinomic human alveolar basal epithelial cell line, A549, was obtained from American Type Culture Collection (ATCC) (Manassas, Virginia). Ham's F-12K medium with L-glutamine was purchased from Caisson Laboratories (North Logan, Utah), and was supplemented with 2 mM L-glutamine, 1 mM sodium pyruvate, 1% non-essential amino acids, 50 U/mL penicillin, and 50 mg/mL streptomycin for sub-culture. Cells were cultured at 37 °C with 5% $CO_2$ and 95% humidity. A549 cells were pre-seeded into a 96-well plate (Corning Inc., New York) at a density of $1 \times 10^5$ cells per well in 200 µL culture medium and cultured for 16-18 hours to allow cells to attach. Different concentrations (50, 100 and 150 µg/mL) of $TiO_2$ NPs suspensions were prepared separately with Ham's F-12K medium and immediately applied to the cells after pretreatment. Cells without NPs treatment served as controls in each experiment. The pH reactive oxygen species (ROS) generation and cell viability were all measured after 0, 1, 3, 6, 12, 24, 36, and 48-hour exposures to the nanoparticles.

### 2.6. pH Measurement of Cell Colony

The coated dual-core micro-pH probes were applied to measure the pH of the micro-environment around the cells treated with different concentrations of $TiO_2$ nanoparticles. After exposure to different concentration of $TiO_2$ nanoparticles for 1, 3, 6, 12, 24, 36, and 48 hours, the probe was dipped into each well to conduct a pH measurement. After each measurement, the probe was rinsed with sufficient amounts of MQ water.

### 2.7. Assessment of Cytotoxicity

To determine the cytotoxicity of $TiO_2$ nanoparticles, the cell proliferation reagent WST-1 (Roche Life Science, Indianapolis, Indiana) was used following the manufacturer's instructions. After cells were exposed to $TiO_2$ nanoparticles for 1, 3, 6, 12, 24, 36, and 48 hours, the absorbance at 450 nm was measured using a microplate reader (FLOURstar; BMG Labtechnologies, Durham, North Carolina).

The ROS level was determined by using Penicillin–streptomycin, 2', 7' - dichlorofluorescin diacetate (DCFH-DA) purchased from Life Technology (Grand Island, New York). The stock solution was prepared in dimethyl sulfoxide (DMSO) at a final concentration of 10 mM and the 20 μM working solution was prepared by diluting the stuck solution 500-fold with Hanks' Balanced Salt solution (HBSS, Life Technology, Grand Island, New York). The supernatant was taken out from each well, and cells were incubated with the working solution in a dark environment for 1 hour at 37 ˚C. Fluorescence was then determined at 485 nm excitation and 520 nm emission using a microplate reader (FLOUR star; BMG Lab Technologies, Durhan, North Carolina).

### 2.8. Statistics

Experimental data in this study was analyzed by one-way ANOVA followed by a Post Hoc test. All experimental results were expressed as the mean value, and standard deviation (SD) was derived from triplicate measurements. Two-tail Student's *t*-test was applied for significance testing. The level of statistical significance was presented as a *p*-value of <0.05 (*), <0.01 (**) as well as <0.001 (***).

## 3. RESULTS AND DISCUSSIONS

### 3.1. Probe Fabrication

Our prior studies [35, 36] have reported the development of micro-spherical and 1-in-6 hexagonal fiber-optic pH sensors, which demonstrate a new approach to measure pH in a confined niche environment, including at the single-cell level. In the present study, the probe structure was redesigned to reduce the difficulty of fabrication and to achieve quick sensing performance (Figure 1). A twisted fiber configuration provides several advantages over a parallel aligning configuration, such as better robustness and structural uniformity, thus enhancing the light transmission. The gravitational-stretching system provides controllable forces while pulling twisted fibers down to a micro-sized taper (Figure 1b). A home-built double-fiber twisting and gravitational-stretching system was used for the main sensing stem fabrication (Figure 1a). Using a pencil flame torch enabled us to precisely fabricate a short length (0.5 – 1.2 cm) twisted sensor shaft with two fibers fused only at the cladding section. A distant-fusion was applied to mildly bend inner cores toward each other with an intermediate thin (<5 μm) layer of cladding (Figure 1c, 1d). Finally, a sol-gel dip-coating procedure was applied, followed by aging, curing,

and carbon dioxide ($CO_2$) supercritical drying. A covalent bond between pH sensitive dye and the aerogel was thus formed (Figure 1e), as described in our previous work [35].

The fabricated probe was characterized through SEM/EDS scanning (Figure 2). Results showed that the fabricated probe head had a diameter of around 80 μm. A cross-section image evidently proved a cladding-only fusion as expected (Figure 2, a-d). An outside enwrapping layer (3 – 8 μm) (Figure 2d) around the two inner fibers was the dye embedded aerogel, featured with typical porous networks (Figure 2e), which allows quick interactions between protons (analytes) and BCECF molecules. EDS scanning showed the existence of high percentages of carbon (20.81%) and nitrogen (6.29%), while considerably low oxygen (67.8%) and silica (4.15%) (Figure 2f), when compared to non-coated area (Figure 2g, h), indicating successful amide bonding of BCECF [35]. These overall observations demonstrated a successful fabrication of a dual-core micro-pH probe featured with a BCECF dye-doped aerogel sensing layer.

### 3.2. System Setup and Probe Calibration

The reflection-mode probing system is composed of two major parts, a laser excitation pathway, and a fluorescence signal collection pathway, which are joined together at the sensor tip [37]. Briefly, the 488 nm Argon ion laser beam was introduced into one fiber through focusing, and the excited fluorescence emission can be picked up by the other fiber and transmitted to the detector (Figure 3a). More detailed procedures can be found elsewhere. Compared to our previous single fiber configuration [35], this design can significantly separate the exciting laser and emission signal light through two-fiber usage and separated cores, thus this design may provide a higher signal-to-noise (S/N) ratio.

The finished probe was then calibrated by a set of stepping pH buffers that were standardized using a conventional pH meter. A fluorescence peak was observed at around 550 nm (Figure 3b), and the peak intensity was found to be linearly correlated with the pH values. The linear correlation range was observed from pH 6.20 to pH 7.92 with a coefficient factor of 0.9834 (Figure 3c). Over this pH range, a typical sigmoidal correlation was observed. We thus specifically chose to focus on the linear correlation region, which had already covered the most interested biologically relevant range. Triplicate measurements were conducted for each probe, and several probes were used to come up with a pH detecting resolution of 0.035 ± 0.005 pH units calculated by the standard deviation from triplicate measurements, indicating a good reproducibility.

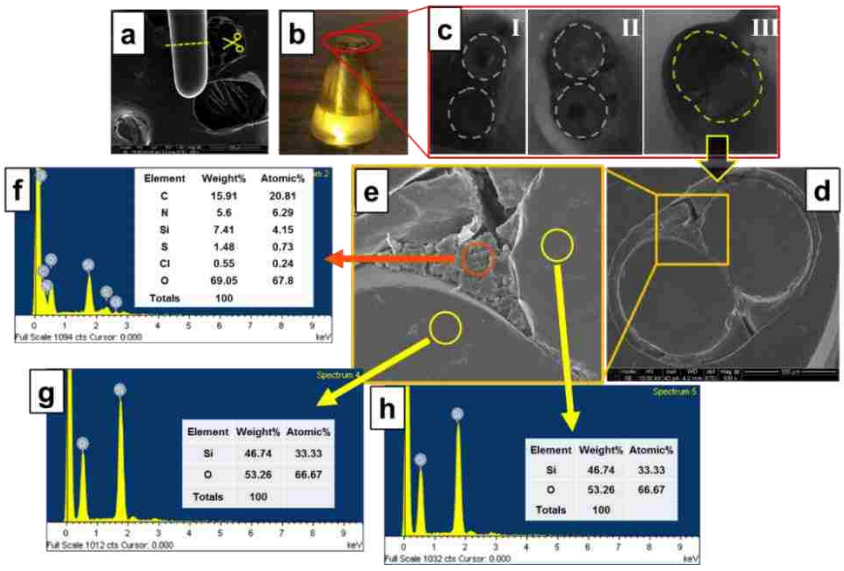


Figure 2. Probe characterization by SEM and EDS analysis. a) SEM image of probe tip; b) the epoxy module immobilized several finished probe within it; c) three different probe cross-sections; d) SEM image of cross section of the dual-core double-fiber twisted pH probe; e) magnified image of square area in (d); f) EDS scanning result of red-circled area in (e); g) and h) EDS scanning results of yellow-circled areas in (e).

Higher sensitivity and pH resolution can theoretically be further achieved by increasing the dye concentration or the laser power. However, this was not recommended due to the possibility of self-quenching and photo-bleaching [37]. The current methodology may also suffer from varied temperature and ionic strength, as has been discussed elsewhere [35, 36]. Nevertheless, no significant interferences to the probe were observed due to these two factors, as long as the measuring condition fell within a biologically relevant range.

### 3.3. Determination of Probing Spatial Resolution

To validate the detecting spatial resolution of the fabricated probe, we used spot dosing (Figure 4d) of 30 – 50 nm $TiO_2$ NPs (Figure 4, a-c) to induce cell deterioration. Results showed apparent pH decreases in all cells + NP groups, while no significant changes were observed in the NP-only groups. Statistically significant differences between cells + NP and control groups began to show after the 90-minute NP dosing. After 150 minutes, significant differences between cells + NPs groups also started to show (Figure 4e). The latter results particularly indicated a site difference of cell responses due to the non-evenly distributed NP concentration. The capability to differentiate such small-scale pH values also indicated the high spatial resolution of our probe. This ability is essentialfor site-specific measurement in a local area, and especially when the pH is variated drastically in that niche environment, such as within a small cluster of cells or a wounded tissue area, etc.

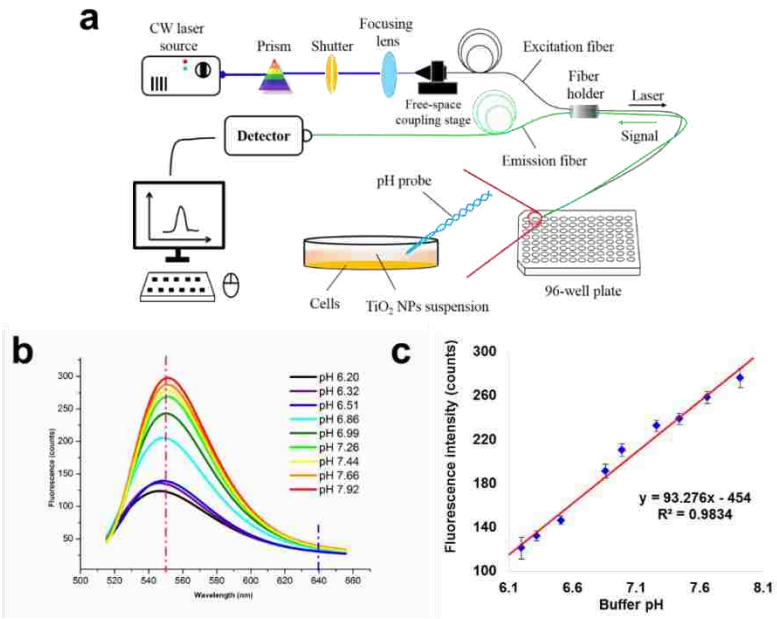


Figure 3. a) Schematic diagram of system setup. The integrated system consisted of a CW Argon laser source, a prism, a shutter, a focusing lens, a free-space coupling stage, a detector, and a computer. The dual-core double-fiber twisted pH probe was integrated into the system and was applied for pH measurements in each well of a 96-well plate; b) A fluorescent spectra was plotted based on probe signal intensity range from 510 nm to 650 nm under a set of standardized pH buffer solution that ranged from pH 6.20 to pH 7.92. The vertical red and blue dash lines represent the peak (550 nm) wavelength and the reference wavelength (640 nm) for final ratio-based pH calculation ($I_{550nm}/I_{640nm}$); c) Linear correlation between buffer pH and fluorescent spectra peak intensity.

### 3.4. Detecting Early Onset of Cell Deterioration Induced by $TiO_2$ NPs

To further demonstrate the probe's ability to detect actual cellular events, the probe was applied to monitor cell response to $TiO_2$ nanoparticles. Engineered nanoparticles (ENPs), though used in many fields such as biomedical imaging and detecting [38, 39], cancer therapy [40], drug delivery [41], water purification [42], and cosmetics [43, 44], bear potential toxic concerns due to their intrinsic nano-scale sizes, heavy metal composition, large specific surface areas, and high photo-reactivity [45-47].

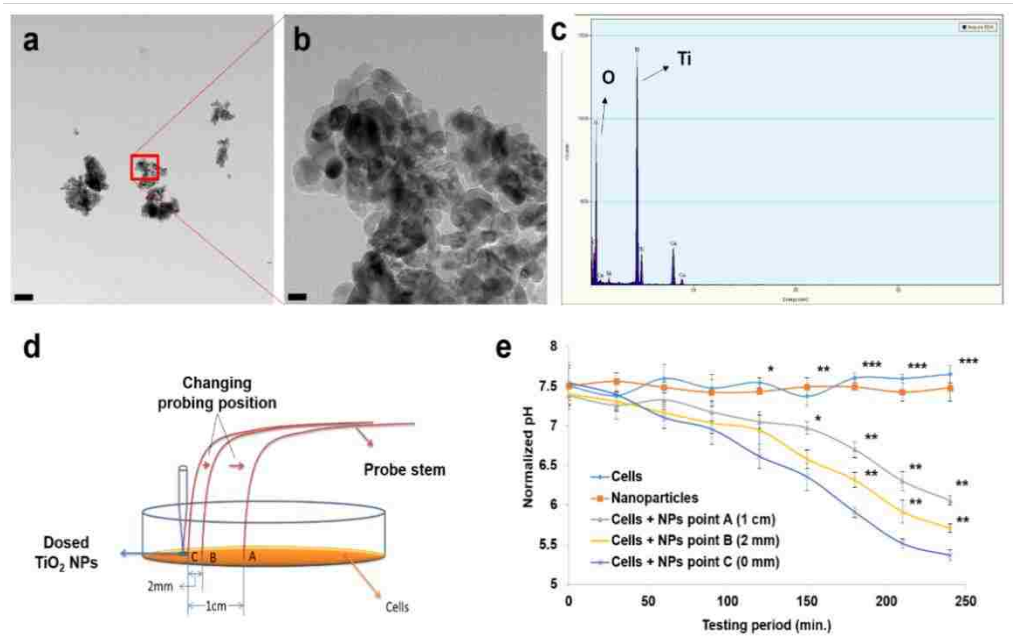


Figure 4. $TiO_2$ NPs characterization and determination of the probe's spatial resolution. a) TEM image of applied $TiO_2$ NPs, and b) zoom-in image of the NPs squared in a). c) EDS scanning result showing chemical composition of the $TiO_2$ NPs. d) Schematic of how to test the spatial resolution of the pH micro-probe. E) Four-hour continual pH monitoring of cells + NP response at three different spots as shown in d), and compared with cell-only and NP-only groups. Statistical significance is interpreted as a *p*-value of <0.05 (*), <0.01 (**) as well as <0.001 (***). Scale bar: a) 200 nm; b) 20 nm.

The NP-caused cell damages are hard to track and study because they are complicated and highly spatiotemporally specified. In the present study, both the probe and two conventional methods were used to monitor cell changes in pH, viability, and ROS. An adenocarcinomic human alveolar basal epithelial cell line, A549 (CCL-185, ATCC), was used and a 40 nm sized $TiO_2$ NPs at concentrations of 50, 100, and 150 µg/mL were applied for cell exposure up to 48 hours. A cell-only group was used as the control in all tests. An NP-only group was also tested and no significant pH variations were induced by the NPs (data not shown).

Results showed decreased pHs and cell viabilities and increased ROS accumulation in NP-dosed groups (Figure 5). We interpreted these results as an early onset of cell deterioration due to the NP's toxicity, and the down regulation seemed related to this process. In detail, higher NP dosages resulted in lower viability and pH, and higher ROS generation. Meanwhile, no significant pH variation in the control group was observed. A similar result was shown in a previous study where cell apoptosis was correlated with $TiO_2$ NP's concentration [46]. Additionally, a time effect was also observed: the longer the NPs were exposed, the lower the viability and pH, while the higher the ROS. Compared with the two conventional methods, the pH measurements showed at least equal ability in detecting NP-induced cell deterioration (which statistically differed from the control group). However, at the highest NP-dosing concentration, our probe can effectively differentiate the signals generated by the NP-dosed cells from those of the control cells ($p < 0.05$, "*") when NPs were just applied, which is couple of hours ahead of the statistically meaningful results that were reported by the viability and ROS assays.

The purpose of using two traditional assays, cell viability and ROS generation, was to demonstrate the effectiveness of the pH probe. On one hand, cell viability was reflected by the enzymatic activity of the mitochondrial level of succinic dehydrogenase, which was finally represented by the formazan concentration through a colorimetric evaluation [48]. ROS generation, one of the known NP-induced syndromes [45, 46, 49], has also been correlated with the mitochondrial inner membrane potential [50]. Thus, both viability and ROS assays are related to mitochondrial stability and may serve as relatively early-stage signs of cell deterioration before whole cell degradation occurs. On

the other hand, ion channels, such as $H^+/K^+$, $Na^+/H^+$, $Cl^-/HCO_3^-$, were also correlated with pH regulation. And these ion channels were found on both cell and mitochondrial membranes [51]. Our results, thus, showed an important correlation between extracellular pH and NP exposure. The detected pH changes featured a locally radical acidification due to the NP destruction, and such local changes happened faster than the other two population-based assays. Although further mechanistic studies on the pH variation triggering points during NP-induced cell degradation and its correlation with mitochondria stability are still needed, our developed pH micro-probes may find applications in detecting subtle and local cellular changes in a fast and stain-free manner.

## 4. CONCLUSIONS

In this study, we successfully developed and fabricated a novel dual-core micro-pH probe using a home-built double-fiber twisting and gravitational-stretching system. The probe was coated by a specific OrMoSils dye-doping method and applied for pH sensing in a microliter environment. The enhanced mechanical structure of the probe with fused double fibers successfully separated the excitation beam and emission light, thus providing the robust probe with reduced background noise and increased sensitivity. A linear correlation between pH and spectral peak intensity was found within a biologically meaningful pH range of 6.20 to 7.92 and a coefficient factor of 0.9834 was achieved. The probe's spatial resolution was then exemplarily tested and a resolution of at least 2 mm was clearly demonstrated in a cell + NPs exposure test. We finally applied this probe in a $TiO_2$ NP-induced cytotoxicity assay. Results revealed a concentration/time dependence of the NP's cytotoxicity. Results also demonstrated the probe's potential for fast, local and

continuous monitoring of cellular events in a staining-free manner, which may greatly impact future quasi-single-cell and cell-heterogeneity-driven researches.

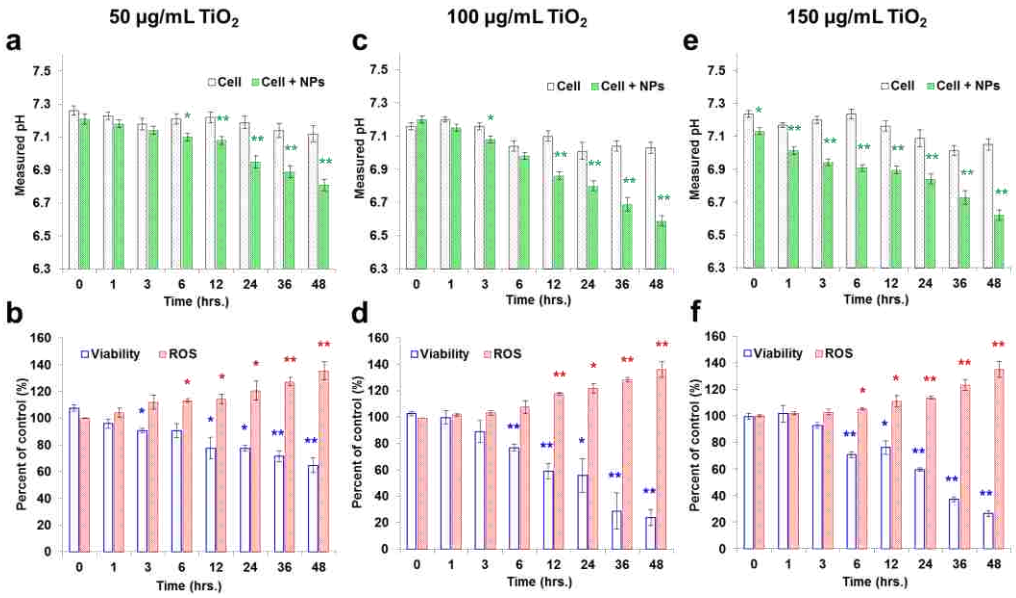


Figure 5. The application of the novel pH probe in measuring cell colony's pH variations and their comparison d with cell viability and ROS generation in a $TiO_2$ NP-induced cytotoxicity model. Green plots are pH measurement using our developed probe, blue and red plots are data are the cell viability and ROS kits measurements. Three NP concentration, 50, 100 and 150 µg/mL, were used is this study. Values are mean ± SD ($n \geq 3$). Statistical significance was indicated by $*p < 0.05$ (significant), and $** p < 0.01$ (very significant), versus the control groups.

**ACKNOWLEDGEMENTS**

The authors would like to thank Clarissa A. Wisner and Qianyao Li at the Missouri University of Science and Technology, for their assistance with SEM imaging and EDS scanning. The authors also thank Dr. Kathleen Drowne for her proof-reading and editing assistance for this manuscript. This work was supported by the National Institute of Health (NIH, 1R21GM104696-01).

**REFERENCE**


1. Arriaga, E.A., *Single cell heterogeneity.* Single Cell Analysis: Technologies and Applications, 2009: p. 223-234.

2. Aird, W.C., *Endothelial cell heterogeneity.* Critical care medicine, 2003. **31**(4): p. S221-S230.

3. Tang, D.G., *Understanding cancer stem cell heterogeneity and plasticity.* Cell research, 2012. **22**(3): p. 457-472.

4. Altschuler, S.J. and L.F. Wu, *Cellular heterogeneity: do differences make a difference?* Cell, 2010. **141**(4): p. 559-563.

5. Davey, H.M. and D.B. Kell, *Flow cytometry and cell sorting of heterogeneous microbial populations: the importance of single-cell analyses.* Microbiological reviews, 1996. **60**(4): p. 641-696.

6. Elowitz, M.B., et al., *Stochastic gene expression in a single cell.* Science, 2002. **297**(5584): p. 1183-1186.

7. Kamme, F., et al., *Single-cell microarray analysis in hippocampus CA1: demonstration and validation of cellular heterogeneity.* The Journal of neuroscience, 2003. **23**(9): p. 3607-3615.

8. Casey, J.R., S. Grinstein, and J. Orlowski, *Sensors and regulators of intracellular pH.* Nature reviews Molecular cell biology, 2010. **11**(1): p. 50-61.

9. Haas, A., *The phagosome: compartment with a license to kill.* Traffic, 2007. **8**(4): p. 311-330.

10. Kurkdjian, A. and J. Guern, *Intracellular pH: measurement and importance in cell activity.* Annual review of plant biology, 1989. **40**(1): p. 271-303.

11. Webb, B.A., et al., *Dysregulated pH: a perfect storm for cancer progression.* Nature Reviews Cancer, 2011. **11**(9): p. 671-677.

12. Neri, D. and C.T. Supuran, *Interfering with pH regulation in tumours as a therapeutic strategy.* Nature reviews Drug discovery, 2011. **10**(10): p. 767-777.

13. Matés, J.M., et al., *Intracellular redox status and oxidative stress: implications for cell proliferation, apoptosis, and carcinogenesis.* Archives of toxicology, 2008. **82**(5): p. 273-299.

14. Chiche, J., et al., *Hypoxia-inducible carbonic anhydrase IX and XII promote tumor cell growth by counteracting acidosis through the regulation of the intracellular pH.* Cancer research, 2009. **69**(1): p. 358-368.

15. Gillies, R.J., et al., *MRI of the tumor microenvironment.* Journal of Magnetic Resonance Imaging, 2002. **16**(4): p. 430-450.

16. Busco, G., et al., *NHE1 promotes invadopodial ECM proteolysis through acidification of the peri-invadopodial space.* The FASEB Journal, 2010. **24**(10): p. 3903-3915.

17. Han, J. and K. Burgess, *Fluorescent indicators for intracellular pH.* Chemical reviews, 2009. **110**(5): p. 2709-2728.

18. Booth, I.R. *The regulation of intracellular pH in bacteria*. in *Novartis Foundation Symposium 221-Bacterial Responses to Ph*. 2007. Wiley Online Library.

19. Martin, C., et al., *Intracellular pH gradients in migrating cells.* American Journal of Physiology-Cell Physiology, 2011. **300**(3): p. C490-C495.

20. Roos, A. and W.F. Boron, *Intracellular pH*. 1981: Am Physiological Soc.

21. Minton, K., *Cell signalling: Responding to intracellular pH.* Nature Reviews Molecular Cell Biology, 2013. **14**(10): p. 608-609.

22. LIU, J., Z. DIWU, and D. KLAUBERT, *Fluorescent Molecular Probes. Part 3. 2′, 7′ - Bis - (3 - carboxypropyl) - 5 - (and - 6) - carboxyfluorescein (BCPCF): A New Polar Dual - Excitation and Dual - Emission pH Indicator with a PKA of 7.0.* ChemInform, 1998. **29**(11).

23. Benjaminsen, R.V., et al., *Evaluating nanoparticle sensor design for intracellular pH measurements.* ACS nano, 2011. **5**(7): p. 5864-5873.

24. Peng, J., et al., *Noninvasive monitoring of intracellular pH change induced by drug stimulation using silica nanoparticle sensors.* Analytical and bioanalytical chemistry, 2007. **388**(3): p. 645-654.

25. Ruedas-Rama, M.J., et al., *Fluorescent nanoparticles for intracellular sensing: a review.* Analytica chimica acta, 2012. **751**: p. 1-23.

26. Dennis, A.M., et al., *Quantum dot–fluorescent protein FRET probes for sensing intracellular pH.* ACS nano, 2012. **6**(4): p. 2917-2924.

27. Toumazou, C. and S. Purushothaman, *Use of a pH sensor comprising an ion-sensitive field effect transistor (ISFET) to perform real time detection/quantification of nucleic acid amplification*. 2012, Google Patents.

28. Sakurai, T. and Y. Husimi, *Real-time monitoring of DNA polymerase reactions by a micro ISFET pH sensor.* Analytical chemistry, 1992. **64**(17): p. 1996-1997.

29. Udd, E. and W.B. Spillman Jr, *Fiber optic sensors: an introduction for engineers and scientists*. 2011: John Wiley & Sons.

30. Froggatt, M. and J. Moore, *High-spatial-resolution distributed strain measurement in optical fiber with Rayleigh scatter.* Applied Optics, 1998. **37**(10): p. 1735-1740.

31. Reed, W.A., M.F. Yan, and M.J. Schnitzer, *Gradient-index fiber-optic microprobes for minimally invasive in vivo low-coherence interferometry*. Optics letters, 2002. **27**(20): p. 1794-1796.

32. Vo-Dinh, T. and P. Kasili, *Fiber-optic nanosensors for single-cell monitoring.* Analytical and bioanalytical chemistry, 2005. **382**(4): p. 918-925.

33. Chaudhury, N., R. Gupta, and S. Gulia, *Sol-gel Technology for Sensor Applications (Review Paper).* Defence Science Journal, 2007. **57**(3): p. 241-253.

34. Lin, J. and C.W. Brown, *Sol-gel glass as a matrix for chemical and biochemical sensing*. TrAC Trends in Analytical Chemistry, 1997. **16**(4): p. 200-211.

35. Yang, Q., et al., *Reflection-mode micro-spherical fiber-optic probes for in vitro real-time and single-cell level pH sensing.* Sensors and Actuators B: Chemical, 2015. **207**: p. 571-580.

36. Yang, Q., et al., *Fiber-Optic-Based Micro-Probe Using Hexagonal 1-in-6 Fiber Configuration for Intracellular Single-Cell pH Measurement.* Analytical chemistry, 2015. **87**(14): p. 7171-7179.

37. Yang, Q., et al., *A Novel Fiber-Optic Based Micro-Probe Using Hexagonal 1-in-6 Fiber Configuration for Intracellular Single-Cell pH Measurement.* Analytical chemistry, 2015.

38. Agasti, S.S., et al., *Nanoparticles for detection and diagnosis.* Advanced drug delivery reviews, 2010. **62**(3): p. 316-328.

39. Hahn, M.A., et al., *Nanoparticles as contrast agents for in-vivo bioimaging: current status and future perspectives.* Analytical and bioanalytical chemistry, 2011. **399**(1): p. 3-27.

40. Brannon-Peppas, L. and J.O. Blanchette, *Nanoparticle and targeted systems for cancer therapy.* Advanced drug delivery reviews, 2012. **64**: p. 206-212.

41. Cho, K., et al., *Therapeutic nanoparticles for drug delivery in cancer.* Clinical cancer research, 2008. **14**(5): p. 1310-1316.

42. Pradeep, T., *Noble metal nanoparticles for water purification: a critical review.* Thin solid films, 2009. **517**(24): p. 6441-6478.

43. Bolzinger, M.A., S. Briançon, and Y. Chevalier, *Nanoparticles through the skin: managing conflicting results of inorganic and organic particles in cosmetics and pharmaceutics.* Wiley Interdisciplinary Reviews: Nanomedicine and Nanobiotechnology, 2011. **3**(5): p. 463-478.

44. Wiechers, J.W. and N. Musee, *Engineered inorganic nanoparticles and cosmetics: facts, issues, knowledge gaps and challenges.* Journal of biomedical nanotechnology, 2010. **6**(5): p. 408-431.

45. Chen, J., et al., *In vivo acute toxicity of titanium dioxide nanoparticles to mice after intraperitioneal injection.* Journal of Applied Toxicology, 2009. **29**(4): p. 330-337.

46. Park, E.-J., et al., *Oxidative stress and apoptosis induced by titanium dioxide nanoparticles in cultured BEAS-2B cells.* Toxicology letters, 2008. **180**(3): p. 222-229.

47. Shukla, R.K., et al., *ROS-mediated genotoxicity induced by titanium dioxide nanoparticles in human epidermal cells.* Toxicology in Vitro, 2011. **25**(1): p. 231-241.

48. Vistica, D.T., et al., *Tetrazolium-based assays for cellular viability: a critical examination of selected parameters affecting formazan production.* Cancer Research, 1991. **51**(10): p. 2515-2520.

49. Love, S.A., et al., *Assessing nanoparticle toxicity.* Annual review of analytical chemistry, 2012. **5**: p. 181-205.

50. Kowaltowski, A.J., et al., *Mitochondria and reactive oxygen species.* Free Radical Biology and Medicine, 2009. **47**(4): p. 333-343.

51. Matsuyama, S. and J. Reed, *Mitochondria-dependent apoptosis and cellular pH regulation.* Cell death and differentiation, 2000. **7**(12): p. 1155-1165.

# II. SIMULTANEOUS DETERMINATION OF URINARY QUINOLINATE, GENTISATE, 4-HYDROXYBENZOATE, AND α-KETOGLUTARATE BY HIGH-PERFORMANCE LIQUID CHROMATOGRAPHY – TANDEM MASS SPECTROMETRY

Sisi Chen[a], Casey Burton[a], Anthony Kaczmarek[b], Honglan Shi[a], Yinfa Ma[a*]

[a] Department of Chemistry and Center for Single Nanoparticle, Single Cell, and Single Molecule Monitoring, Missouri University of Science and Technology, Rolla, MO, USA 65409

[b] Central Missouri Urology Clinic, Rolla, MO, USA 65401

[*] Corresponding Author
Yinfa Ma, PhD
Address: Department of Chemistry
Missouri University of Science and Technology
400 West 11th Street
Rolla, MO 65409
Tel: 573-341-6220
Fax: 573-341-6033
E-mail: yinfa@mst.edu

## ABSTRACT

Renal cell carcinoma (RCC) remains a difficult-to-detect cancer for which new detection methodologies are urgently needed to improve screening efficacy. Urinary metabolomic profiling has identified several potential RCC biomarkers, including quinolinic acid, 4-hydroxybenzoic acid, gentisic acid and α-ketoglutaric acid. These four endogenous metabolites have unique pathophysiological mechanisms associated with RCC, suggesting they may be promising biomarkers for earlier RCC detection. However,

the lack of targeted analytical methods for their simultaneous determination in urine has hindered efforts to evaluate their clinical applicability. In this study, a robust high-performance liquid chromatography - tandem mass spectrometry (HPLC-MS/MS) technique using multiple reaction monitoring was developed to simultaneously monitor these four urinary biomarkers. The method was validated by multiple figures of merit including method detection limits (0.05 ng/mL to 1 ng/mL), spiked recovery accuracy (88.6% - 114.8%) and reproducibility (0.4 – 9.3% RSD). The applicability of the method was further demonstrated in clinically relevant 100-fold diluted urine specimens. All four potential biomarkers were successfully quantified with urinary concentrations that were in agreement with previous reports. In conclusion, an accurate and sensitive method has been described for the simultaneous determination of quinolinic acid, 4-hydroxybenzoic acid, gentisic acid and α-ketoglutaric acid. We anticipate this method to significantly benefit clinical translational research aiming to evaluate the clinical applicability of these four potential biomarkers.

**Key words**: Liquid chromatography – tandem mass spectrometry; Quinolinic Acid; Gentisic acid; 4-Hydroxybenzoic acid; renal cell carcinoma

## 1. INTRODUCTION

Renal cell carcinoma (RCC), more colloquially known as kidney cancer, remains a difficult-to-detect cancer with 64,000 expected new U.S. cases in 2015, representing 3.8% of all new expected cancer diagnoses in the United States[1]. While RCC incidence has risen in recent years, whether this increase can be attributed to improved screening practices is unclear[2-4]. Imaging-based techniques, such as abdominal ultrasound and

computerized tomography (CT) scans, have proven effective in detecting renal masses in symptomatic RCC cases[4, 5]. Recent advances in contrast-enhanced ultrasonography (CEUS)[6] and positron emission tomography – computed tomography (PET-CT)[7] have further enhanced diagnostic accuracy. However, the high prevalence of asymptomatic RCC cases poses considerable diagnostic challenges for medical imaging approaches to RCC detection and diagnosis. Namely, routine screening in the general population is still not considered cost-effective. Overdetection of small, indolent renal masses, representing some 70% of all RCC cases[8, 9],many of which are detected incidentally from bladder and prostate cancer screenings[4, 10-12], has substantially contributed to increased costs and toxicities associated with overtreatment. Patient management and treatment decisions have consequently shifted toward increased active surveillance of indolent masses over exclusive use of radical nephrectomy [7]. However, active surveillance is not a viable patient management option for socioeconomically and/or geographically disadvantaged patients, and for those that it is, can burden patients who must undergo follow-up imaging with new costs and morbidity. Finally, these technological advances in RCC detection have not meaningfully impacted RCC mortality despite greatly increased incidence rates. New molecular-based techniques capable of reflecting RCC carcinogenesis and progression are therefore urgently needed to better discriminate biologically aggressive tumors from indolent renal masses and improve patient outcomes.

Metabolomics represents an emerging “omics” approach to link pathophysiological metabolic changes to individual patient care. Unlike the genome or even proteome, changes in the metabolome are rapid and represent the final response of

an organism to both internal and external stimuli[13, 14]. Urinary metabolomics is rapidly emerging as a patient- and laboratory-friendly diagnostic platform owing to its noninvasive detection modality, minimal burden to patients, and inexpensive assays. While proteomics has been extensively applied to RCC biomarker discovery, RCC metabolomics remains relatively underdeveloped [15, 16]. Nevertheless, recent research has identified a growing panel of potential metabolic biomarkers such as hippuric acid and myoinositol[17], acetoacetate and lactate[18, 19], and sphingomyelin [20] with potentially wide-ranging metabolic implications affecting phospholipid catabolism, tryptophan metabolism, phenylalanine metabolism, nicotinate and nicotinamide metabolism, citric acid cycle, benzoate metabolism, and more[20, 21]. While analytical methods exist for the detection of these compounds in bodily fluids, four metabolomically implicated compounds, α-ketoglutaric acid, quinolinic acid, gentisic acid, and 4-hydroxybenzoic acid, are particularly promising biomarkers for the detection and diagnosis of RCC based on their underlying pathophysiology related to RCC.

Briefly, quinolinic acid, a $NAD^+$ precursor and an essential intermediate in the tryptophan metabolism pathway, is overexpressed in pathological RCC [21-24]. Tryptophan metabolism up-regulation is related to increased cellular glycolytic activity [25, 26] while increased activity of catalytic enzyme indoleamine 2,3-dixoxygenase has further been shown to suppress immune cell proliferation and promote immune escape [27-29]. For these reasons, the related tryptophan and kynurenine pathways have been used to stage various cancers[30]. α-Ketoglutaric acid is a classic Warburg metabolite that is differentially expressed from citric acid cycle up-regulation and activation of the alanine, aspartate, and glutamate synthetic pathways. Finally, gentisic acid and 4-

hydroxybenzoic acid serve important roles in the benzoate degradation via hydroxylation pathway and may function in preventing lipoprotein oxidation in cancer cells [21, 31]. This functional understanding has led to considerable clinical interest that aims to evaluate the clinical applicability of these four compounds in RCC screening. However, no quantitative analytical techniques have yet been described for their simultaneous and sensitive detection in urine. While a number of methodologies encompassing an array of analytical platforms such as LC-MS [32-34] and GC-MS [35-37] have been reported to detect these metabolites individually in various biomatrices, no techniques currently exist for urinary screening purposes to the best of our knowledge. Therefore, we sought to develop a targeted high-performance liquid chromatography – tandem mass spectrometry (HPLC-MS/MS) technique using hybrid quadrupole – linear ion trap (QqLIT) tandem mass analyzer to accurately and rapidly determine these four urinary biomarkers. This analytical platform utilized multiple reaction monitoring (MRM) scans, which advantageously monitor the structure-dependent transition from unique precursor ions to unique product ions following analyte fragmentation by collision gases. This two-step approach to analyte quantification greatly minimizes potential isomeric interferences, affording highly selective quantification in complex urine matrices that likely have multiple isomeric interferences. The applicability of the newly developed method to clinical screening efforts was finally demonstrated in clinical urine specimens collected from healthy individuals and patients with pathologically confirmed RCC and renal masses.

## 2. RESULTS AND DISCUSSION

### 2.1. MS/MS Optimization

The four compounds were individually optimized with respect to compound-dependent parameters and ion transitions using direction infusion MS/MS. Direct infusions were performed using reagent standards prepared at a concentration of 200 ng/mL in 0.5% formic acid to mimic speciation and adduct formation under relevant matrix conditions. An automated syringe pump infused standards at a rate of 0.30 mL/hour. Prior to the selection of 0.5% formic acid, other additives such as acetate acid, ammonium acetate, and ammonium formate were considered but yielded suboptimal ionization efficiencies. During the infusion, full scan data acquisition utilizing Multiple Channel Analyzer (MCA) modes under positive and negative ionization were initially used to identify primary precursor ions and any potential analyte-additive adducts. Briefly, ionization efficiencies for the hydroxyl-containing 4-hydroxybenzoic acid and gentisic acid were approximately equivalent for negative ion ($[M-H]^-$) and positive ion ($[M+H]^+$) modes. Negative ion mode afforded the most efficient ionization mechanism for dicarboxylic α-ketoglutaric acid and quinolinic acid, yielding strong $[M-H]^-$ and $[M-COOH]^-$ precursor ions. For this reason, negative-ion ESI ionization facilitated by 0.5% formic acid additive was selected for mass spectrometric detection of the four compounds. Following selection of the precursor ion and ionization method, automated MS/MS parameter optimization for each compound provided the following compound-dependent parameters: declustering potential (DP), collision energy (CE), and collision cell exit potential (CXP) (Table 1). The two highest intensity ion transitions were selected as the quantification and confirmation ion pairs. Source parameters including voltage,

temperature and gas flow rates, were subsequently optimized with flow injection analysis as described in the experimental section.

### 2.2. HPLC Optimization

Chromatographic separation, despite the advantages of using tandem mass spectrometry, remains necessary for urinalysis to minimize interferences including those that alter ionization efficiencies and those that have similar fragmentation patterns. The potential for interferences in heightened in RCC patients who may suffer from impaired renal function, leading to clearance of normally-retained physiological biomolecules. For example, the Human Metabolome Database lists several naturally occurring metabolites with equivalent precursor ions to the selected RCC biomarkers such as cysteine and 4-hydroxyproline. For this reason, the four analytes were additionally optimized with respect to chromatographic separation to provide superior sensitivity and accuracy in urine matrices.

Polar-capped reversed-phase columns were evaluated based on previously developed methods for separation of similarly polar metabolites[38-40]. Specifically, a Synergi POLAR-RP (4.0 µm, 2.0 × 150 mm, Phenomenex, USA), a Luna phenyl-hexyl (3.0 µm, 3.0 × 150 mm, Phenomenex, USA), and a Synergi Fusion-RP column (4.0 µm,3.0 × 150 mm, Phenomenex, USA) were examined for their ability to effective retain and separate the selected RCC biomarkers. The Luna phenyl-hexyl column afforded acceptable retention of 4-hydroxybenzoic acid and gentisic acid, but failed to retain quinolinic acid and α-ketoglutaric acid. The Synergi POLAR-RP column was unable to provide sufficient separation and retention for all four analytes. Meanwhile, the Synergi Fusion-RP column effectively retained and separated all four RCC biomarkers (Figure 1).

Table 1. Optimized MS/MS parameters for selected RCC biomarkers.

| Compounds | Ion Pairs (m/z) | Declustering Potential (DP, V) | Collision Energy (CE, V) | Collision Cell Potential (CXP, V) | Entrance Potential (EP, V) |
|---|---|---|---|---|---|
| **Quinolinic acid** | 165.9/121.9 | -30 | -14 | -7 | -10 |
| | 165.9/78.0 | -30 | -20 | -3 | -10 |
| **4-Hydroxybenzoic** | 136.9/93.0 | -35 | -22 | -5 | -10 |
| **acid** | 136.9/65.2 | -35 | -42 | -1 | -10 |
| **Gentisic acid** | 152.9/107.9 | -20 | -30 | -7 | -10 |
| | 152.9/108.9 | -20 | -20 | -5 | -10 |
| **α-Ketoglutaric acid** | 144.9/101.0 | -35 | -12 | -5 | -10 |
| | 144.9/57.0 | -35 | -18 | -1 | -10 |

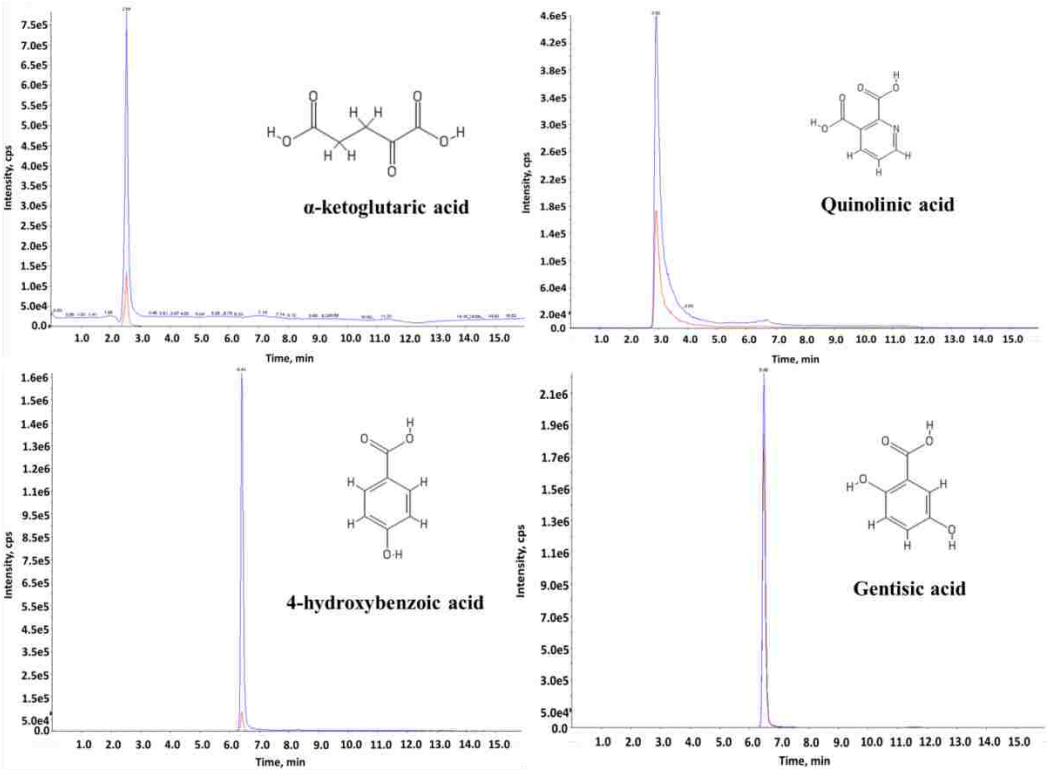


Figure 1. Extracted-ion chromatograms (XIC) for the quantitation and confirmation MRM transitions for each of the candidate RCC biomarkers prepared at 500 ng/mL in 1% synthetic urine using the newly developed HPLC-MS/MS method. Separation parameters: Column: Synergi Fusion reverse phase (4.0 µm, 3.0 × 150 mm); flow rate: 0.4 mL/min; injection volume: 50 µL; mobile phase: 0.5% formic acid in ultrapure water and 0.5% formic acid in methanol.

Following column selection, formic acid additive concentrations were optimized for chromatographic separation. Lower concentrations (<0.5% v/v) resulted in quinolinic acid peak broadening, prompting the selection of 0.5% formic acid in the final methodology. A representative chromatogram of a real 100-fold diluted urine sample has been shown in Figure 2. The occurrence of system peaks next to analyte peaks in real urine samples prompted us to investigate whether these additional peaks may represent spurious system peaks and/or analyte splitting. A spiked recovery study using variable

spiked concentrations was performed to confirm linear responses by the desired analyte peaks while the additional, spurious peaks remain unchanged. These results indicated these additional peaks had no impact on the accuracy of the newly developed method.

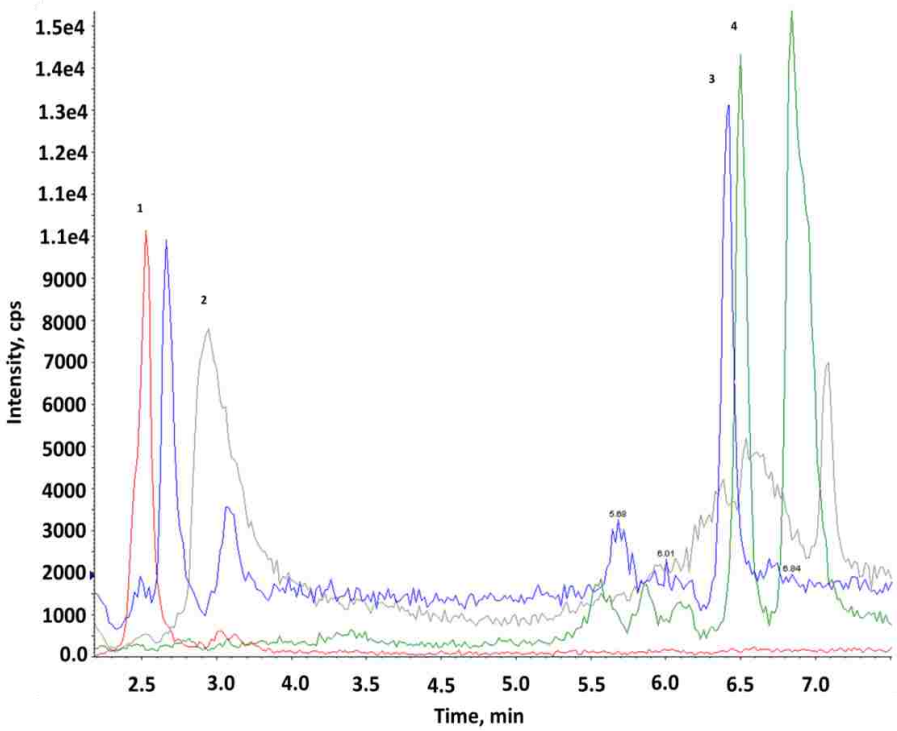


Figure 2. Representative chromatogram of a 100-fold diluted urine specimen. Analyte peaks are labeled as follows: 1. α-Ketoglutaric acid; 2. Quinolinic acid; 3. 4-Hydroxybenzoic acid; 4. Gentisic acid.

### 2.3. Method Performance

The newly developed method was rigorously validated with conventional figures of merit including determination of instrumental detection limits, method detection limits, limits of quantification, linearity, spiked recovery studies, measures of intra- and inter-day precision, and application to real urine specimens. Calibration standards were spiked into a pooled urine specimen for matrix matching purposes and were quantified using the

standard addition method. The resulting calibration curve was used to determine linearity, operating linear range, and detection limits. The calibration range was set between 0.001 ng/mL and 1000 ng/mL to encompass anticipated urinary ranges following a 100-fold dilution. Limits of quantification (S/N > 10) ranged from 0.05 ng/mL for gentisic acid to 1 ng/mL for quinolinic acid. Linear ranges were set at the limit of quantification to the upper limit of the calibration range (1000 ng/mL) and were found to have excellent linearity within these ranges ($R^2 > 0.9997$). Linear regression analyses for the calibration curves and method performance parameters for each analyte have been summarized in Table 2. Spiked recovery studies (n = 3) were performed to determine accuracy and precision in biologically relevant sample matrices and anticipated analyte concentrations. These experiments indicated the newly developed method was highly accurate (88.6%-114.8%) and precise (0.4% - 9.3% RSD) as shown in Table 3. Method precision was also assessed with intra- and inter-day variations using real urine specimens. These tests indicated acceptable intraday variance (1.2% - 2.8% RSD) and interday variance (2.4% - 5.1%). Together the figures of merit suggest the newly developed technique is sufficiently sensitive, selective, and reproducible for analyte quantification in urine matrices.

**2.4. Urine Sample Analysis**

Clinical applicability of the newly developed HPLC-MS/MS method was demonstrated in urine specimens collected from clinically relevant screening populations. This component of the study did not aim to generate or confirm any biological hypothesis, but merely aimed to demonstrate the technique was applicable in both healthy and pathological RCC urine specimens. The low prevalence of RCC in the local patient

Table 2. Method performance parameters for the newly developed HPLC-MS/MS technique including linear range and equations, standard deviation of slope, standard deviation of the intercept, standard deviation of residues, quantifiaction limits, detection limits, and retention times.

| Compounds | Calibration Range (ng/mL) | Linear Equation | Standard Deviation of Slope | Standard Deviation of Intercept | Standard Deviation of Residues | $R^2$ | Quantification Limit (ng/mL) | Method Detection Limit (ng/mL) | Retention Time (min) |
|---|---|---|---|---|---|---|---|---|---|
| **α-Ketoglutaric acid** | 1.0-1000 | y = 1401.9x - 3558.1 | 13 | 4966 | 1554 | 0.9999 | 1.0 | 0.75 | 2.53 ± 0.05 |
| **Quinolinic acid** | 2.5-1000 | y = 5913.7x - 16852 | 91 | 36867 | 12097 | 0.9998 | 2.5 | 1.0 | 2.92 ± 0.04 |
| **4-Hydroxybenzoic acid** | 0.75-1000 | y = 2773.6x - 8497.9 | 51 | 18648 | 5580 | 0.9997 | 0.75 | 0.25 | 6.40 ± 0.03 |
| **Gentisic acid** | 0.25-1000 | y = 11359x - 4475.9 | 65 | 21488 | 5937 | 0.9999 | 0.25 | 0.05 | 6.45 ± 0.04 |

†These values denote concentrations in undiluted urine.

††Two samples were diluted 200-fold due concentrations that exceeded the linear range.

Table 3. Accuracy and precision of the newly developed HPLC-MS/MS method. All values are presented as a percentage.

| | **Low (10 ng/mL)** | | **Medium (50 ng/mL)** | | **High (250 ng/mL)** | | **Intraday Variation** | **Interday Variation** |
|---|---|---|---|---|---|---|---|---|
| **Compounds** | Recovery | RSD | Recovery | RSD | Recovery | RSD | RSD | RSD |
| **α-Ketoglutaric acid** | 92.9 | 6.7 | 105.6 | 5.7 | 100.4 | 0.4 | 2.8 | 5.1 |
| **Quinolinic acid** | 112.0 | 4.8 | 108.4 | 9.3 | 114.8 | 4.5 | 2.1 | 4.9 |
| **4-hydroxybenzoic acid** | 99.9 | 8.1 | 94.4 | 2.2 | 88.6 | 6.1 | 1.8 | 2.4 |
| **Gentisic acid** | 107.5 | 6.3 | 104.4 | 6.7 | 108.3 | 8.4 | 1.2 | 3.1 |

population hindered efforts to accrue a statistically significant number of RCC patients. For this reason, a total of 27 urine samples ($N_{RCC}$ = 3; $N_{healthy}$ = 24) were analyzed in this study. Larger study populations will be necessary to generate meaningful statistical conclusions regarding the clinical applicability of these four compounds in RCC detection and diagnosis. Importantly, all four compounds were successfully quantified (S/N > 10) in 100-fold diluted urine from both RCC patients and healthy individuals, indicating the technique can be readily used for quantification of the four analytes without additional, potentially interfering, preparative techniques. Specifically, dilution-corrected mean values for quinolinic acid, 4-hydroxybenzoic acid, gentisic acid, and α-ketoglutaric acid were 3,440 ng/mL, 1,134 ng/mL, 547 ng/mL, and 24,830 ng/mL, respectively. These concentrations are consistent with previously reported urinary levels for these compounds[41-43]. However, urinary analytes must be further adjusted to reflect urine concentration-dilution resulting from patient hydration status and time since last urination. Urinary creatinine has been conventionally used for this purpose, but there are serious drawbacks to this approach. Creatinine is correlated with muscle mass and consequently age, gender, physical activity, diet, and disease status among other factors[44]. In this study, urinary creatinine differed dramatically in the healthy control population consisting of young, physically active males compared with the RCC urine specimens, which may result in over-normalization in the healthy group. Age- and gender-matching can reduce this error but cannot account for physical activity, diet, and disease status. For this reason, urine specific gravity, a correlate of total dissolved solids in urine, was used as an alternative normalization factor. Urine specific gravity has been recently proposed as a useful normalization factor for biomarker screenings in

populations and diseases where creatinine normalization may be inappropriate[45]. Notably, the urine specific gravity levels measured in this study (mean: 1.017; range: 1.003 - 1.033) matched general population statistics for urine specific gravity, suggesting creatinine-based normalization of these four analytes may result in inaccurate determinations due to differences in patient muscle mass and physical activity. The serum protein, cystatin C, has also been proposed as a highly effective urinary biomarker normalization factor in damaged kidneys, although it was not evaluated in this study due to a lack of corresponding serum samples[46]. The USG-adjusted mean values for quinolinic acid, 4-hydroxybenzoic acid, gentisic acid, and α-ketoglutaric acid were 4,060 ng/mL, 1,338 ng/mL, 645 ng/mL, and 29,300 ng/mL, respectively, which remained consistent with previous reports. Briefly, group comparisons were made using two-tailed 2-sample Student's t-Test and the USG-normalized data, although the sample size effectively limits any conclusions rendered here. In this limited study, compounds were found to be higher in RCC, including α-ketoglutaric acid ($\mu_{RCC}$ = 35,231 ng/mL, $\mu_{healthy}$ = 29,300 ng/mL, *P-value* = 0.336), quinolinic acid ($\mu_{RCC}$ = 5,960 ng/mL, $\mu_{healthy}$ = 4,060 ng/mL, *P-value* = 0.140), 4-hydroxybenzoic acid ($\mu_{RCC}$ = 3,126 ng/mL, $\mu_{healthy}$ = 1,338 ng/mL, *P-value* = 0.185), and gentisic acid ($\mu_{RCC}$ = 1,457 ng/mL, $\mu_{healthy}$ = 645 ng/mL, *P-value* = 0.271). However, further validation using statistically appropriate sample sizes are needed to generate useful statistical conclusions.

# 3. EXPERIMENTAL

## 3.1. Chemicals

Standard reagents quinolinic acid, 4-hydroxybenzoic acid, gentisic acid, and α-ketoglutaric acid as well as mobile phase additives ammonium formate (LC-MS grade), ammonium acetate (LC-MS grade), acetic acid (LC-MS grade) and formic acid (MS grade) were purchased from Sigma-Aldrich (St Louis, MO, USA). Acetonitrile (LC-MS grade) and methanol (MS grade) were obtained from Fischer Scientific (Pittsburgh, PA, USA). Ultrapure water was obtained using a Milli-Q Advantage A10 and Millipore Elix® water purification system (Millipore, MA, USA).

## 3.2. Standard Preparation

Dry chemical standards were stored at -20 °C from which stock solutions of 1000 µg/mL were prepared with ultrapure water. Individual stock solutions were stored at 4 °C for no more than three months under dark conditions. Working stock solutions were freshly prepared from serial dilution with ultrapure water. Calibration standards ranging from 0.001 ng/mL to 1,000 ng/mL were prepared in a 100-fold diluted pooled urine sample.

## 3.3. HPLC-MS/MS Instrumentation

A Synergi Fusion reversed-phase column (4.0 µm, 3.0 × 150 mm, Phenomenex, USA) and a Shimadzu UFLC system (Columbia, MD) consisting of a vacuum degasser (DGU-30A3), two pumps (LC-20 AD XR), an auto sampler (SIL-20AC XR), and a column oven (CTO-20A) were used for separation. HPLC separation was conducted at

0.4 mL/min at 25 °C using a 50 µL injection volume. Compound separation was enhanced by using a binary gradient system comprised of A: 0.5% formic acid in ultrapure water and B: 0.5% formic acid in methanol. The gradient program was initialized at 5% B for two minutes followed by a linear increase of B to 40% over two minutes. The 40% B composition was held for one minute followed by a linear increase to 80% B in two minutes where it was held for an additional one minute. The B composition was dropped to 5% in one minute and held for six and half minutes. The total run-to-run time was 16 minutes.

A 4000 QTRAP mass spectrometer (AB SCIEX, Foster City, CA) was used to quantitate the selected RCC biomarkers. The mass spectrometer was operated in multiple-reaction mode (MRM) under negative-ion ESI conditions. Nitrogen was used as the curtain and cone gases. Optimized ESI parameters included: curtain gas: 35 psi; ion spray voltage: -4500V; GS1: 35 psi; GS2: 50 psi; temperature: 450˚C. The MS/MS collision gas was set at 6 psi.

### 3.4. Method Validation

Urine represents a biologically complex matrix that presents significant bioanalytical challenges. Therefore, the newly developed method was validated through several figures of merit including: instrumental limit of detection, method detection limit, linearity, intra- and inter-day variance estimation, and performance in spiked recovery tests to yield precision and accuracy information. All analyses were run as analytical triplicates.

### 3.5. Urine Analysis

Urine samples ($N$ = 27) were collected and subsequently analyzed by the newly developed technique to demonstrate clinical applicability. Pathological RCC specimens ($N$ = 3) were provided by the Central Missouri Urology Clinic (Rolla, MO) and healthy urine specimens ($N$ = 24) were collected from consenting Missouri University of Science and Technology undergraduate and graduate students. Additional collection of RCC specimens was hindered by the relative rarity of RCC in the local rural population. All study participants provided written consent, and the collection was approved by the Institutional Review Board at Missouri University of Science and Technology. Pathologic specimens originated from three males aged 49, 67, and 85 years-old with staged RCC. These individuals had no confounding morbidities and had not received prior treatment to their new diagnoses. Twenty-four control samples were additionally sampled from healthy individuals ranging from 21 to 59 years of age with no history of malignancy and no current illnesses. Urine specimens were collected on-site and immediately stored in a -80 ˚C ultralow freezer for approximately one to six weeks prior to analysis. Upon complete thawing to room temperature, a 1 mL aliquot was centrifuged at 3000 *g*-force for 20 minutes at 4 °C. The supernatant was additionally filtered with a 0.22 µm nylon membrane filter to remove any proteins or cells from the urine. Filtered samples were diluted to a final dilution factor of 100 with ultrapure water for analysis.

## 4. CONCLUSION

A targeted, quantitative HPLC-MS/MS method was developed for simultaneous determination of quinolinic acid, 4-hydroxybenzoic acid, gentisic acid and α-ketoglutaric

acid in urine, which has not been previously reported to the best of our knowledge. The newly developed method was validated by multiple conventional figures of merit including method detection limits (0.05 ng/mL to 1 ng/mL), spiked recovery studies that indicated high accuracy (88.6% - 114.8%) and reproducibility (0.4 – 9.3% RSD), and acceptable intraday variance (1.2% - 2.8% RSD) and interday variance (2.4% - 5.1%) The applicability of the newly developed method was further demonstrated in 27 urine specimens from healthy individuals in addition to several RCC patients. All four compounds were successfully quantified in urine samples at concentrations were in agreement with previous findings. Together these findings suggest the new method can be considered sensitive, selective, and highly accurate, enabling researchers to evaluate the clinical applicability of these four urinary markers for earlier RCC detection and diagnosis. Although higher concentration levels in RCC samples were observed in our small sample set, larger study populations will be required to generate statistically significant conclusions regarding the clinical applicability of these four compounds. We therefore anticipate this method to significantly benefit clinical researchers aiming to perform epidemiological studies for these four compounds and to elucidate their roles in disease.

## ACKNOWLEDGEMENTS

This project was supported by the Center for Single Nanoparticle, Single Cell, and Single Molecule Monitoring at Missouri University of Science and Technology. C. Burton received financial support from a National Science Foundation Graduate Research Fellowship under Grant No. #DGE-1011744. The authors would like to express their

appreciation toward the staff at the Central Missouri Urology Clinic. Finally, special thanks are given to Qihua Wu and Ruipu Mu for constructive discussions.

## REFERENCE

1. Howlader, N., et al., *SEER Cancer Statistics Review, 1975–2011*. 2013, National Cancer Institute. Bethesda, MD, http://seer. cancer. gov/csr/1975_2011/, based on November.

2. Jayson, M. and H. Sanders, *Increased incidence of serendipitously discovered renal cell carcinoma.* Urology, 1998. **51**(2): p. 203-205.

3. Chow, W.-H., et al., *Rising incidence of renal cell cancer in the United States.* Jama, 1999. **281**(17): p. 1628-1631.

4. Luciani, L.G., R. Cestari, and C. Tallarigo, *Incidental renal cell carcinoma—age and stage characterization and clinical implications: study of 1092 patients (1982–1997).* Urology, 2000. **56**(1): p. 58-62.

5. Tosaka, A., et al., *Incidence and properties of renal masses and asymptomatic renal cell carcinoma detected by abdominal ultrasonography.* The Journal of urology, 1990. **144**(5): p. 1097-1099.

6. Wang, C., et al., *Diagnostic accuracy of contrast-enhanced ultrasound for renal cell carcinoma: a meta-analysis.* Tumor Biology, 2014: p. 1-8.

7. Wagstaff, P., et al., *The role of imaging in the active surveillance of small renal masses.* Current urology reports, 2014. **15**(3): p. 1-8.

8. Volpe, A., et al., *The natural history of incidentally detected small renal masses.* Cancer, 2004. **100**(4): p. 738-745.

9. Lane, B.R., C.M. Tobert, and C.B. Riedinger, *Growth kinetics and active surveillance for small renal masses.* Current opinion in urology, 2012. **22**(5): p. 353-359.

10. Motzer, R.J., et al., *Kidney cancer.* Journal of the National Comprehensive Cancer Network, 2009. **7**(6): p. 618-630.

11. Ozsoy, O., et al., *Incidental detection of synchronous primary tumours during staging workup for prostate cancer.* Swiss Med Wkly, 2010. **140**(15-16): p. 233-236.

12. Palsdottir, H.B., et al., *Incidental detection of renal cell carcinoma is an independent prognostic marker: results of a long-term, whole population study.* The Journal of urology, 2012. **187**(1): p. 48-53.

13. Bennett, B.D., et al., *Absolute metabolite concentrations and implied enzyme active site occupancy in Escherichia coli.* Nature chemical biology, 2009. **5**(8): p. 593-599.

14. Amantonico, A., P.L. Urban, and R. Zenobi, *Analytical techniques for single-cell metabolomics: state of the art and trends.* Analytical and bioanalytical chemistry, 2010. **398**(6): p. 2493-2504.

15. Theodorescu, D., et al., *Discovery and validation of new protein biomarkers for urothelial cancer: a prospective analysis.* The lancet oncology, 2006. **7**(3): p. 230-240.

16. Thongboonkerd, V. and P. Malasit, *Renal and urinary proteomics: current applications and challenges.* Proteomics, 2005. **5**(4): p. 1033-1042.

17. Catchpole, G., et al., *Metabolic profiling reveals key metabolic features of renal cell carcinoma.* Journal of cellular and molecular medicine, 2011. **15**(1): p. 109-118.

18. Gao, H., et al., *Metabonomic profiling of renal cell carcinoma: high-resolution proton nuclear magnetic resonance spectroscopy of human serum with multivariate data analysis.* Analytica chimica acta, 2008. **624**(2): p. 269-277.

19. Zira, A.N., et al., *1H NMR metabonomic analysis in renal cell carcinoma: a possible diagnostic tool.* Journal of proteome research, 2010. **9**(8): p. 4038-4044.

20. Lin, L., et al., *LC-MS based serum metabonomic analysis for renal cell carcinoma diagnosis, staging, and biomarker discovery.* Journal of proteome research, 2011. **10**(3): p. 1396-1405.

21. Kim, K., et al., *Urine metabolomic analysis identifies potential biomarkers and pathogenic pathways in kidney cancer.* Omics: a journal of integrative biology, 2011. **15**(5): p. 293-303.

22. Ganti, S., et al., *Kidney tumor biomarkers revealed by simultaneous multiple matrix metabolomics analysis.* Cancer research, 2012. **72**(14): p. 3471-3479.

23. Ganti, S. and R.H. Weiss. *Urine metabolomics for kidney cancer detection and biomarker discovery*. in *Urologic Oncology: Seminars and Original Investigations*. 2011. Elsevier.

24. Yoshimura, H., et al., *Effects of kynurenine metabolites on mesangial cell proliferation and gene expression.* Experimental and molecular pathology, 2009. **87**(1): p. 70-75.

25. Warburg, O., *On the origin of cancer cells.* Science, 1956. **123**(3191): p. 309-314.

26. Perroud, B., et al., *Grade-dependent proteomics characterization of kidney cancer.* Molecular & Cellular Proteomics, 2009. **8**(5): p. 971-985.

27. Popov, A. and J.L. Schultze, *IDO-expressing regulatory dendritic cells in cancer and chronic infection.* Journal of molecular medicine, 2008. **86**(2): p. 145-160.

28. Chen, W., *IDO: more than an enzyme.* Nature immunology, 2011. **12**(9): p. 809-811.

29. Wettersten, H.I. and R.H. Weiss, *Potential biofluid markers and treatment targets for renal cell carcinoma.* Nature Reviews Urology, 2013. **10**(6): p. 336-344.

30. Suzuki, Y., et al., *Increased serum kynurenine/tryptophan ratio correlates with disease progression in lung cancer.* Lung Cancer, 2010. **67**(3): p. 361-365.

31. Ashidate, K., et al., *Gentisic acid, an aspirin metabolite, inhibits oxidation of low-density lipoprotein and the formation of cholesterol ester hydroperoxides in human plasma.* European journal of pharmacology, 2005. **513**(3): p. 173-179.

32. Meinitzer, A., et al., *Development of a liquid chromatography–mass spectrometry method for the determination of the neurotoxic quinolinic acid in human serum.* Clinica Chimica Acta, 2014. **436**: p. 268-272.

33. Jian-Hua, L. and P.C. Smith, *Direct analysis of salicylic acid, salicyl acyl glucuronide, salicyluric acid and gentisic acid in human plasma and urine by high-performance liquid chromatography.* Journal of Chromatography B: Biomedical Sciences and Applications, 1996. **675**(1): p. 61-70.

34. Michail, K., et al., *Development and validation of a liquid chromatographic method for the determination of hydroxymethylfurfural and alpha-ketoglutaric acid in human plasma.* Analytica chimica acta, 2007. **581**(2): p. 287-297.

35. Zhang, K. and Y. Zuo, *GC-MS determination of flavonoids and phenolic and benzoic acids in human plasma after consumption of cranberry juice.* Journal of agricultural and food chemistry, 2004. **52**(2): p. 222-227.

36. Smythe, G.A., et al., *ECNI GC-MS analysis of picolinic and quinolinic acids and their amides in human plasma, CSF, and brain tissue*, in *Developments in Tryptophan and Serotonin Metabolism*. 2003, Springer. p. 705-712.

37. Horning, E. and M. Horning, *Human metabolic profiles obtained by GC and GC/MS.* Journal of Chromatographic Science, 1971. **9**(3): p. 129-140.

38. Crow, B., et al., *Analysis of urinary aromatic acids by liquid chromatography tandem mass spectrometry.* Biomedical Chromatography, 2008. **22**(12): p. 1346-1353.

39. Magiera, S., et al., *A liquid chromatography and tandem mass spectrometry method for the determination of potential biomarkers of cardiovascular disease.* Journal of Chromatography B, 2013. **919**: p. 20-29.

40. Möller, M., J.L. Du Preez, and B.H. Harvey, *Development and validation of a single analytical method for the determination of tryptophan, and its kynurenine metabolites in rat plasma.* Journal of Chromatography B, 2012. **898**: p. 121-129.

41. Sriboonvorakul, N., et al., *Liquid chromatographic–mass spectrometric method for simultaneous determination of small organic acids potentially contributing to acidosis in severe malaria.* Journal of Chromatography B, 2013. **941**: p. 116-122.

42. Zaugg, S., et al., *Determination of salicylate, gentisic acid and salicyluric acid in human urine by capillary electrophoresis with laser-induced fluorescence detection.* Journal of Chromatography B: Biomedical Sciences and Applications, 2001. **752**(1): p. 17-31.

43. Lord, R., et al., *Weekly Biological Variability of Urinary Organic Acids.* North American Journal of Medicine and Science Jul, 2012. **5**(3): p. 149.

44. Heymsfield, S., et al., *Measurement of muscle mass in humans: validity of the 24-hour urinary creatinine method.* The American Journal of Clinical Nutrition, 1983. **37**(3): p. 478-494.

45. Burton, C., H. Shi, and Y. Ma, *Normalization of urinary pteridines by urine specific gravity for early cancer detection.* Clinica Chimica Acta, 2014. **435**: p. 42-47.

46. Hojs, R., et al., *Serum cystatin C as an endogenous marker of renal function in patients with mild to moderate impairment of kidney function.* Nephrology Dialysis Transplantation, 2006. **21**(7): p. 1855-1862.

# SECTION

# 2. MATERIALS AND METHODS

## 2.1. POROUS WALL HOLLOW GLASS MICROSPHERES

The porous wall hollow glass microspheres (PWHGMs) used in this study were provided by MoSci Corporation (Rolla, MO). They consist of a spherical 1-μm thick silicate glass shells that enclose spherical central hollow cavities with a diameter that ranges from 20 μm to 75 μm. The 1-μm thick shells are penetrated by pores with tortuous channels that can range from 10 to 300 nm in diameter. The microspheres, their surface, and their pore sizes were characterized by field emission scanning electron microscopy (FESEM) (Hitachi 4700, Tokyo, Japan). Figure 2.1 shows electron micrographs of PWHGMs, their spherical hollow cavities, and the differently sized pores in the walls. The FESEM images confirm that the PWHGMs are indeed spherical with a smooth outer surface (Figure 2.1a). In some cases, there are pieces of broken microspheres attached to the surfaces of the intact microspheres. The diameters of the microspheres range from 20 μm to 70 μm. A broken microsphere shell was also imaged by FESEM to show the central hollow cavity (Figure 2.1b). Higher magnification of a microsphere shell showed many indentations on the surface, which are identified with the pores through the outer walls (Figure 2.1c & Figure 2.1d). The pores are only visible as indentations because gold sputtering, which was used to prepare the microspheres for FESEM imaging, closed the pores. There are two distinct size ranges of the pores: (a) a small number of relatively large pores as shown in Figure 2.1d with a diameter between 50 nm and 75 nm, and (b) a great number of small pores with sizes between 10 nm and 20 nm. The substantial

difference between the large and small pores sizes and the lack of a continuous distribution of pore sizes has a major effect on the release of material from the microspheres as shown later in the kinetic study presented in this dissertation. Overall, the pores and the spherical hollow cavity are characteristic for PWHGMs, making them distinguishable from other glass microspheres.

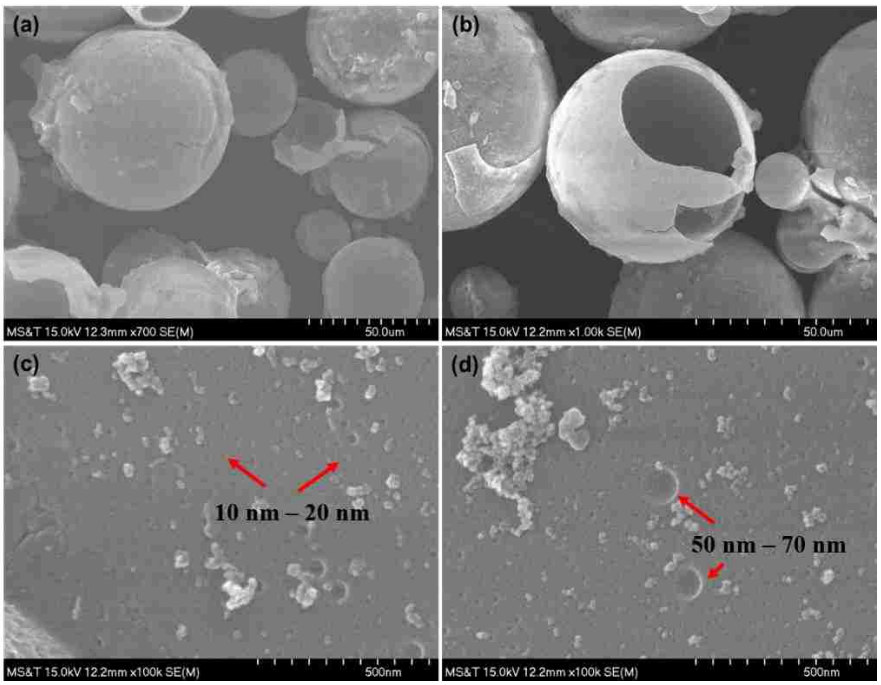


Figure 2.1. SEM images of microspheres. (a): the surface of microspheres; (b): the central hollow cavity; (c) and (d): the pores on the wall.

## 2.2. NMR INSTRUMENTATION AND SPECTRA ACQUISITION, PROCESSING, AND PEAK ASSIGNMENTS

All $^{1}$H-NMR spectra presented in this dissertation were obtained using a 5-mm broadband probe with z-gradient in the departmental 400 MHz Bruker AVANCE III HD NMR Spectrometer. The data were acquired with the following acquisition parameters:

- sample temperature: 298 K

- spectral width: 4800 Hz
- number of data points: 32 k
- pulse width: 14.3 µs
- recovery delay between scans: 2 s
- number of scans: 16

After acquisition, the $^{1}$H-NMR spectra were phase- and baseline-corrected with automated routines of the spectrometer's TOPSPIN® 3.1 software. In some cases, manual refinement of the phase and baseline corrections was necessary to obtain optimized spectra. The peak assignments are listed in the Table 2.1 below.

Table 2.1. $^{1}$H chemical shifts assignments

| Chemicals | Chemical shift (ppm) | Chemicals | Chemical shift (ppm) |
|---|---|---|---|
| $H_2O$ | 4.63 | $CHCl_3$ emulsion in $D_2O$ | 7.20 |
| HOD | 4.63 | $CH_3COOH$ | 1.84 |
| $CH_3(CH_2)_{10}CH_3$ emulsion in $D_2O$ | 0.76 | $(CH_3)_2CHOH$ | 0.92 |
| $CH_3(CH_2)_{10}CH_3$ phase-separate in $D_2O$ | 0.95 | $(CH_3)_2CHOH$ | 3.76 |
| $CH_3(CH_2)_{10}CH_3$ emulsion in $D_2O$ | 1.17 | $(CH_3)_2CHOOCCH_3$ | 0.99 |
| $CH_3(CH_2)_{10}CH_3$ phase-separate in $D_2O$ | 1.35 | $(CH_3)_2CHOOCCH_3$ | 4.72 |
| $CHCl_3$ dissolved in $D_2O$ | 7.55 | $(CH_3)_2CHOOCCH_3$ | 1.81 |

There are two sets of peaks for $C_{12}H_{26}$ in $D_2O$ as well as for $CHCl_3$ in $D_2O$. The reason is that $C_{12}H_{26}$ has a very low solubility in water ($3.7 \times 10^{-9}$ g/mL at 25 °C [110]), and so does $CHCl_3$ ($8.1 \times 10^{-3}$ g/mL at 25 °C [111]). Hence, $C_{12}H_{26}$ or $CHCl_3$ in excess of the low solubility will form emulsified (i.e., colloidal) particles in solution. The formation of emulsified colloids in the mixture of $CHCl_3$ in $D_2O$ will be used as the example to explain the two NMR peaks (Table 2.1). An emulsion is an unstable system that consists of at least two immiscible liquid phases (Figure 2.2). When very small amounts of $CHCl_3$ are mixed with $D_2O$ (< 5 µL in 750 µL $D_2O$) a real solution without emulsified $CHCl_3$ will form. After saturation of $D_2O$ with $CHCl_3$, however, further $CHCl_3$ will form emulsified colloids as shown schematically in Figure 2.3. Because of the different chemical environment of molecularly dissolved $CHCl_3$ and emulsified $CHCl_3$, two signals of different chemical shift are expected, and observed, in the NMR spectra, i.e., one for the molecularly dissolved and one for the emulsified species.

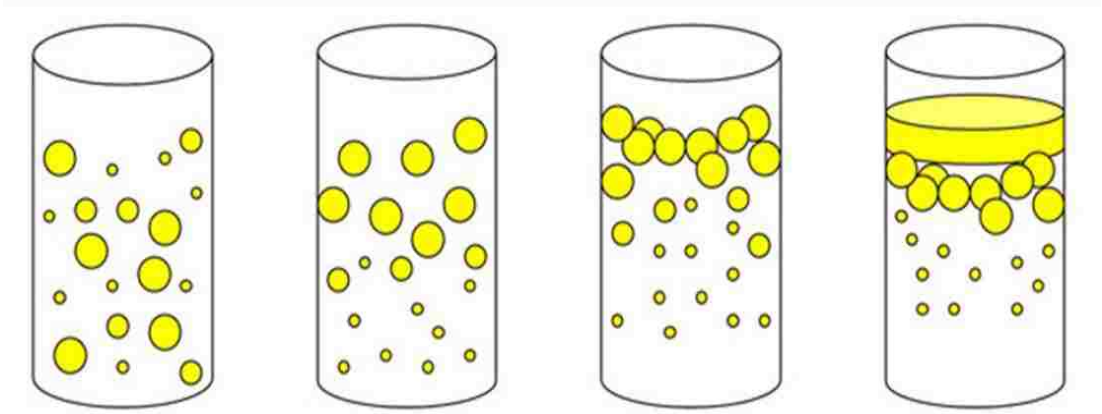

Figure 2.2. Illustration of emulsion. Emulsions have different stability characteristics and there are applications that demand varying levels of emulsification stability. From left to right: a stable emulsion; the emulsion has begun to separate; further separation; the emulsion is creaming. Adapted from ref [112].

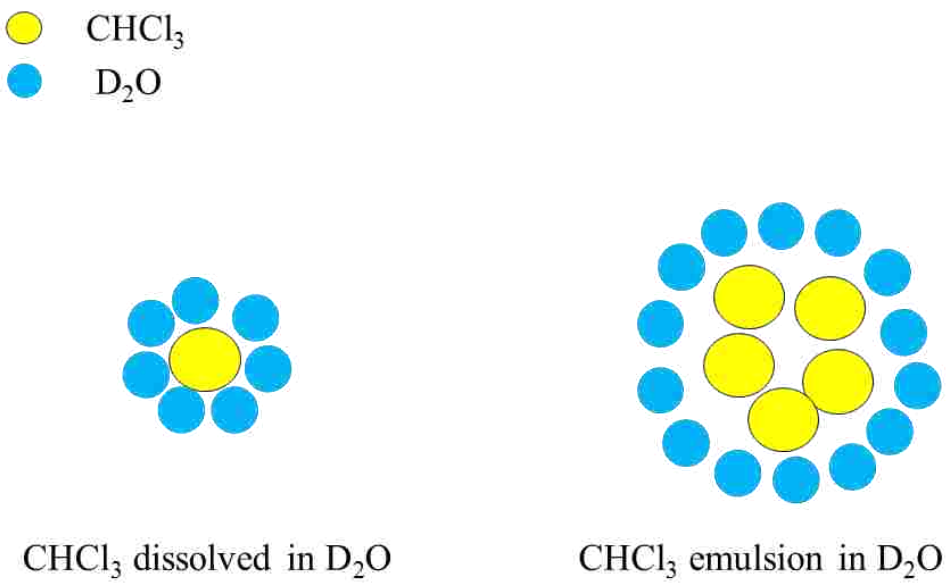


Figure 2.3. Dissolved $CHCl_3$ in $D_2O$ and emulsified $CHCl_3$ in $D_2O$.

## 2.3. DEVELOPMENT OF LOADING SYSTEM

The vacuum-based loading system is considered novel at this point because it is the first time loading PWHGMs with target materials through a vacuum-based system is reported. The newly developed procedure (Figure 2.4) for loading PWHGMs with liquid materials or materials dissolved in liquids is described in detail below:

1. A desired amount of glass microspheres is put into a glass vial.
2. The glass vial is connected to a standard laboratory vacuum pump with the flexible rubber hose that tightly fits over the vial. It is ensured that the rubber hose provides an air-tight seal with the vial.
3. The vacuum pump is turned on for about 1 hour to remove all air from the vial and with it from inside the hollow microspheres. The airflow must be controlled to be reasonably low in order to prevent microspheres from being floated out of the glass vial. In addition, the air flow toward the vacuum pump must be kept low, so that air

can escape from the microspheres without generating excessive pressure differences between the hollow cavity inside the microspheres and the surrounding atmosphere. The delicate microspheres tend to burst if air is removed too fast from the vial and the pressure difference becomes too large.

4. The material intended to be loaded into the hollow spheres is slowly injected through the rubber hose (or a separate septum) into the evacuated glass vial with a syringe. Depending on the volatility of the charging material, the vacuum pump can be left running (low-volatility materials) or must be turned off and separated from the vial system by a valve (high-volatility materials). It is advisable to inject as much material as is needed to completely submerge the microspheres with liquid.
5. The microspheres are left in the vial for 12-15 hours (e.g., overnight) to fully allow the inside of the microsphere cavities to equilibrate with the surrounding solution.

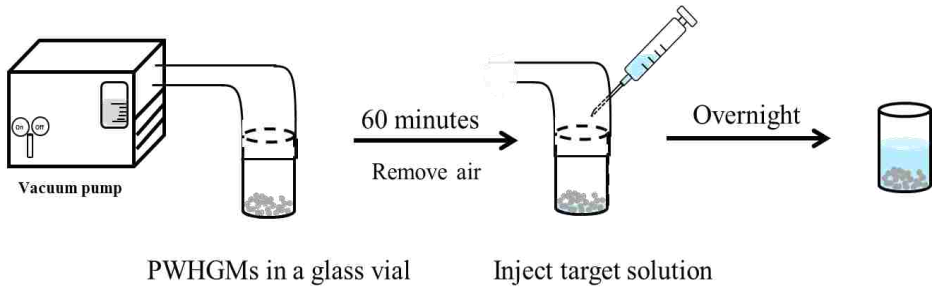


Figure 2.4. Schematic diagram of loading system. The integrated system consisted of a vacuum pump, a glass vial, rubber tube, and a syringe. The PWHGMs was included in the system

Pictures were taken with a digital camera before and after the PWHGMs were loaded with $H_2O$ (Figure 2.5a & Figure 2.5b). As shown in the pictures, unloaded microspheres filled with air float on top of the liquid phase (Figure 2.5a) whereas the

water-loaded microspheres sink to the bottom. Even though the $SiO_2$ of the glass microspheres, which is the main component of the microspheres' shells, has a higher density (2.2 g/cm$^3$ [113]) than most common liquids (e.g. $H_2O$: 0.9950 g/cm$^3$ [114]), the air inside the PWHGMs, which has a much lower density ($1.225 \times 10^{-3}$ g/cm$^3$ [115]), keeps the average density of unloaded microspheres below the density of most common liquid materials. Therefore, unloaded microspheres will float, for example, on top of water. On the contrary, microspheres charged with a liquid material will sink to the bottom (Figure 2.5b) due to a higher average density even if the liquid inside the microspheres has a considerably lower density that the surrounding fluid. Unloaded and loaded microspheres were imaged with inverted optical microscopy as shown in Figure 2.5c & Figure 2.5d. Because the refractive index is significantly different between air and liquid, the image of the unloaded microspheres looks very different from the one of the loaded microspheres. What appears to be a thick wall of the microspheres in Figure 2.5c is actually the result of the difference in refractive index between liquid ($H_2O$ in this case) and air. The spherical contours of the microspheres are clearly visible under the microscope even after the microspheres were filled with liquid. It shows that the loaded microspheres kept their integral structure, which indicates that the exerted pressure differences during the loading process did not break the microspheres. There are no air bubbles visible inside or outside the microspheres after loading them with liquid materials, which shows that a carefully executed vacuum-based loading system is a procedure that can be successfully applied to fill microspheres with target materials. To fill microspheres with solid components, the same procedure is applied with aqueous or organic-liquid solutions of the target material.

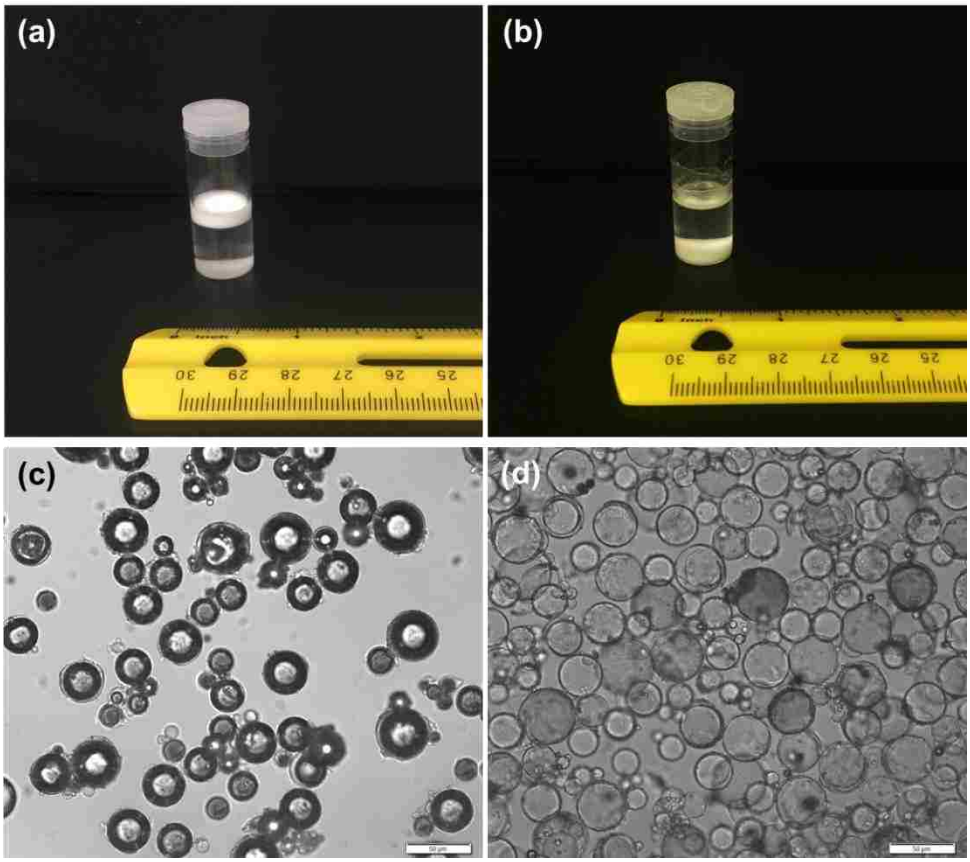


Figure 2.5. Images of microspheres before and after loading with $H_2O$. (a) unloaded microspheres floated in $H_2O$; (b) loaded microspheres sink down in $H_2O$; (c) inverted microscopic image of unloaded microspheres under white light; (d) inverted microscopic image of loaded microspheres under white light. The scale bar is 50 μm.

## 2.4. WASHING MICROSPHERES THROUGH CENTRIFUGATION PROCESS

To find NMR evidence of loaded materials inside of microspheres, any excess amount of target material must be removed from the surface of the microspheres. The target materials that reside outside of the microspheres will result in NMR signals of similar, if not the same chemical shift as the materials loaded inside. Therefore, a sufficient washing procedure removing all excess material including material attached to the outside of the microsphere shells must be applied before analysis. The proposed washing procedures utilized a solvent that is immiscible with the solution loaded inside

the microspheres. Because either n-dodecane or chloroform was loaded into the microspheres, $D_2O$ was chosen to wash the microspheres. The microspheres were washed with 1 mL portions of $D_2O$ followed by centrifugation of the solution. The supernatants collected after each washing were individually examined by NMR spectroscopy. The washing procedure was generally repeated 3 times, whereupon the microspheres were transferred into a 5 mm NMR tube filled with lock solvent ($D_2O$ in this example).

The washing effectiveness was evaluated first with the system $CHCl_3$ and $D_2O$. After microspheres were loaded with $CHCl_3$ through the loading procedures described in Section 2.3, they were transferred into a centrifuge tube (Eppendorf, NY). $D_2O$ was added and centrifugation executed. The supernatant was decanted from the centrifuge tube and transferred into an NMR tube for recording an NMR spectrum. Figure 2.6 shows the NMR spectra of the supernatants before and after three times washing with $D_2O$.

The spectra show that two peaks can be observed at 7.55 ppm and 7.20 ppm before the washing procedure, which are assigned to molecularly dissolved $CHCl_3$ and the colloidal $CHCl_3$ emulsion. The peak at 7.20 ppm indicates that there is $CHCl_3$ in excess of the dissolution limit of the molecular form present in the supernatant. After the third wash, however, no peak is observed at 7.20 ppm, which indicates that all of the colloidal $CHCl_3$ emulsion was removed and that only a small quantity of molecularly dissolved $CHCl_3$ remained in $D_2O$. These quantities could not completely be removed but may originate from material that leaks out of the microspheres during the final washing steps. The comparison of supernatants collected at different stages during the washing process demonstrates that a centrifugation-based washing procedure with solvents that

are virtually immiscible with the loaded material is effective to remove excess amount of target material loaded into microspheres.

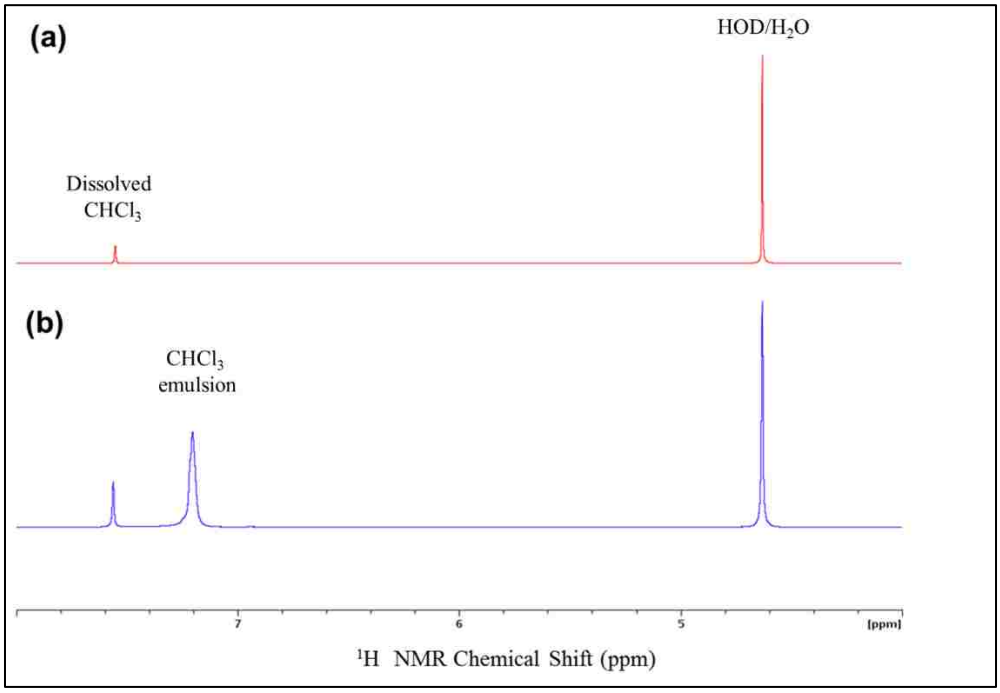


Figure 2.6. $^{1}H$ NMR spectra of supernatants collected during washing process. a) NMR spectrum of supernatant collected after three washes. b) NMR spectra of supernatants collected before washing. From the left to right peaks are assigned to dissolved $CHCl_3$, emulsified $CHCl_3$ and $HOD/H_2O$.

# 3. MODEL SYSTEM STUDIES

The development of new drugs and diagnostic biomarkers is expensive and time consuming. But it is not only the drug or biomarker formulation itself but also the way a drug or diagnostic biomarker is delivered that scientists have been looking into. Modern drug delivery systems are engineered strategies that can deliver drugs and biomarkers to target sites and release them in a controlled manner for therapeutic treatments or diagnostic applications, respectively. The major goal is to offer targeted delivery only to where the medication or diagnostic biomarker is needed, while leaving other sites unaffected. Targeted delivery minimizes the amount of drug or biomarker needed for the application and also reduces potentially toxic side effects. Specially designed drug and biomarker carriers are desired to administer the drugs very selectively. When designing a new drug delivery carrier, scientists are faced with questions of biocompatibility, quantification of the loaded drugs, and the release kinetics of the drugs from the carriers. The model systems studied in this work are designed to provide insights into the release mechanisms and kinetics of materials from the inner cavity of PWHGMs to the surrounding areas. These studies are the first of its kind and are necessary to understand the properties of PWHGMs before they can be put into practice as actual drug delivery carrier. In particular, three model systems are used to evaluate the potential of PWHGMs to be used as carriers in drug or biomarker delivery systems.

## 3.1. THE MOTIVATION OF THE INVESTIGATION INTO THE BINARY IMMISCIBLE SYSTEMS

Compounds used as drugs or biomarkers are most commonly organic compounds that can be divided into two categories, small organic molecules, and biologics (i.e. biological medical products). Many properties have to be taken into consideration during the development of new drugs or biomarkers, including structural properties (e.g. hydrogen bonding, polarity, functional groups, etc.), physicochemical properties (e.g. solubility, diffusivity, etc.), biochemical properties (e.g. metabolism, biodegradability etc.), as well as pharmacokinetics (PK) and toxicity (half-life, $LD_{50}$) [116]. However, drugs encounter many barriers in living system till they reach the therapeutic target. When a drug molecule passes through a barrier, the amount of drug molecules will most likely be reduced at the other side of barriers (Figure 3.1) [117]. Unfortunately, there are many barriers in a human body including membranes, adverse pH value, metabolic enzymes, and molecular transport vehicles or enzymes [118]. For example, orally administered drugs are first ingested via the esophagus arriving in the stomach where the pH ranges between 1.5 to 3.5 [119]. However, many drug molecules, especially biologics such as proteins will break down or decompose at such low pH and thus lose their functionalities. The solubility of drug molecules is another crucial factor in drug delivery. The drug's high or low solubility in aqueous or organic solvents determines how it will be absorbed by the body and how it may reach its designated area. Therefore, targeted drug or biomarker delivery techniques which utilize vehicles that can penetrate barriers more easily or even eliminate them have gained much attention in the development of drug carriers, particularly if they have the potential to protect drugs from decomposition or dysfunction in human body.

The model systems in this study use microspheres as carriers and $C_{12}H_{26}$ (n-dodecane) and $CHCl_3$ (chloroform) as loaded materials. $C_{12}H_{26}$ was chosen because it is an organic molecule with a very low solubility in water. Because the loaded materials were characterized with NMR spectroscopy, the straight and simple structure of $C_{12}H_{26}$ avoids the generation of too many signals in the $^1H$ NMR spectrum, which would make it more difficult to unambiguously assign all signals in the spectrum. $CHCl_3$ is a simpler chemical with only one type of $^1H$ nucleus (proton), which makes it easy to interpret NMR spectra quantitatively. The glass microspheres used as carrier and container of the chemicals are resistant to acidic solutions, which renders them particularly useful as drug carriers for acid-sensitive molecules.

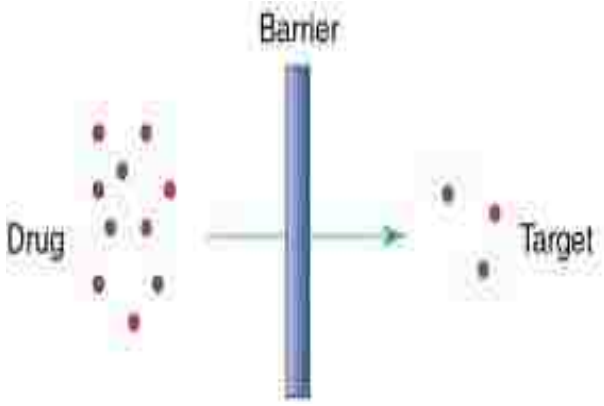


Figure 3.1. The number of active drug molecules is reduced during the passing of a barrier. Adapted in modified form from ref [117].

## 3.2. BINARY IMMISCIBLE SYSTEM OF $CHCl_3$ AND $D_2O$

The $CHCl_3$ and $D_2O$ system was studied first as a simple example of obtaining insights of binary immiscible system with NMR spectroscopy. CHCl3 only provides one proton NMR signal, which makes it easy to interpret data.

**3.2.1. Experiments Design and Procedures**. The control experiments of the two immiscible liquids $CHCl_3$ and $D_2O$ were first carried out by adding different amounts of $CHCl_3$ (1 µL, 3 µL, 5 µL, 15 µL, and 20 µL) to 750 µL $D_2O$ without the microspheres present. NMR spectra were recorded for every mixture. Thereafter, microspheres were loaded with $CHCl_3$ according to the vacuum-based loading system explained in section 2.3 and washed three times with $D_2O$ following the washing procedures mentioned in section 2.4. The final solution was transferred into a 5 mm NMR tube with the sample gently shaken before analysis to ensure that the microspheres were homogeneously distributed in the NMR active volume. NMR spectra of the microspheres loaded with $CHCl_3$ and suspended in $D_2O$ were recorded, and integrated signal intensities of the $CHCl_3$ peak was used for evaluation.

**3.2.2. Results and Discussion.** An important aspect for drug delivery with hollow glass microspheres is to know what compounds are loaded into the PWHGMs as well as the absolute amount and the concentrations of the loaded compounds. Therefore, an analytical technique like NMR is desired, which can determine and quantify loaded materials inside the PWHGMs. The series of control experiments was conducted to understand the binary immiscible system of $CHCl_3$ in $D_2O$. A narrow singlet peak is observed at 7.55 ppm when only 3 µL of $CHCl_3$ is added to the 750 µL of $D_2O$ (Figure 3.2). The solubility of $CHCl_3$ in water at 25 °C is $8.1 \times 10^{-3}$ g/mL [111], and it was calculated by the density of $CHCl_3$ (1.49 g/mL at 25 °C) that there was a molality of only $5.96 \times 10^{-3}$ g $CHCl_3$ per mL $D_2O$ when 3 µL of $CHCl_3$ was added to the 750 µL $D_2O$. Therefore, the 3 µL $CHCl_3$ was dissolved molecularly in $D_2O$, resulting in the narrow singlet peak at 7.55 ppm. The integral of the $CHCl_3$ singlet peak was 0.1318 relative to

the integral of the HOD peak at 4.63 ppm. As more $CHCl_3$ was added, the integral of the peak for the molecularly dissolved singlet $CHCl_3$ increased. The maximum solubility for $CHCl_3$ in 750 µL $D_2O$ was reached by adding 4.10 µL $CHCl_3$. Therefore, the peak for the molecularly dissolved $CHCl_3$ reached saturation with an integral of 0.1568 when 5 µL of $CHCl_3$ was added to 750 µL of $D_2O$. Meanwhile, as more $CHCl_3$ was added (for example, 20 µL $CHCl_3$) to $D_2O$, a new broader peak appeared at 7.20 ppm (Figure 3.3). This peak is assigned to $CHCl_3$ mixed with $D_2O$ as an emulsion. Every NMR-detected nucleus in a molecule has a specific chemical shift value, which depends on its chemical environment. Whether molecularly dissolved or emulsified, $CHCl_3$ has the same molecular structure, but their chemical environment is different, resulting in two peaks at different chemical shifts. While the narrow peak at 7.55 ppm results from $CHCl_3$ in a chemical environment of $D_2O$, the chemical shift of the emulsified $CHCl_3$ is closer to the chemical shift of pure $CHCl_3$. Accordingly, the chemical environment in the emulsion colloids is based more on $CHCl_3$ surrounded by other $CHCl_3$ molecules rather than by $D_2O$. The slight difference in chemical shift that the broader $CHCl_3$ peak in $D_2O$ exhibits compared to a pure $CHCl_3$ NMR sample is attributed to the fact that the emulsion colloids are still surrounded by a different chemical environment, i.e., the solvent $D_2O$. The integral of the peak for the molecularly dissolved $CHCl_3$ was found to be 0.1568 ± 0.001 at the point when the emulsion peak first appeared. The peak for the molecularly dissolved $CHCl_3$ remained constant when more $CHCl_3$ was added to the $CHCl_3/D_2O$ mixture, which indicates $CHCl_3$ is completely dissolved molecularly until the saturation limit is reached, and that an emulsion only appears after the saturation with molecular $CHCl_3$. The intensity of an NMR signal is proportional to the number of protons

contributing to the signal, which is why NMR spectroscopy is intrinsically quantitative. However, integrated signal intensities only give information about the relative number of different protons. Consistent with this statement, the ratio of the HOD peak to the saturated, molecularly dissolved $CHCl_3$ peak remains unchanged under the same experimental conditions.

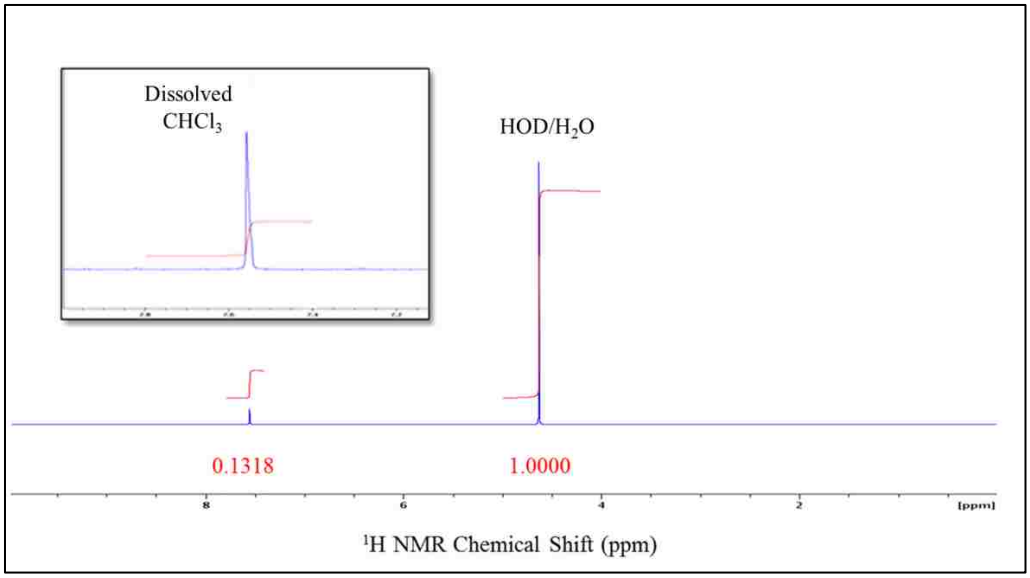


Figure 3.2. $^1H$ NMR spectrum of 3 µL in $D_2O$. The integration of dissolved $CHCl_3$ at 7.55 ppm was 0.1318 when the HOD peak at 4.63 ppm was set to 1.000.

The PWHGMs were filled with $CHCl_3$ according to the vacuum-based loading procedure (Section 2.3) and washed with $D_2O$ (Section 2.4). The washing process was necessary to remove excess amounts of $CHCl_3$ on the surfaces of the PWHGMs so that NMR spectra provide reasonable evidence of $CHCl_3$ inside of microspheres. After the loading and washing process, the $CHCl_3$-loaded PWHGMs were suspended in $D_2O$, and NMR spectra were recorded (Figure 3.4). A broad peak is observed at 7.20 ppm and assigned to the $CHCl_3$ inside PWHGMs. The $CHCl_3$ inside the microspheres had the

same chemical shift as the formerly recorded emulsified $CHCl_3$, indicating that they have same chemical environment [107]. The microspheres were fully filled with $CHCl_3$ and

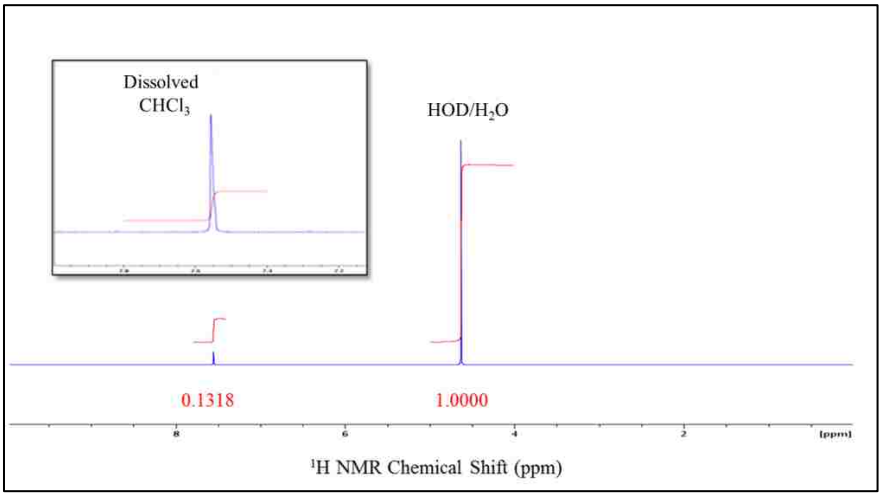


Figure 3.3. $^1H$ NMR spectrum of 20 µL chloroform in $D_2O$. The chemical shifts assignments are molecularly dissolved $CHCl_3$: 7.55 ppm, emulsified $CHCl_3$: 7.20 ppm, and HOD: 4.63 ppm.

the microspheres can be seen as providing a template for large colloids or droplets of $CHCl_3$, however not as a simple emulsion but surrounded by the glass shell of the microspheres. While the $CHCl_3$ in the microspheres exhibits the same chemical shift as observed for emulsified $CHCl_3$ (Figure 3.5), the integrated intensity of the narrow singlet peak at 7.55 ppm was found to be only 0.1149, which is lower than that expected for the peak intensity of the molecularly dissolved $CHCl_3$ in saturation (integral of 0.1568). Accordingly, the broad peak at 7.20 ppm (integral of 0.2174) cannot be from emulsified $CHCl_3$ in $D_2O$ but is attributed to $CHCl_3$ inside the PWHGMs. Additional evidence for this statement is provided by the spectrum of the supernatant, which after three times washing with $D_2O$ did not show any peak for emulsified $CHCl_3$ but only a small peak for the residual, molecularly dissolved $CHCl_3$ below the saturation limit.

**3.2.3. Conclusions.** In this model system, the behavior of $CHCl_3$ in $D_2O$ and in the cavities of hollow glass microspheres was evaluated. A model study of the binary immiscible system of $CHCl_3$ in $D_2O$ provided information with respect to two aspects (qualitative and quantitative information): (a) molecularly dissolved $CHCl_3$ has a different chemical environment than emulsified $CHCl_3$ and, thus, a different chemical shift is observed; (b) $CHCl_3$ first dissolves molecularly while emulsion colloids only form after saturation is reached for the molecular dissolution. The integrated signal intensities for the peak of the molecularly dissolved $CHCl_3$ correlate well with the known molecular dissolution limit for $CHCl_3$ in $D_2O$. The results demonstrated that NMR spectroscopy not only can provide structural information of the materials loaded in the microspheres, but is also capable of quantifying their amounts.

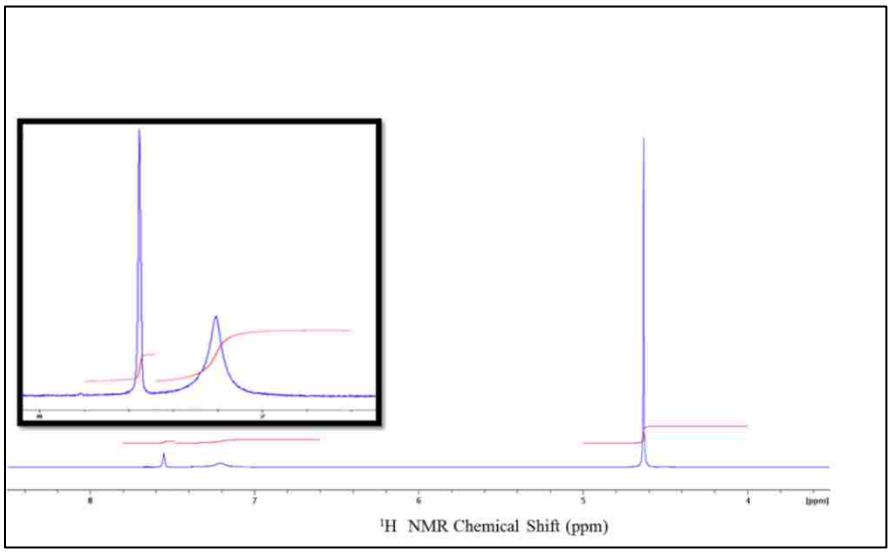


Figure 3.4. $^1H$ NMR spectrum of $CHCl_3$ inside of the microspheres suspended in $D_2O$. The peaks from left to right are assigned to dissolved $CHCl_3$ in $D_2O$ (7.55 ppm), $CHCl_3$ inside microspheres (7.20 ppm), and HOD (4.63 ppm).

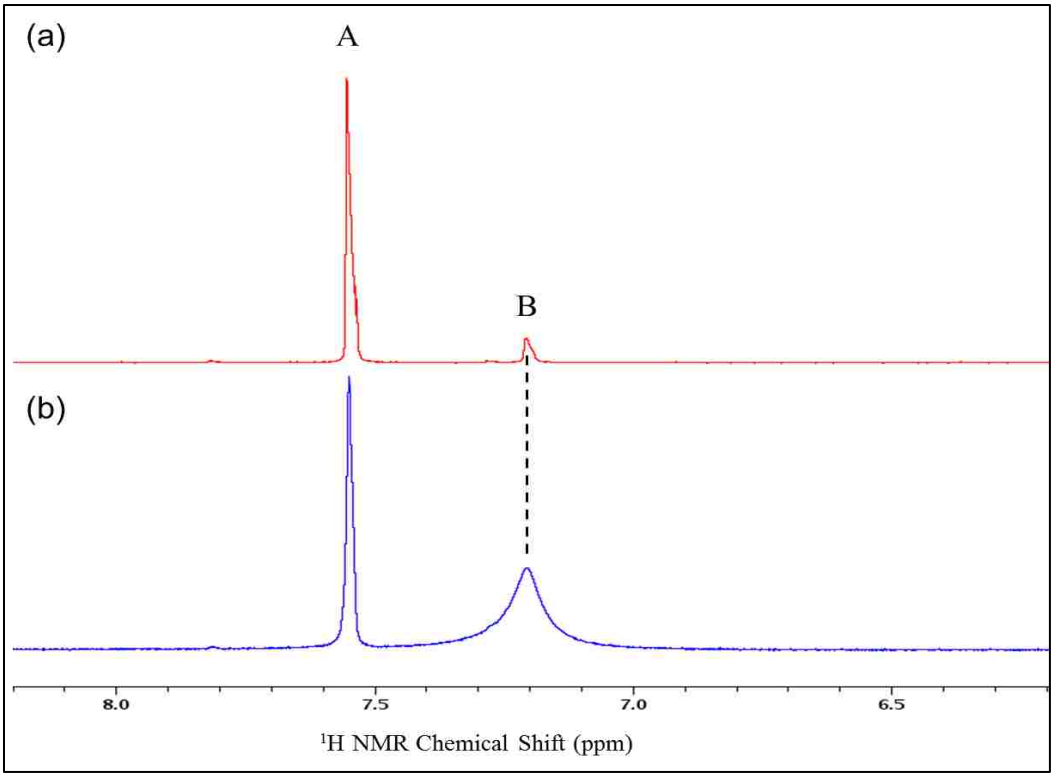


Figure 3.5. Comparisons between $^{1}H$ NMR spectra of (a) $CHCl_3$ emulsion peak in $D_2O$ and (b) peak of $CHCl_3$ in microspheres. Peak A is assigned to the dissolved $CHCl_3$ in $D_2O$. Peak B is assigned to the $CHCl_3$ emulsion in spectrum (a) and the $CHCl_3$ in the microspheres in spectrum (b).

## 3.3. BINARY IMMISCIBLE SYSTEM OF $C_{12}H_{26}$ AND $D_2O$

The binary immiscible system of $C_{12}H_{26}$ and $D_2O$ was conducted to simulate the real application of the microspheres as drug carriers. $C_{12}H_{26}$ is a water-non-soluble molecule, which is similar to some drugs.

**3.3.1. Experiments Design and Procedures.** The control experiments of two immiscible solvents were first carried out by adding a series of well-defined amounts of $C_{12}H_{26}$ (1 µL, 2 µL, 3 µL, 4 µL, 5 µL, 6 µL, 8 µL, 10 µL, 20 µL, 30 µL, 40 µL, 50 µL, 70 µL) to 750 µL $D_2O$ without microspheres present. A $^{1}H$-NMR spectrum was recorded for each of the mixtures. Thereafter, glass microspheres were loaded with $C_{12}H_{26}$

according to the vacuum-based loading system of section 2.3 and washed three times with $D_2O$ following the washing procedures of section 2.4. The microspheres were then re-suspended in $D_2O$ and the sample gently shaken before the analysis to ensure the microspheres were homogeneously distributed in the NMR active volume. An NMR spectrum of the suspended microspheres and their loaded material was recorded. The detailed experimental procedures were described in Section 2 (MATERIALS AND METHODS).

**3.3.2. Results and Discussion.** Before the analysis of $C_{12}H_{26}$ loaded into microspheres, control experiments were conducted to obtain general insights into the behavior of the virtually immiscible $C_{12}H_{26}$ in $D_2O$ system as observed by NMR. Figure 3.6 shows NMR spectra of 1 µL $C_{12}H_{26}$ in 750 µL $D_2O$ (Figure 3.6a) and 70 µL $C_{12}H_{26}$ in 750 µL $D_2O$ (Figure 3.6b). When 1 µL $C_{12}H_{26}$ was added to 750 µL $D_2O$, there were three sets of peaks observed in the spectrum. The singlet HOD peak at 4.63 ppm was from $^1H$ impurities in the lock solvent $D_2O$, which has a purity of 99.8% with 0.2% $H_2O$. The fast exchange between protons from $H_2O$ to $D_2O$ and vice versa leads to a statistical distribution of $^1H$ among the water molecules resulting almost exclusively in HOD molecules (and almost no $H_2O$ molecules) within the solution. The complex, asymmetrical peak pattern at 1.17 ppm is assigned to the $CH_2$ groups of $C_{12}H_{26}$ while the low-resolved triplet peak at 0.76 ppm is assigned to the $CH_3$ groups of $C_{12}H_{26}$. The triplet peak is caused by spin-spin coupling (J coupling) to the two protons of the $CH_2$ groups. The more complex, asymmetrical $CH_2$ signal cannot be interpreted as a singlet peak at 1.17 ppm but rather contains several multiplets from couplings between the $CH_2$ groups of $C_{12}H_{26}$ as well as the coupling of the $CH_2$ groups to the terminal $CH_3$ groups. When

1 µL $C_{12}H_{26}$ was added to 750 µL $D_2O$, the mass concentration of $C_{12}H_{26}$ in $D_2O$ was $1 \times 10^{-3}$ g/mL, which is much greater than the reported molecular solubility of $C_{12}H_{26}$ in water ($3.7 \times 10^{-9}$ g/mL at 25 °C [110]). Assuming that the solubilities in $H_2O$ and $D_2O$ are similar, the amount of molecularly dissolved $C_{12}H_{26}$ is below the detection limit of NMR spectroscopy ($1.8 \times 10^{-4}$ mol/L) and only emulsified colloids of $C_{12}H_{26}$ contribute to the broadened peaks observed in the spectrum. This phenomenon became more pronounced when more $C_{12}H_{26}$ was added into the $D_2O$ (e.g., 70 µL in 750 µL $D_2O$) as shown in Figure 3.6b. There are four NMR signals present in addition to the HOD/$H_2O$ peak at 4.63 ppm. The broad peaks next to the peaks assigned earlier to the $CH_2$ and $CH_3$ groups of $C_{12}H_{26}$ originate from the separate phase of $C_{12}H_{26}$ and its $CH_2$ and $CH_3$ groups. The phase separation of $C_{12}H_{26}$ in $D_2O$ changes the chemical environment of the $C_{12}H_{26}$ molecules and with it the chemical shifts in the NMR spectra. The control experiments provide many pieces of valuable information on this binary immiscible system that are used here for a model study. First, emulsified $C_{12}H_{26}$ was easily formed due to the low solubility of $C_{12}H_{26}$ in water, and the peaks from the emulsified $C_{12}H_{26}$ can easily be distinguished from the peaks of phase-separate $C_{12}H_{26}$. Second, the substantial broadening of the peaks is caused by a distribution of the colloidal drop sizes of the $C_{12}H_{26}$ emulsion. Every colloid size creates an NMR signal that has a slightly different chemical shift. Overall, the control experiments offer sufficient information to analyze and explain the NMR peaks recorded in the later investigation with microspheres loaded with $C_{12}H_{26}$ and suspended in $D_2O$.

In next investigation, glass microspheres were loaded with $C_{12}H_{26}$ according to the loading system described in Section 2.3 and washed three times with $D_2O$ to remove

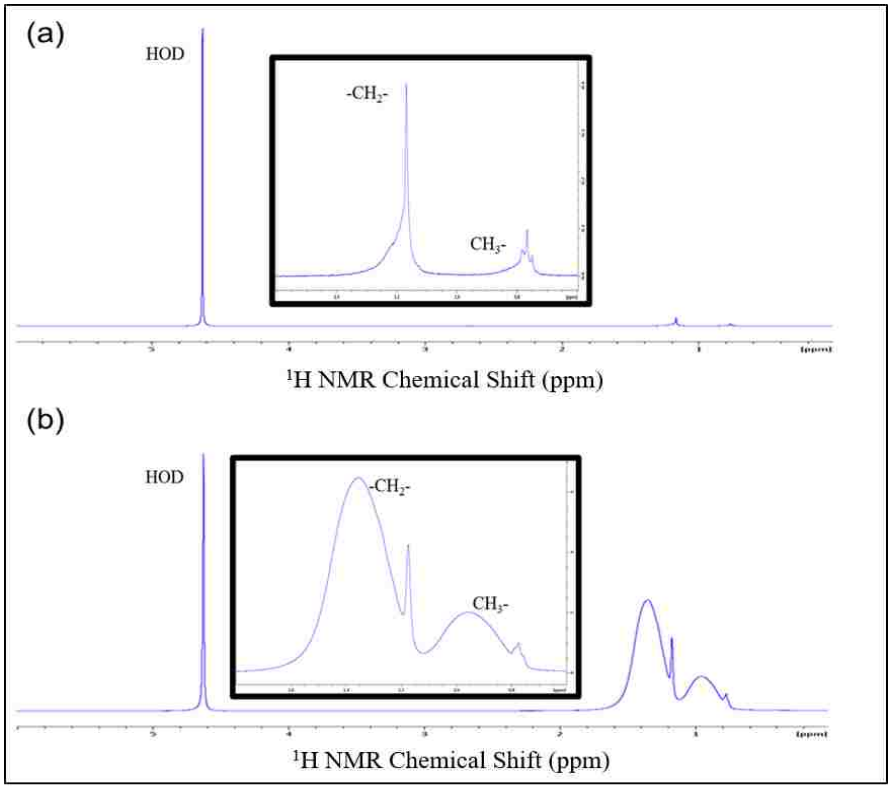


Figure 3.6. Control experiments of different amount of $C_{12}H_{26}$ added into $D_2O$. a) 1 µL $C_{12}H_{26}$ in $D_2O$. b) 70 µL $C_{12}H_{26}$ in $D_2O$.

excess amount of $C_{12}H_{26}$ from the outer wall of the microspheres according to the procedure described in Section 2.4. Afterwards, the microspheres were re-suspended in $D_2O$ and transferred into a 5 mm NMR tube. The recorded NMR spectrum is shown in Figure 3.7. There are three NMR peaks observed in the spectrum, (a) the HOD peak at 4.63 ppm, (b) the combined peak of all $CH_2$ groups at 1.19 ppm, and (c) the $CH_3$ group peak at 0.78 ppm. The triplet splitting of the $CH_3$ group peak is not resolved and the peak of the $CH_2$ groups becomes very broad. The broadened peak shapes observed when $C_{12}H_{26}$ is loaded in the microspheres can be caused by several factors, such as changes in the relaxation times of molecules inside or outside the microspheres (homogeneous line broadening) caused by paramagnetic impurities introduced with the microspheres.

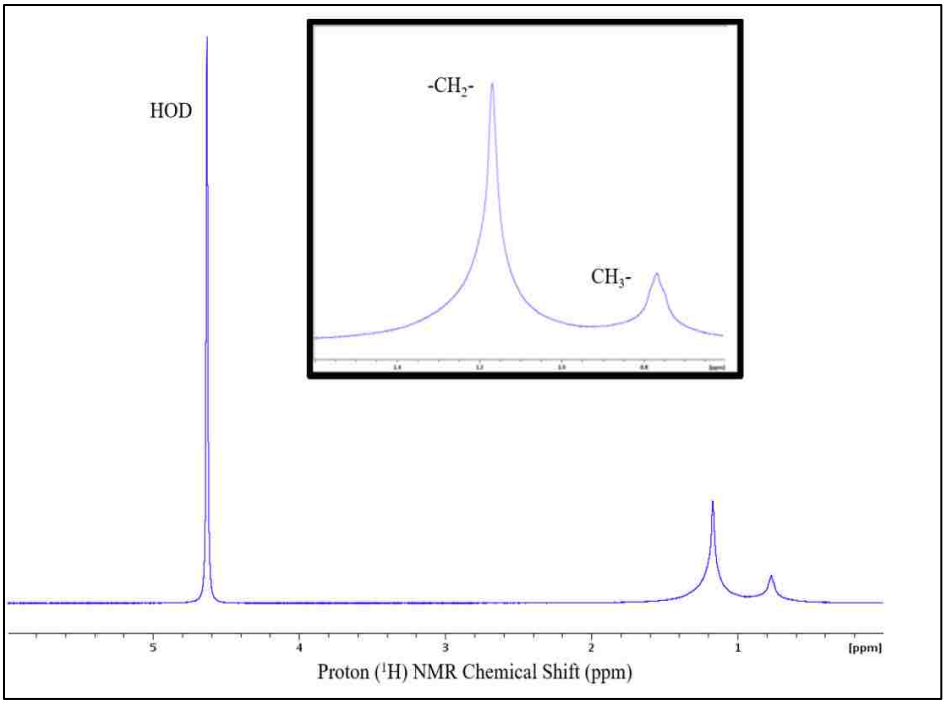


Figure 3.7. $^{1}$H NMR spectrum of microspheres loaded with $C_{12}H_{26}$ and suspended in $D_2O$. The chemical shift of the $CH_2$ groups was at 1.19 ppm and the $CH_3$ groups at 0.78 ppm.

The two common relaxation mechanisms for NMR-active nuclei, i.e., spin-lattice relaxation ($T_1$ time constant) and spin-spin relaxation ($T_2$ time constant), are both affected by paramagnetic impurities and will ultimately have an influence on the peak width, which is inversely proportional to the relaxation observed in the recorded free induction decay (FID). For most small molecules, the relaxation times $T_1$ and $T_2$ are about equal and long enough so that narrow lines are observed in the NMR spectra. The spin-lattice relaxation time $T_1$ of $C_{12}H_{26}$ was determined from a standard inversion-recovery experiment to be $T_1$ = 1.69 s [120], which should be long enough to generate narrow peaks. However, since broad peaks are still observed in the NMR spectra of the microspheres loaded with $C_{12}H_{26}$, another effect must be considered which can result in inhomogeneous peak broadening. Such effect is the distortion of the magnetic field

homogeneity by substantial susceptibility mismatches between materials. Magnetic susceptibility is a measure of the degree to which a material can be magnetized by an external magnetic field. As a result of this magnetization, magnetic field lines and with it the field's homogeneity is distorted. The distortion of the magnetic field leads inadvertently to peak broadening, which becomes especially visible at the bases of NMR peaks. As a result, the significant susceptibility mismatch that exists between the shell of the microspheres ($-16 \times 10^{-6}$ in SI units) on the one and $C_{12}H_{26}$ and $D_2O$ ($-9.06 \times 10^{-6}$ in SI units) on the other hand gives rise to the line broadening in the spectra of the loaded microspheres.

Other than the peak broadening, the chemical shifts of the $CH_2$ group peak and the $CH_3$ group peak are also changed. In the control experiments, four sets of peaks were noticed. As explained previously, the two narrow peaks were assigned to the emulsified $C_{12}H_{26}$ in $D_2O$ while the two broad peaks were generated by the phase-separate $C_{12}H_{26}$. The $CH_2$ and $CH_3$ group NMR signals from the $C_{12}H_{26}$ loaded in microspheres each occur with the closest chemical shifts to the emulsified $C_{12}H_{26}$ signals of the control experiments. $C_{12}H_{26}$ in the microspheres is the template for large colloid, and thus it has the same chemical environment with the emulsified $C_{12}H_{26}$, leading to the same chemical shift. This is consistent with the system of $CHCl_3$ and $D_2O$. When the $C_{12}H_{26}$ molecules confined in the microspheres, there is no phase separation, and therefore, the NMR signals that have the same chemical shift with the emulsified $C_{12}H_{26}$ must from inside of the microspheres.

**3.3.3. Conclusion.** In this model system, the NMR spectra of $C_{12}H_{26}$ in $D_2O$ and in the cavities of hollow glass microspheres were evaluated. The control experiments

demonstrate that emulsified $C_{12}H_{26}$ and phase-separate $C_{12}H_{26}$ in $D_2O$, which leads to two different sets of NMR signals with different line shapes and chemical shifts. The NMR signals from $C_{12}H_{26}$ inside of microspheres lead to peaks with broad bases and same chemical shifts with emulsified $C_{12}H_{26}$. The broad lines are explained by significant differences in the magnetic susceptibilities of the glass microspheres on the one and the $C_{12}H_{26}$ and $D_2O$ solutions on the other hand. The results show that NMR signals can be obtained from the loaded $C_{12}H_{26}$ inside the microspheres.

## 3.4. MATERIAL EXCHANGE FROM THE INTERIOR OF THE MICROSPHERES TO THE OUTSIDE

**3.4.1. Inspiration of the Investigation**. In the previous section, NMR spectroscopy was shown to be powerful to determine materials loaded inside of hollow glass microspheres. In the cases described above, materials remain about static in the microsphere without a significant exchange from the inside to the outside of the microspheres because the chemicals inside and outside were only very slightly miscible. Therefore, it is hard for individual molecules to overcome the phase barrier that the two individual liquids create through their interphase at the pores of the microspheres. In practice, however, drug and biomarker delivery requires the release of the drug or biomarker molecules to a target site, which is a dynamic process. Therefore, dynamic (or kinetic) NMR information is needed for a comprehensive characterization and evaluation of the microspheres as carriers in drug or biomarker delivery systems.

In the present study, reaction-based methodology was used to investigate the exchange of chemicals from the inside of the microspheres to the surrounding solution and vice versa. The general idea is to conduct a chemical reaction with one chemical

loaded inside the microspheres, while the other reactant is present only in the surrounding solution. The formation of a product will lead to the new peaks in the NMR spectra, which indicates a contact between the reaction components. The initiation of a reaction can only occur if the two chemicals are in close contact within the same medium, which requires an exchange of the chemicals inside and outside of the microspheres. A typical organic reaction was selected as the model system for studying the exchange of materials for several major reasons: (a) inorganic reaction in aqueous solution (such as acid-base reactions) are typically very fast and thus don't provide enough time to monitor the occurrence of the exchange on an NMR timescale; (b) $^{1}H$ NMR requires the presence of hydrogen atoms, which are more common in organic compounds; and (c) hydrogen atoms in inorganic compounds are often in fast exchange with the $H_2O$ solvent molecules, thus providing no specific peaks in the NMR spectra. In addition, acids can propagate from the inside of a microsphere to the outside or vice versa through breaking and reforming chemical bonds between hydrogen and oxygen in the aqueous solution without requiring physical movement of hydrogen atoms. Therefore, it is difficult to determine the occurrence of physical exchange from inside to outside by the observation of acid-base reactions (i.e., neutralization reactions). Another reason for choosing organic reactions is that most drugs and biomarkers are organic molecules, so that an organic molecule based model system is more similar to the projected future applications. In the present study, the esterification of isopropanol and acetic acid and its reverse reaction (i.e., the hydrolysis of isopropyl acetate) was used as the model system to study the exchange of materials.

**3.4.2. Experiments Design and Procedures**. The esterification of isopropanol with acetic acid reaction (Figure 3.8) was first carried out as a control experiment without the microspheres involved. Similarly the hydrolysis reaction of isopropyl acetate was conducted in a control experiment. Before conducting the reaction, NMR spectra of acetic acid and isopropanol were recorded individually to obtain the chemical shifts of each type of proton (Table 1). The esterification was then carried out by mixing 0.1026 g of acetic acid (molar mass 60.05 g/mol) and 0.1035 g of isopropanol (molar mass 60.1 g/mol) in a glass vial. The masses of acid and alcohol compounds were chosen so that the mole ratio is 1:1. 100 µL of the mixture were transferred to an NMR tube containing 750 µL $D_2O$ and 5 µL of concentrated $H_2SO_4$ as a catalyst. An NMR spectrum was recorded immediately after the initiation of the reaction and every two hours after the initiation. The last NMR spectrum was recorded after 24 hours.

The control experiment of the hydrolysis of the esterification of isopropanol with acetic acid reaction (Figure 3.8) was carried out by adding 20 µL of isopropyl acetate into 750 µL $D_2O$ in the absence of concentrated $H_2SO_4$. After a first NMR spectrum was recorded, 5 µL of concentrated $H_2SO_4$ was added into the solution, and another NMR spectrum was immediately recorded. Further NMR spectra were recorded after 10 minutes and after 120 minutes of reaction time.

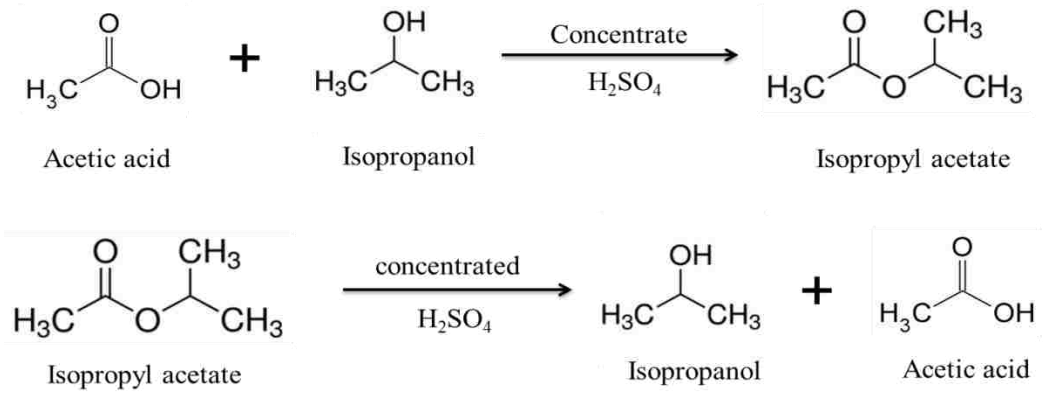


Figure 3.8. The esterification of isopropanol with acetic acid and its hydrolysis reactions.

Finally, microspheres were loaded with isopropyl acetate according to the vacuum-based loading protocol and the washing procedures described in Sections 2.3 and 2.4. The microspheres loaded with isopropyl acetate were transferred into an NMR tube and a spectrum was recorded in the absence of concentrated $H_2SO_4$. Then 5 µL of concentrated $H_2SO_4$ was pipetted into the NMR tube and another NMR spectrum recorded after 5 minutes. Again, after 10 minutes, a third NMR spectrum was recorded.

**3.4.3. Results and Discussion**. The esterification reaction is a simple organic reaction where a carboxylic acid is heated with an alcohol in the presence of a strong mineral acid as the catalyst. It usually takes hours to complete the reaction and therefore, enough time is provided to monitor the reaction in an NMR spectrometer. Acetic acid and isopropanol were selected as the reactants because the chemical-shift difference of the CH group between isopropanol and isopropyl acetate is about 1 ppm and thus is easily detectable. The high resolution of the two peaks can be used to evaluate the reaction progress, which in this case serves as an indicator of the chemical exchange from inside the microspheres to the outside. The control experiments of esterification were first

carried out by mixing acetic acid and isopropanol at a mole ratio of 1:1 and observing the corresponding NMR spectra. The enlarged peak areas are shown in Figure 3.9. Acetic acid has a singlet peak at 1.84 ppm, while isopropanol exhibits a septet at 3.76 ppm and a doublet at 0.92 ppm. Isopropyl acetate, which is the product of the reaction, shows a septet at 4.72 ppm, a singlet at 1.81 ppm, and a doublet at 0.99 ppm.

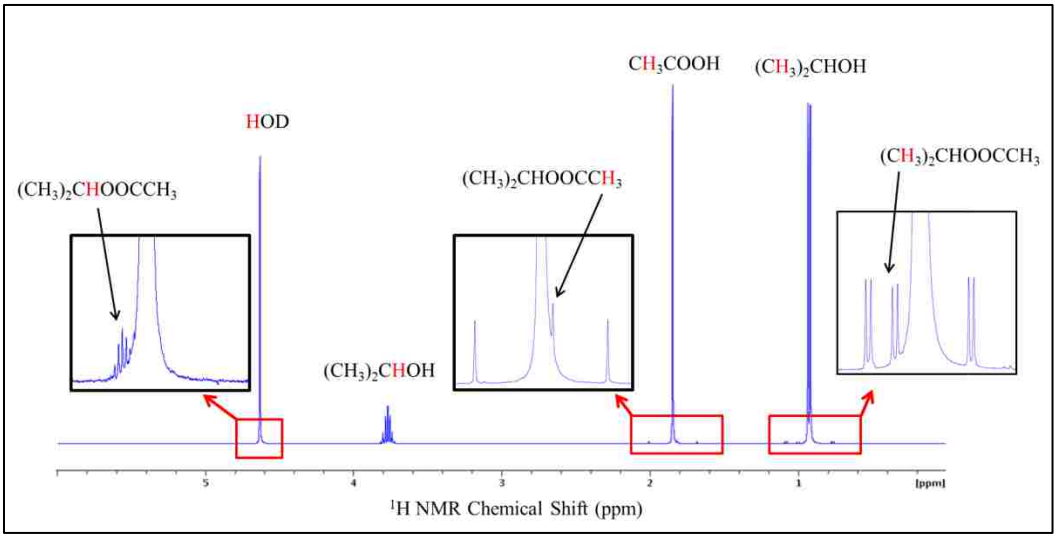


Figure 3.9. $^{1}H$ NMR spectrum recorded during the esterification of isopropanol with acetic acid after adding 5 µL concentrated $H_2SO_4$.

The results (Figure 3.9) indicate that the esterification reaction started immediately after 5 µL of concentrated $H_2SO_4$ were added, because the peaks of isopropyl acetate were already observed less than a minute after the reaction was initiated. The septet peak of isopropyl acetate (4.72 ppm) is close to the HOD peak, while the singlet peak of the $CH_3$ group in isopropyl acetate (1.81 ppm) and the doublet peak of the $CH_3$ group in isopropyl acetate (0.99 ppm) are next to the singlet peak of the $CH_3$ group in acetic acid and the doublet peak of the $CH_3$ group in isopropanol, respectively. However, the septet peak of the isopropyl CH group has a chemical shift difference of 1

ppm from the septet peak of the isopropanol CH group. The resolution of these two peaks can be used as indication for the progress of the esterification, and therefore, the occurrence of the two septet peaks is sufficient to show an exchange between the inside of the microspheres with the surrounding solution. More NMR spectra were recorded to understand the reaction progress, where the NMR spectrum recorded after 24 hours is shown in Figure 3.10. However, no significant difference in the peak intensities is observed after 24 hours. Esterification reactions typically require temperatures between 60 – 110 °C, while the reaction rate is very slow at lower temperature. Alternatively, the reaction may reach equilibrium very soon after the initiation of the reaction, so that it may already be complete after a few minutes.

Because two chemicals are required to initiate the reaction (isopropanol and acetic acid in this case), a problem encountered in this study was which chemical should be loaded into microspheres and which into the surrounding solution. The second problem occurred around the washing procedure, because acetic acid and isopropanol are soluble in both water and chloroform, and it is hard to find an immiscible solvent to wash the microspheres loaded with acetic acid or isopropanol. Therefore, the esterification of acetic acid with isopropanol was not pursued further in the evaluation of the properties of microspheres.

In contrast, the hydrolysis of esters only requires one reactant (i.e. the ester) and the reaction occurs at the same condition as the esterification formation. In addition, isopropyl acetate has only a moderate solubility in water, which makes it possible to remove excess amounts of loaded chemicals from the microspheres. Moreover, in the esterification reaction, the focus was on the formation of isopropyl acetate, from which

the septet peak of the CH group was nearly covered by the HOD peak. Peak overlapping in NMR spectra makes it difficult to quantify the number of protons of each peak without advanced signal deconvolution software and thus results in inaccurate interpretation and quantification. In the hydrolysis reaction, however, the focus was on the formation of acetic acid and isopropanol, where the latter exhibits a septet peak of the CH group that is not only well separated from the septet peak of the CH group of the isopropyl acetate but also from the singlet peak of HOD. Therefore, in the results and discussion section, a greater focus is put on the septet peak of the isopropanol CH group.

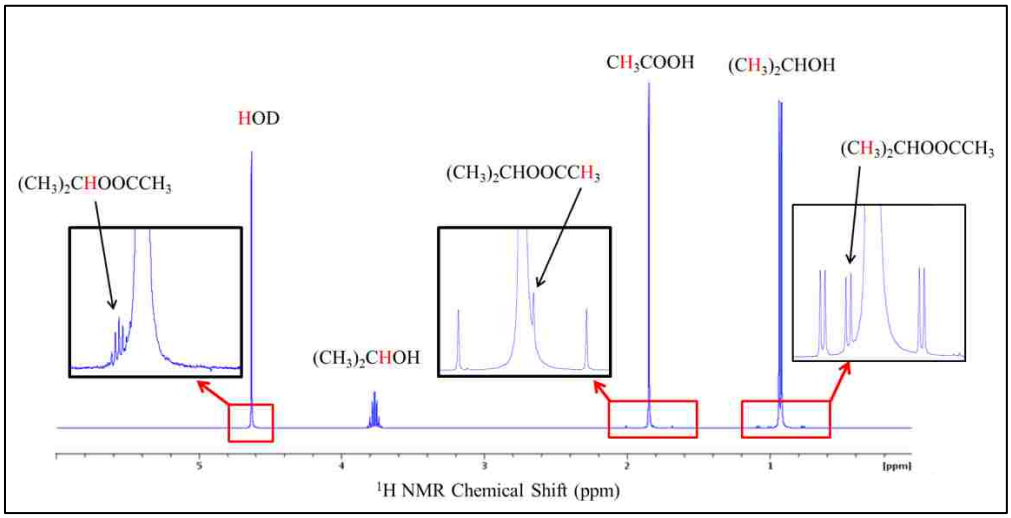


Figure 3.10. $^{1}$H NMR spectrum of the esterification of isopropanol with acetic acid after 24 hours.

The hydrolysis of the isopropyl acetate was evaluated with NMR spectroscopy. The first NMR spectrum was recorded as a control experiment with 20 µL of isopropyl acetate in 750 µL $D_2O$ in the absence of concentrated $H_2SO_4$ (Figure 3.11). The septet peak of the CH group of isopropyl acetate appears at 4.85 ppm next to the singlet peak of HOD (4.63 ppm). Another two sets of peaks were observed at higher field. The singlet

peak at 1.93 ppm is assigned to the two isopropyl $CH_3$ groups of the ester, and the doublet peak at 1.10 ppm to the acetate $CH_3$ group of the ester. There was only baseline noise observed around 3.78 ppm, indicating that no isopropanol has yet been formed. Afterwards, the reaction was initiated by adding 5 μL of concentrated $H_2SO_4$. Figure 3.12 shows the NMR spectrum recorded less than a minute after the reaction was initiated. A septet peak is observed at 3.78 ppm and assigned to the CH group of newly formed isopropanol. This particular peak indicates that the hydrolysis reaction has immediately started in the presence of concentrated $H_2SO_4$. NMR spectra recorded at the reaction times of 10 and 120 minutes (Figure 3.13) reveal that the intensity of the peak continuously increases with the reaction proceeding, leading to a higher S/N ratio. This indicates the equilibrium for the hydrolysis reaction was not reached even after 120 minutes. The hydrolysis of the isopropyl acetate proved to be more suitable to evaluate the exchange of materials inside and outside of the microspheres. First, isopropyl acetate is the only chemical that needs to be loaded into the microspheres thus providing a simpler experimental design. Second, the washing procedure can still be applied because isopropyl acetate has only a moderate solubility in water. Ultimately and most importantly, the NMR spectra are easier to interpret, and the increase in the intensity of the isopropanol CH-group septet peak is an indication of the reaction progress. Therefore, both the presence and increase of the isopropanol septet peak can be used as evidence for chemical exchange between the inside of the microspheres with the surrounding solution.

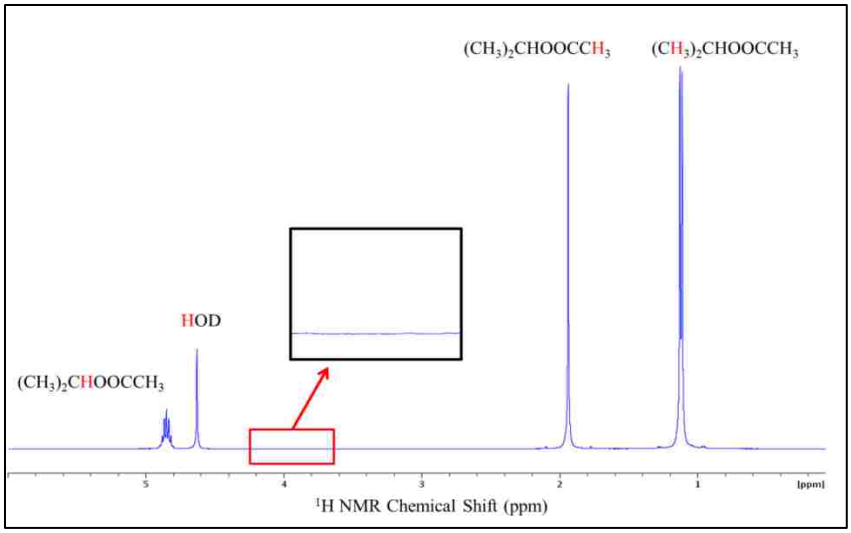


Figure 3.11. $^{1}H$ NMR spectrum of the hydrolysis of isopropyl acetate before the injection of concentrated $H_2SO_4$.

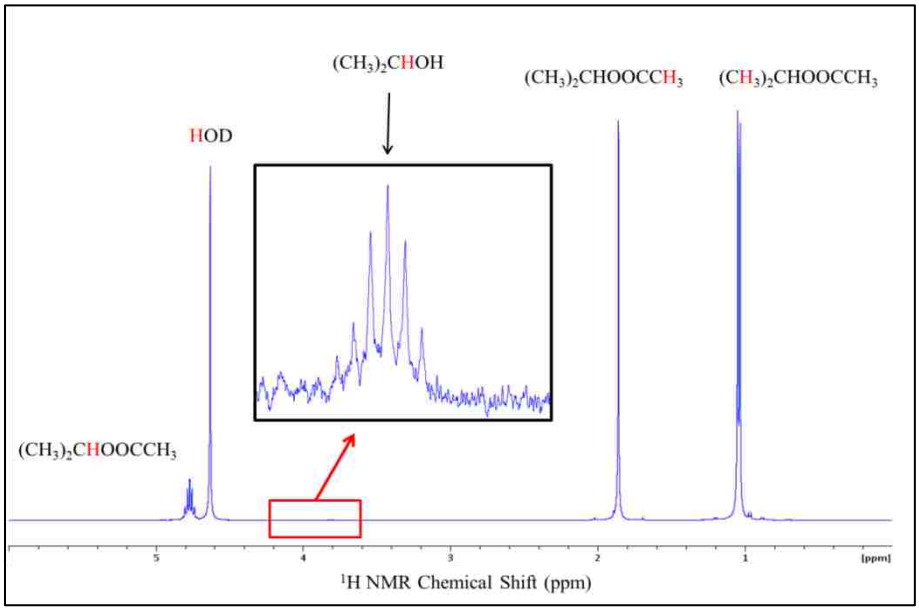


Figure 3.12. $^{1}H$ NMR spectrum of the hydrolysis of isopropyl acetate after the injection of 5 µL concentrated $H_2SO_4$.

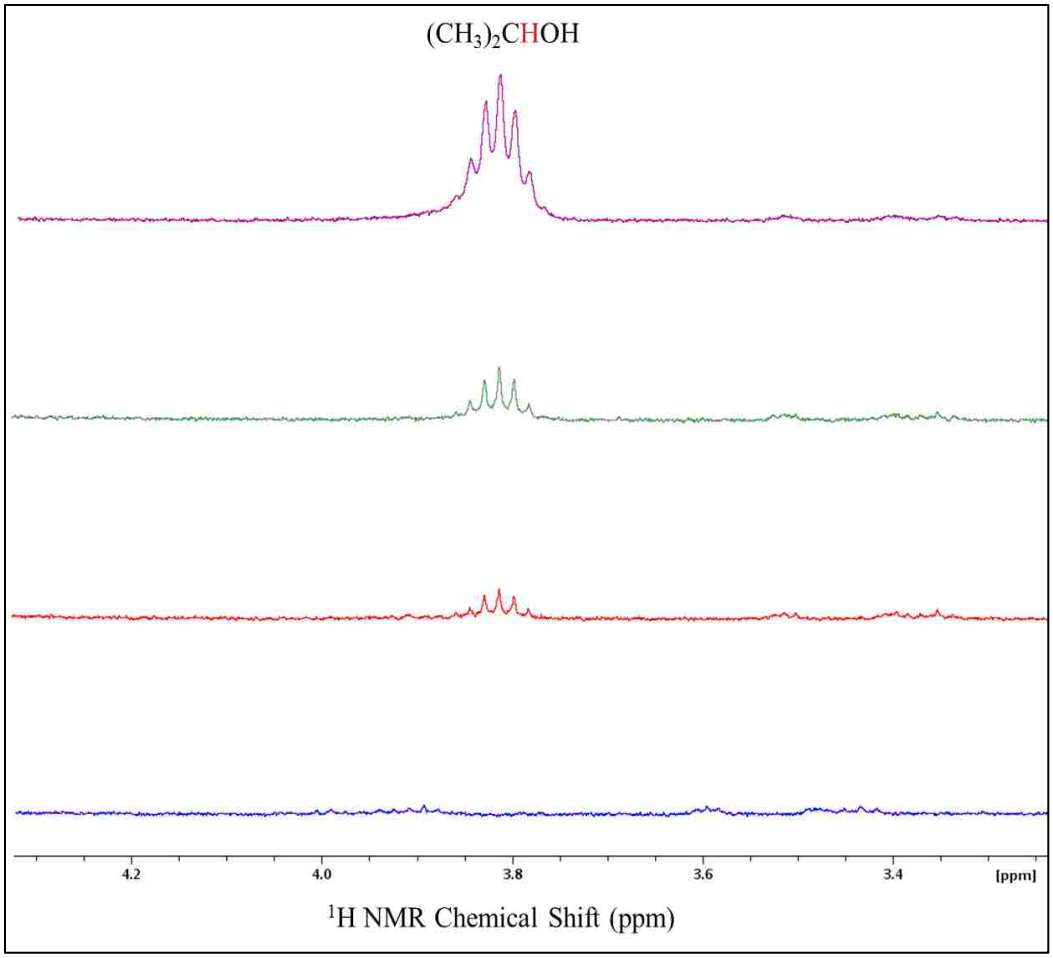


Figure 3.13. $^{1}$H NMR spectra of the formation of isopropanol in the hydrolysis of isopropyl acetate. The spectrum from bottom up was recorded before the addition of concentrated sulfuric acid, directly after the addition of acid, 10 minutes after the addition of acid, and 120 minutes after the addition of acid.

In a second series of experiments microspheres were loaded with isopropyl acetate and washed with $D_2O$. Due to the moderate solubility of isopropyl acetate in water, the volume of isopropyl acetate injected during the loading process through the rubber hose was kept at a minimum and did not completely fill all microspheres. The washing of the microspheres was only conducted once to preserve the material inside the microspheres, and the supernatant was investigated with NMR spectroscopy. Only very

small amounts of the isopropyl acetate were present in the supernatant, indicating that most of the ester was absorbed into the cavities of the microspheres.

An NMR spectrum was recorded after the microspheres were suspended in 750 µL of $D_2O$ but in the absence of concentrated $H_2SO_4$ (Figure 3.14). No peaks were observed at 3.80 ppm, indicating that the hydrolysis had not yet started. A broad peak of the CH group of isopropyl acetate was observed at 4.78 ppm, with the resolution of the septet peak lost. The doublet of the isopropyl $CH_3$ groups was also not resolved. The low resolution is due to the magnetic field distortions caused by the susceptibility differences between the shells of the microspheres and isopropyl acetate. Afterwards, 5 µL of concentrated $H_2SO_4$ was added into the solution and an NMR spectrum recorded within a minute after the addition of $H_2SO_4$. Figure 3.15 shows the results of the microspheres loaded with isopropyl acetate and suspended in $D_2O$ in the presence of the concentrated $H_2SO_4$. A broad peak observed at 3.81 ppm is assigned to the isopropanol CH group, which demonstrates the formation of isopropanol. However, the septet resolution of the peak is also lost, which indicates that the isopropanol is preferentially formed inside the microspheres. Isopropanol formed outside of the microsphere should exhibit a well resolved septet. The formation of isopropanol inside the microspheres indicates that $H^+$ propagated into the microspheres and initiated the reaction inside. Nevertheless, an NMR spectrum (Figure 3.16) recorded after 10 minutes of adding concentrated $H_2SO_4$ shows a higher resolution of the CH group peak at 4.78 ppm as well as the $CH_3$ group peak at 3.81 ppm indicating the presence of isopropyl acetate and isopropanol outside the microspheres. Another indication that material exchanged between the cavities of the microspheres is that most of the microspheres slowly floated to the top of the solution

because of the lower density of isopropyl acetate (0.87 g/mL) inside the microspheres compared with the $D_2O$ in the surrounding solution. By floating to the top, the microspheres actually left the NMR-sensitive volume whereas the signals of the isopropanol and the isopropyl acetate could still be observed in the NMR spectra. Hence the observed signals must be from isopropyl acetate and isopropanol in $D_2O$. The increasing peak intensity of the isopropanol CH group indicated that the reaction was still proceeding and material was still leaching out of the microspheres. This demonstrated that a significant exchange of $H^+$ and isopropyl acetate occurred between the inside of the microspheres and the surrounding solution.

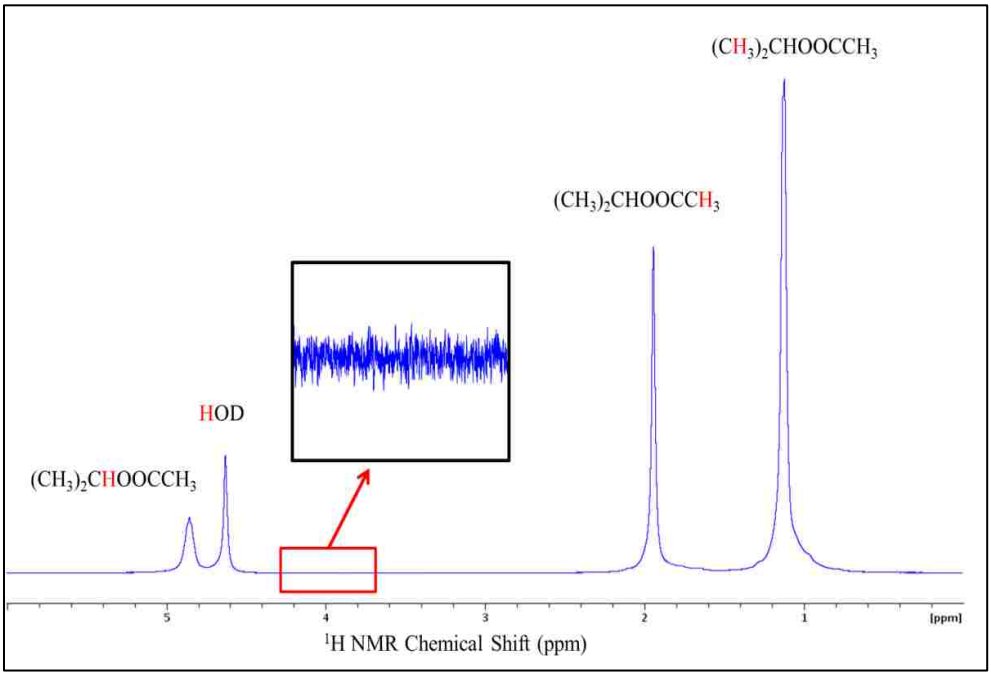


Figure 3.14. $^1H$ NMR spectrum of microspheres loaded with isopropyl acetate and suspended in $D_2O$ in the absence of concentrated $H_2SO_4$.

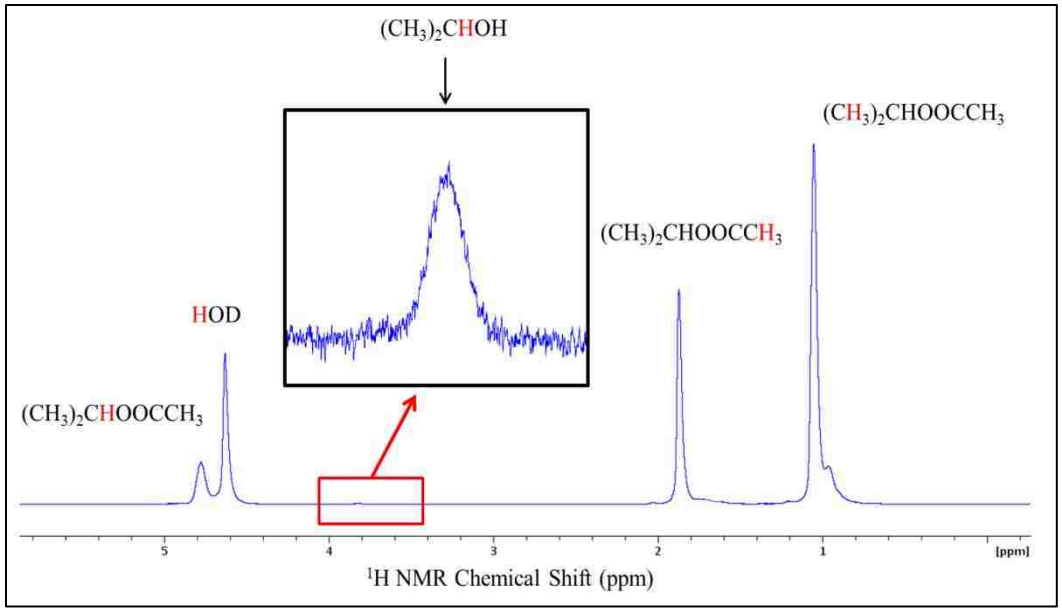


Figure 3.15. $^{1}H$ NMR spectrum of microspheres loaded with isopropyl acetate and suspended in $D_2O$ with 5 µL concentrated $H_2SO_4$ added.

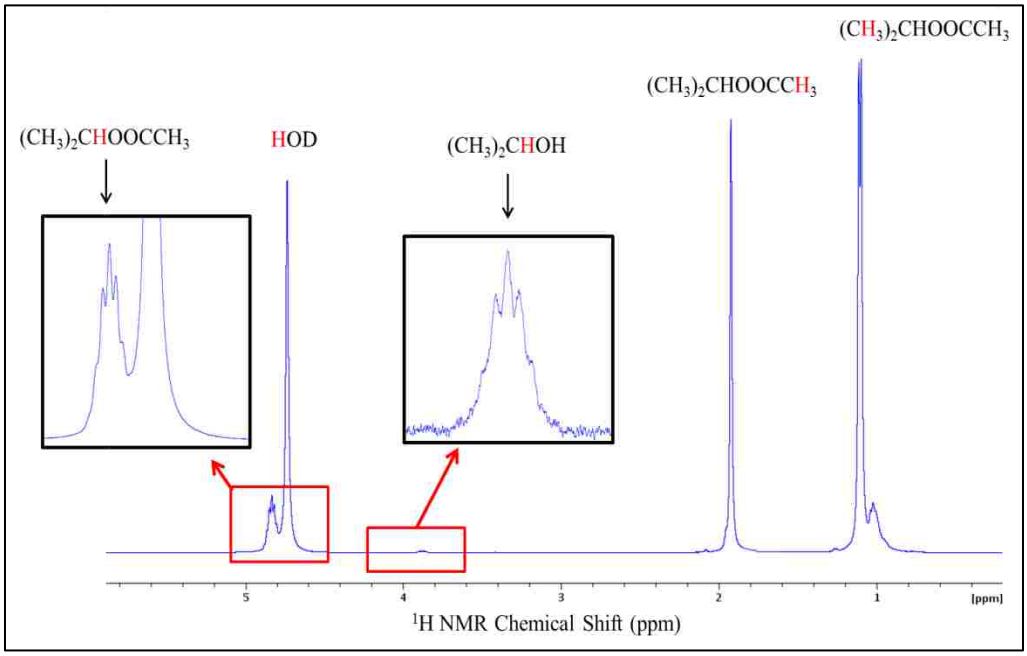


Figure 3.16. $^{1}H$ NMR spectrum of microspheres loaded with isopropyl acetate and suspended in $D_2O$ with 5 µL concentrated $H_2SO_4$ added. The spectrum was recorded after 10 minutes reaction time.

**3.4.4. Conclusion**. Model studies were conducted with the esterification reaction of isopropanol and acetic acid and its reverse reaction of isopropyl acetate hydrolysis into isopropanol and acetic acid. A series of control experiments demonstrated that the hydrolysis is a more suited reaction for the study of material exchange from the inside of the microspheres with the surrounding solution. The formation of isopropanol and the presence of a well-resolved septet peak for the CH group of isopropanol showed the progress of the reaction. NMR spectroscopy was also able to monitor the proceeding of the reaction after the initial injection of the concentrated $H_2SO_4$ catalyst. The improving resolution of the isopropanol CH-group septet peak along with the progress of the reaction indicated that not only $H^+$ propagated into the microspheres, but also that isopropyl acetate and the product of the hydrolysis leached out of the microspheres.

# 4. RELEASE KINETICS OF MATERIALS

## 4.1. MOTIVATION OF RELEASE KINECTICS STUDIES

One of the most important aspects during targeted drug or biomarker delivery is the controlled release of chemicals at a target site for therapeutic treatments. The chemicals should be delivered at a specific rate that is determined by the specific needs of the human body or the therapy over a defined period of time. By controlling the release of chemicals, it is desirable to maintain the concentration at a constant and lowest possible therapeutic level at the target site to achieve a successful treatment without causing toxic side effects. There are many types of controlled drug release systems, such as encapsulation dissolution controlled systems [121], matrix dissolution controlled systems [122], water penetration controlled systems [123], chemically controlled systems [124], and others [125-127]. In general, it can be divided into two major categories, degradation-controlled system and diffusion-controlled system (Figure 4.1 [128]).

The degradation-controlled systems function by the release of drugs from a bulk phase, in which the drugs are homogeneously dispersed. The drugs are released when the matrix is deformed or decomposed. The change to the bulk phase can principally be separated into two classes: bulk erosion and surface erosion [128, 129]. Bulk erosion refers to a uniform deformation or degradation throughout the bulk of the materials, whereas the degradation starts at the matrix surface in the case of surface erosion, and the size of the carrier is slowly and uniformly reduced inward. The dissolution rate determines the release process of degradation and is highly depended on the degrading material and the medium in which it degrades. The most commonly used materials in

degradation-controlled system are biodegradable polymers [130]. The first generation of biodegradable structures includes polyesters, poly(glycolic acid) (PGA), poly(D,L-lactic acid) (PLA), and poly(D,L-lactic-coglycolic acid) (PLGA) [131]. Biodegradable polymers have very prominent applications in targeted drug delivery because of their biocompatibilities. They can decompose into natural byproducts, such as water and carbon dioxide, and thus are easily removed from target sites after they delivered their therapeutic payload [132]. Meanwhile, the properties of polymers have major effects on the dissolution rate and release behaviors of drug molecules. These parameters include crystallinity [133], glass transition temperature [134], hydrophilicity and hydrophobicity [135], and molecular weight [136]. Optimization of these properties can largely improve the functionality of the polymers as vehicles for drug release.

The other drug release systems are diffusion controlled, where physical and chemical phenomena affect the release rate. The drug molecules must travel through tortuous pathways to exit the matrix and diffuse into the surrounding solution. Typical diffusion-based drug delivery systems include matrix-based or reservoir-based (Figure 4.1). In matrix-based diffusion system, drugs are incorporated into polymers, where the swelling effects of the polymers lead to a volume expansion of the system. The expansion will cause the opening of pores through which the drug is released. Porous poly (lactic-co-glycolic acid) (PLGA)-based microparticles are the most common polymers used for matrix-based controlled drug delivery system [132]. The sizes of the open pores of the polymer become larger and eventually exceed the size of the drug molecules. On the contrary, a reservoir-based diffusion system confines the drug molecules to a reservoir that has a static barrier towards the surrounding environment

[137]. Hence, the PWHGMs used in this study are considered a reservoir-based system. The materials to be delivered to a target site are first deposited and confined in the microspheres, and then suspended in a miscible solvent environment. The confined molecules can pass through the static pores in the walls of microspheres into the surrounding environment. Because of its quantitative capabilities, NMR spectroscopy provides an opportunity to monitor the release into the surrounding environment by observing time-dependent changes in the signal intensities of the released molecules.

## 4.2. EXPERIMENT DESIGN AND PROCEDURES

To observe the release of molecules from PWHGMs to a surrounding environment, the procedure exemplified below was developed. It utilizes the unrestricted diffusivity and unlimited miscibility of $H_2O$ in deuterated water ($D_2O$) but exploits the fact that deuterium atoms ($^2H$ atoms) are invisible in $^1H$ NMR spectroscopy. At the same time, the $D_2O$ can be used for shimming (i.e., homogenizing) the magnetic field and as NMR lock solvent. The procedure is as follows:

1. PWHGMs were loaded with $H_2O$ according to the vacuum-based loading system described in Section 2.3.
2. The loaded microspheres were washed three times with $CHCl_3$ according to the procedure described in Section 2.4.
3. A flame-sealed 1-mm capillary tube filled with $CHCl_3$ was inserted vertically along the long axis of a 5-mm NMR tube. The integrated singlet signal of $CHCl_3$ at 7.24 ppm from the capillary tube served as quantitative calibration

standard for the integrated peak intensity of the varying $H_2O$ peak at 4.63 ppm observed in this study.

4. The microspheres were carefully transferred into the bottom of the NMR tube such that the sample height stayed just below the NMR active volume of the tube.
5. $D_2O$ was slowly and carefully added into the NMR tube to avoid floating the microspheres.
6. A series of NMR spectra was recorded in regular intervals for up to 8 hours resulting in a total of up to 185 NMR spectra.
7. The time-dependent, integrated signal intensity of the $H_2O$ peak at 4.63 ppm was used to quantify the release of material from the microspheres.

The flame-sealed 1-mm capillary tube filled with $CHCl_3$ provided a time-independent chemical-shift and signal-intensity calibration for the experiments. The time-dependent signal intensities of the $H_2O$ peak at 4.63 ppm were measured in relation to the $CHCl_3$ calibration standard. The microspheres were kept below the NMR-active volume so that an increase in the $H_2O$ signal intensity is directly attributed to $H_2O$ molecules released from the microspheres.

## 4.3. RESULTS AND DISCUSSION

NMR is an intrinsically quantitative technique that can be employed for a wide variety of applications, among which are *in situ* monitoring of chemical reactions and their kinetics. One of the key advantages of $^1H$ NMR spectroscopy over other quantitative techniques is that the integrated signal intensity is directly proportional to the number of

protons in the NMR-active volume of the sample. Quantitative in situ NMR spectroscopy has therefore gained much popularity and attention in the last decades. The quantitative aspect of $^{1}H$ NMR spectroscopy was particularly utilized in this study to investigate the release kinetics of $H_2O$ molecules from the PHWGMs into surrounding $D_2O$.

The sample height of the microspheres was intentionally kept below the NMR-active volume as shown in Figure 4.2. The NMR-active volume is the volume where the radiofrequency (RF) field of the NMR pulses is delivered to the sample. It is identical with the volume in which the RF coil detects the NMR response from the sample. The only two chemicals used in this release study are $H_2O$ and $D_2O$. However, the $D_2O$ that is used as the surrounding solution has an intrinsic $H_2O$ impurity of about 0.2%. In addition, the fast exchange between hydrogen and deuterium in aqueous $H_2O/D_2O$ solutions leads to the formation of mostly HOD molecules. Both species, $H_2O$ and HOD, provide a singlet peak at 4.63 ppm (Figure 4.3). Therefore, if the microspheres loaded with $H_2O$ and suspended in $D_2O$ were placed within the NMR active volume, it would be impossible to differentiate between $H_2O$ inside or outside the microspheres. However, because the microspheres were placed below the NMR-active volume, only $H_2O$ released from the microspheres and diffused into the NMR-active volume will increase the $HOD/H_2O$ signal recorded by the NMR spectrometer.

Figure 4.3 shows an example of an NMR spectrum recorded during the release study using the sample setup illustrated in Figure 4.2. The singlet peak at 7.24 ppm is assigned to the $CHCl_3$ confined in the flame-sealed 1-mm central capillary. This signal serves as external standard and remains constant during the entire series of NMR experiments. The singlet peak at 4.63 ppm is assigned to HOD. This signal changes in

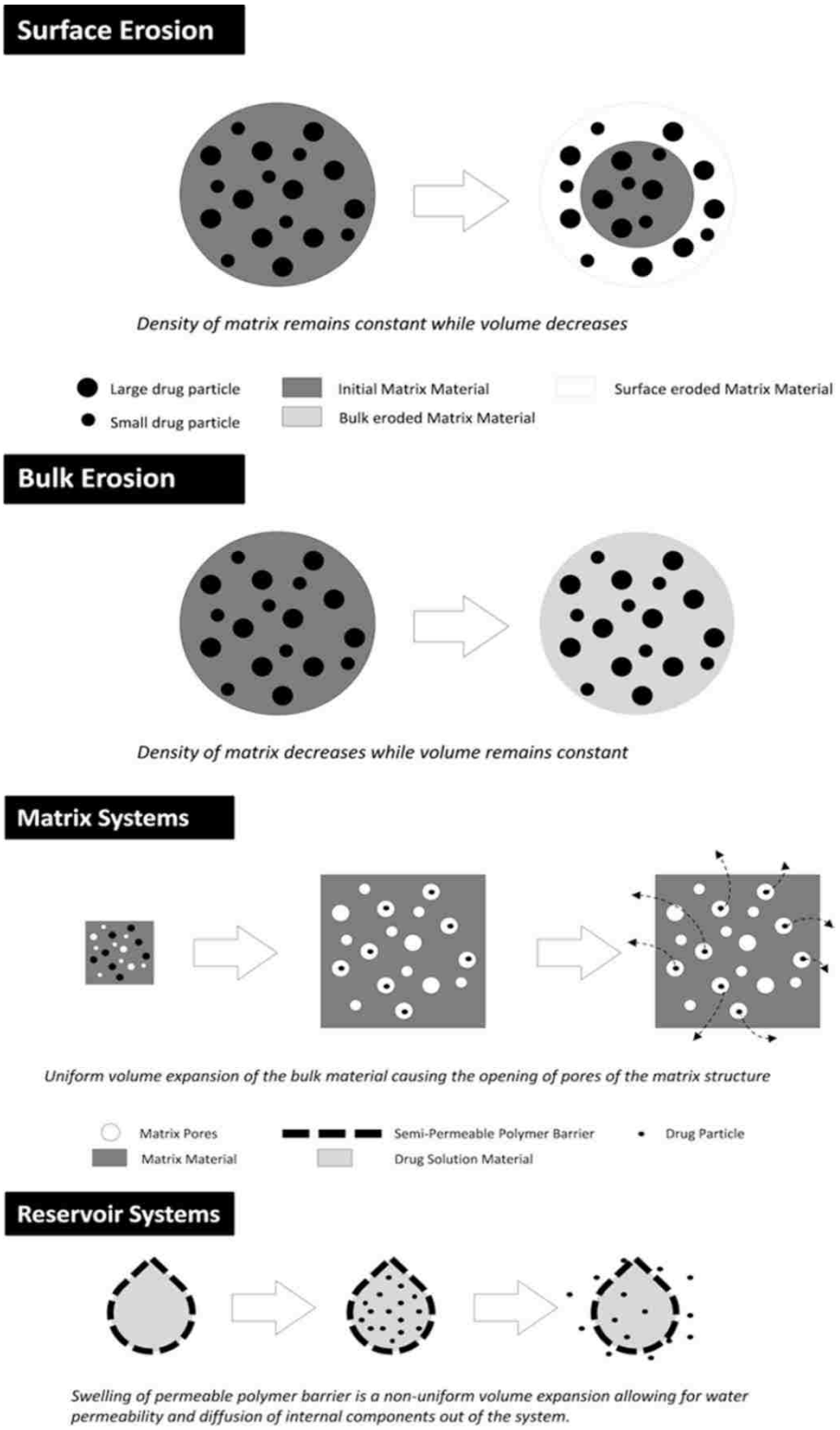


Figure 4.1. Schematic representation of degradation-controlled (surface erosion, bulk erosion) and diffusion-controlled (matrix-based, reservoir based) release systems for targeted drug delivery. Adapted from ref [128].

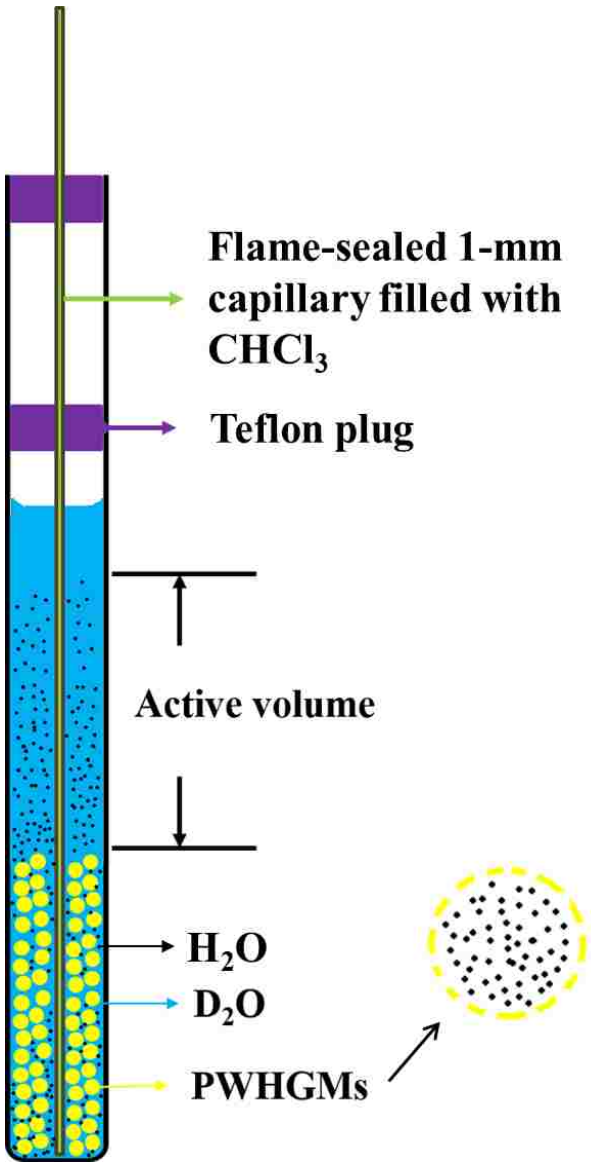


Figure 4.2 Schematic illustration of the sample distribution in the NMR tube for the kinetic release experiment. For this study, the microspheres are kept below the NMR active volume.

intensity during the course of the experiments. The changing intensity of the $H_2O$ peak is normalized to the intensity of the $CHCl_3$ peak from the capillary tube and plotted as a function of time in Figure 4.4.

The data plotted in Figure 4.4 represent a double-exponential raise to maximum curve as evaluated by a numerical fitting procedure to a 5-parameter double-exponential curve leading to the following equation:

$$I = 6.35 + 78\% \, (1 - exp \ (-0.048 \, t)) + 22\% \, (1 - exp \ (-0.0063 \, t)) \qquad (1)$$

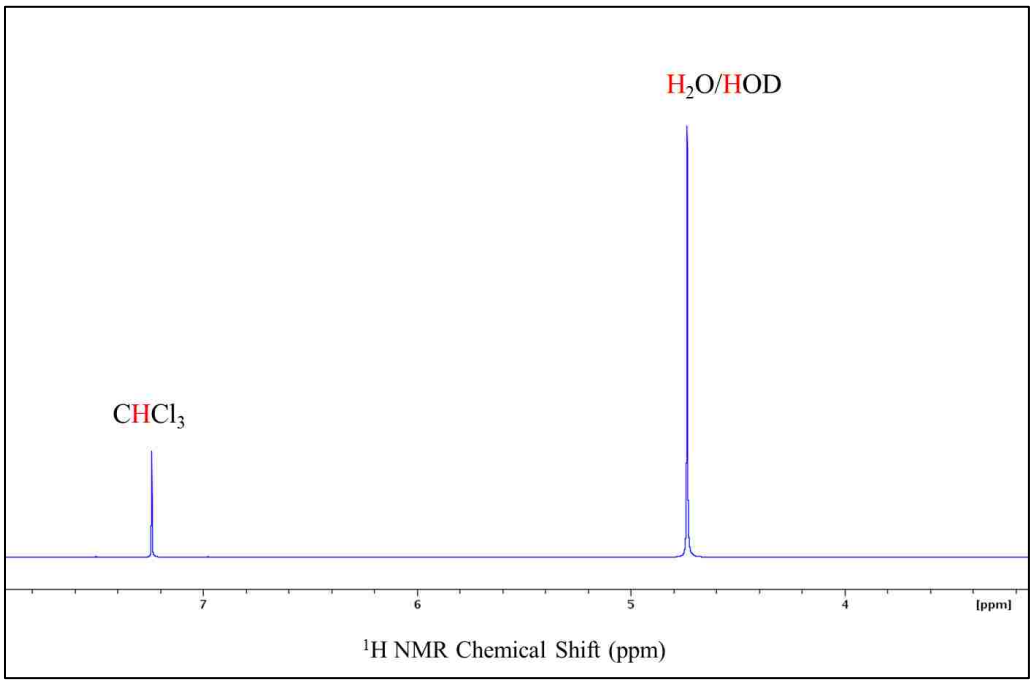


Figure 4.3. A typical $^1$H NMR spectrum recorded during the diffusion process of $H_2O$ into $D_2O$.

The best fit to the experimental data is included in Figure 4.4 as a line curve. It has a correlation coefficient of $R^2$ = 0.9977 and a standard error around 1%. The uncertainty in the starting point of the release relative to the first NMR spectrum (± 1 min) adds another 1% to the standard error. The individual parameters are interpreted as follows:

The curve has a constant intercept, which means that it does not start at zero intensity (intercept $I_0$ = 6.35). The intercept represents the 0.2% HOD impurity already present in the surrounding solvent ($D_2O$). The curve fit exhibits the combination of two

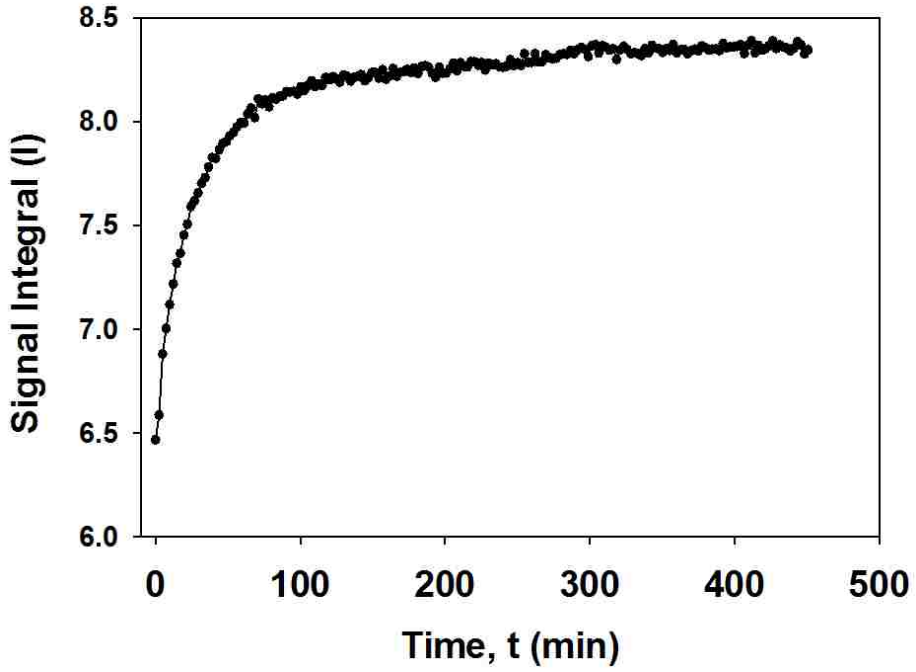


Figure 4.4. $^1H$ NMR signal intensity of HOD/$H_2O$ in $D_2O$ as a function of time.

exponential curves, where one applies to 78% (± 2%) of the released $H_2O$ and the other to the remaining 22% (± 2%). The 78% show a faster release with a time constant of about 18 - 20 minutes while the 22% of slower release have a time constant around 160 minutes. The two different release rates are may result from microspheres with the very different pore size distributions. As discussed in Section 2.1, there are two distinct ranges of pore sizes, one from 10 nm to 20 nm and another one from 50 nm to 75 nm. Because the largest dimension of an $H_2O$ molecule is only 0.275 nm, the sizes of any of the pores

in the microsphere walls largely exceeds the sizes of a $H_2O$ molecule. Thus, $H_2O$ is believed to move freely into and out of the pores. The significant differences in the pore sizes, however, still create a different physical barrier to the release of $H_2O$ molecules into the surrounding solution. Microspheres that have only small pores in the 10 to 20 nm range will need much longer to release their material into the surrounding solution. Hence, about 78% of the material inside the microspheres is released relatively fast through microspheres with large and small pores, while about 22% are released from microspheres with only small pores. It has been suggested that the slow release originates from material adsorbed on the surfaces of the pores (and the inner surface of the microsphere cavity); however, the microsphere shell account for only 5-10% of the entire microsphere volume (including the hollow cavity), so that this suggestion is not sufficient to explain the slow release of over 20% of the material. Repeating this release experiment showed similar results where the optimized curve-fit parameters fall well within the standard errors reported above.

This set of experiments demonstrates that the release time of materials from the PWHGMs is largely controlled by the size of the pores in the glass walls of the microspheres. This fact can be extremely helpful when designing microspheres as drug carries with a desired drug release rate. For example, when the desired release is preferred to be slow, the pore sizes must be limited to small openings. On the contrary, faster release times are achieved with larger pores. The combination of microspheres with only small pores with those that may have small and large pores can even be beneficial in combination therapies where an initial boost of medication is desirable for acute treatment and an additional slow release for long-term therapy. NMR spectroscopy has

shown to be a powerful technique to determine release properties of materials deposited in PWHGMs. The monitoring of quantitative data obtained from the released material in real time can provide information that assists in the design of further refined microspheres for even more specialized treatments and therapies.

# 5. CONCLUSION

In summary, three major goals were achieved in this dissertation by utilizing different analytical techniques to determine biological parameters. The combination of using various analytical methodologies has a profound effect on the biomedical studies, and thus leads to the future improvement of human health and care.

In the first paper, a novel dual-core micro-pH probe has been successfully developed and fabricated using a home-built double-fiber twisting and gravitational-stretching system. The probe was coated by a specific OrMoSils dye-doping method and applied for pH sensing in a microliter environment. The enhanced mechanical structure of the probe with fused double fibers successfully separated the excitation beam and emission light, thus providing the robust probe with reduced background noise and increased sensitivity. A linear correlation between pH and spectral peak intensity was found within a biologically meaningful pH range of 6.20 to 7.92 and a coefficient factor of 0.9834 was achieved. The probe's spatial resolution was then exemplarily tested and a resolution of at least 2 mm was clearly demonstrated in a cell + NPs exposure test. We finally applied this probe in a $TiO_2$ NP-induced cytotoxicity assay. Results revealed a concentration/time dependence of the NP's cytotoxicity. Results also demonstrated the probe's potential for fast, local and continuous monitoring of cellular events in a staining-free manner, which may greatly impact future quasi-single-cell and cell-heterogeneity-driven researches.

In the second paper, a targeted, quantitative HPLC-MS/MS method was developed for simultaneous determination of quinolinic acid, 4-hydroxybenzoic acid,

gentisic acid and α-ketoglutaric acid in urine, which has not been previously reported to the best of our knowledge. The newly developed method was validated by multiple conventional figures of merit including method detection limits (0.05 ng/mL to 1 ng/mL), spiked recovery studies that indicated high accuracy (88.6% - 114.8%) and reproducibility (0.4 – 9.3% RSD), and acceptable intraday variance (1.2% - 2.8% RSD) and interday variance (2.4% - 5.1%) The applicability of the newly developed method was further demonstrated in 27 urine specimens from healthy individuals in addition to several RCC patients. All four compounds were successfully quantified in urine samples at concentrations were in agreement with previous findings. Together these findings suggest the new method can be considered sensitive, selective, and highly accurate, enabling researchers to evaluate the clinical applicability of these four urinary markers for earlier RCC detection and diagnosis. Although higher concentration levels in RCC samples were observed in our small sample set, larger study populations will be required to generate statistically significant conclusions regarding the clinical applicability of these four compounds. We therefore anticipate this method to significantly benefit clinical researchers aiming to perform epidemiological studies for these four compounds and to elucidate their roles in disease.

In the third part, NMR spectroscopy was applied to characterize materials loaded into PWHGMs for applications of microspheres in controlled and targeted drug delivery system. It is the first known report of characterizing microspheres and their loaded materials with NMR spectroscopy. The information provided by the NMR spectra proved to be valuable to study the properties of PWHGMs and the materials loaded into them.

Thus NMR spectroscopy is a powerful analytical tool to assist in future designs and improvements of PWHGMs as carriers in targeted delivery of drugs or biomarkers.

Microspheres were first characterized with FESEM. Their proposed spherical structure, smooth outer surface, and central hollow cavity were observed and confirmed. Under high magnification, different size ranges of the pores in the glass walls of the microspheres became visible and quantifiable. The porous structure and hollow cavity of the microspheres demonstrated their proposed advantages over other glass materials. A vacuum-based loading system was established to fill the microspheres with target materials. The loading procedure was shown to be very effective without damaging to the integrity of the microspheres. Meanwhile, an effective washing procedure was also developed utilizing a solvent that is immiscible with the loaded material. A three-times washing process removed all residues of the loading material from the outside of the microspheres. NMR spectra of the supernatants confirmed the effectiveness of the washing procedures. The established loading and washing procedures were consistently applied in the later studies.

Three model studies were conducted to demonstrate the applicability of NMR spectroscopy in the characterization of the PWHGMs intended to be used as drug carriers. The first two model studies focused on obtaining NMR evidence of loaded n-dodecane and chloroform inside the microspheres. NMR peaks of the loaded materials could be distinguished from the peaks of the materials in the surrounding solution, which laid the foundation for further studies. A third model study used the hydrolysis of isopropyl acetate to provide chemical evidence that material from the inside of the microspheres exchanged with the surrounding environment. The formation of isopropanol was the

indicator of exchange of isopropyl acetate in the microspheres and concentrated $H_2SO_4$ in the surrounding solution. These NMR results for the first time provided both static and dynamic information of loaded materials in the microspheres.

The release kinetics of $H_2O$ in the cavities of microspheres into the surrounding solution of $D_2O$ provided further evidence of material exchange between microspheres and solution. A 5-parameter double-exponential curve fit of experimental signal intensity data as a function of time indicated two release rates with time constants of 18 - 20 minutes and about 160 minutes. The different release rates are attributed to microspheres with a significant difference in the pore size distribution. The results of this study are expected to further benefit the design of microspheres as drug and biomarker carriers in applications of targeted delivery system for medical and diagnostic applications in human health care.

# BIBLIOGRAPHY


1. Tomaszewski, M., et al., *High rates of non-adherence to antihypertensive treatment revealed by high-performance liquid chromatography-tandem mass spectrometry (HP LC-MS/MS) urine analysis.* Heart, 2014: p. heartjnl-2013-305063.

2. Thaysen-Andersen, M. and N.H. Packer, *Advances in LC–MS/MS-based glycoproteomics: getting closer to system-wide site-specific mapping of the N-and O-glycoproteome.* Biochimica et Biophysica Acta (BBA)-Proteins and Proteomics, 2014. **1844**(9): p. 1437-1452.

3. Gika, H.G., et al., *Current practice of liquid chromatography–mass spectrometry in metabolomics and metabonomics.* Journal of pharmaceutical and biomedical analysis, 2014. **87**: p. 12-25.

4. Zhao, Y.-Y. and R.-C. Lin, *UPLC–MS E application in disease biomarker discovery: the discoveries in proteomics to metabolomics.* Chemico-biological interactions, 2014. **215**: p. 7-16.

5. St Helen, G., et al., *Nicotine delivery, retention and pharmacokinetics from various electronic cigarettes.* Addiction, 2016. **111**(3): p. 535-544.

6. Wink, C.S., et al., *Lefetamine, a controlled drug and pharmaceutical lead of new designer drugs: synthesis, metabolism, and detectability in urine and human liver preparations using GC-MS, LC-MSn, and LC-high resolution-MS/MS.* Analytical and bioanalytical chemistry, 2015. **407**(6): p. 1545-1557.

7. Sanders, J.K., B.K. Hunter, and C. Griesinger, *Modern NMR spectroscopy.* Angewandte Chemie-English Edition, 1994. **33**(19): p. 1992-1993.

8. De Graaff, C. and M. Viergever, *Information processing in medical imaging*. 2013: Springer Science & Business Media.

9. Dunn, W.B., N.J. Bailey, and H.E. Johnson, *Measuring the metabolome: current analytical technologies.* Analyst, 2005. **130**(5): p. 606-625.

10. Zhang, A., et al., *Modern analytical techniques in metabolomics analysis.* Analyst, 2012. **137**(2): p. 293-300.

11. Kulasingam, V. and E.P. Diamandis, *Strategies for discovering novel cancer biomarkers through utilization of emerging technologies.* Nature clinical practice Oncology, 2008. **5**(10): p. 588-599.

12. Rajan, G., *Optical fiber sensors: advanced techniques and applications*. 2015: CRC press.

13. Booth, I.R., *Regulation of cytoplasmic pH in bacteria.* Microbiological reviews, 1985. **49**(4): p. 359.

14. Raven, J. and F. Smith, *The regulation of intracellular pH as a fundamental biological process.* Ion transport in plants, 2013: p. 271-278.

15. McBrian, M.A., et al., *Histone acetylation regulates intracellular pH.* Molecular cell, 2013. **49**(2): p. 310-321.

16. Busa, W. and R. Nuccitelli, *Metabolic regulation via intracellular pH.* American Journal of Physiology-Regulatory, Integrative and Comparative Physiology, 1984. **246**(4): p. R409-R438.

17. Boron, W.F., *Intracellular pH regulation*, in *Membrane transport processes in organized systems*. 1987, Springer. p. 39-51.

18. Orlowski, J. and S. Grinstein, *Diversity of the mammalian sodium/proton exchanger SLC9 gene family.* Pflügers Archiv, 2004. **447**(5): p. 549-565.

19. Organization, W.H., *Biomarkers in risk assessment: Validity and validation*. Vol. 222. 2001: WHO.

20. Stamey, T.A., et al., *Prostate-specific antigen as a serum marker for adenocarcinoma of the prostate.* New England Journal of Medicine, 1987. **317**(15): p. 909-916.

21. Hernández, J. and I.M. Thompson, *Prostate ‐ specific antigen: a review of the validation of the most commonly used cancer biomarker.* Cancer, 2004. **101**(5): p. 894-904.

22. Careri, M., et al., *Use of specific peptide biomarkers for quantitative confirmation of hidden allergenic peanut proteins Ara h 2 and Ara h 3/4 for food control by liquid chromatography–tandem mass spectrometry.* Analytical and bioanalytical chemistry, 2007. **389**(6): p. 1901-1907.

23. Rifai, N., M.A. Gillette, and S.A. Carr, *Protein biomarker discovery and validation: the long and uncertain path to clinical utility.* Nature biotechnology, 2006. **24**(8): p. 971-983.

24. Hanash, S.M., S.J. Pitteri, and V.M. Faca, *Mining the plasma proteome for cancer biomarkers.* Nature, 2008. **452**(7187): p. 571-579.

25. Hamid, O., et al., *Clinical activity, safety, and biomarkers of MPDL3280A, an engineered PD-L1 antibody in patients with locally advanced or metastatic melanoma (mM)*. 2013, American Society of Clinical Oncology.

26. Reddy, M.M., et al., *Identification of candidate IgG biomarkers for Alzheimer's disease via combinatorial library screening.* Cell, 2011. **144**(1): p. 132-142.

27. Horn, L., et al., *Clinical activity, safety and predictive biomarkers of the engineered antibody MPDL3280A (anti-PDL1) in non-small cell lung cancer (NSCLC): update from a phase Ia study*. 2015, American Society of Clinical Oncology.

28. Tan, H.T., et al., *Serum autoantibodies as biomarkers for early cancer detection.* FEBS journal, 2009. **276**(23): p. 6880-6904.

29. Smith, T.J., et al., *2006 update of recommendations for the use of white blood cell growth factors: an evidence-based clinical practice guideline.* Journal of Clinical Oncology, 2006. **24**(19): p. 3187-3205.

30. Jee, S.H., et al., *White blood cell count and risk for all-cause, cardiovascular, and cancer mortality in a cohort of Koreans.* American journal of epidemiology, 2005. **162**(11): p. 1062-1069.

31. Scher, H.I., et al., *Circulating tumour cells as prognostic markers in progressive, castration-resistant prostate cancer: a reanalysis of IMMC38 trial data.* The lancet oncology, 2009. **10**(3): p. 233-239.

32. Riethdorf, S., et al., *Detection of circulating tumor cells in peripheral blood of patients with metastatic breast cancer: a validation study of the CellSearch system.* Clinical cancer research, 2007. **13**(3): p. 920-928.

33. Hecht, S.S., *Tobacco carcinogens, their biomarkers and tobacco-induced cancer.* Nature Reviews Cancer, 2003. **3**(10): p. 733-744.

34. Mamas, M., et al., *The role of metabolites and metabolomics in clinically applicable biomarkers of disease.* Archives of toxicology, 2011. **85**(1): p. 5-17.

35. Qu, Q., et al., *Validation of biomarkers in humans exposed to benzene: urine metabolites.* American Journal of Industrial Medicine, 2000. **37**(5): p. 522-531.

36. Silva, M., et al., *Measurement of eight urinary metabolites of di (2-ethylhexyl) phthalate as biomarkers for human exposure assessment.* Biomarkers, 2006. **11**(1): p. 1-13.

37. Fernandis, A.Z. and M.R. Wenk, *Lipid-based biomarkers for cancer.* Journal of Chromatography B, 2009. **877**(26): p. 2830-2835.

38. Kuligowski, J., et al., *Analysis of lipid peroxidation biomarkers in extremely low gestational age neonate urines by UPLC-MS/MS.* Analytical and bioanalytical chemistry, 2014. **406**(18): p. 4345-4356.

39. Scola, G., et al., *Lipid peroxidation biomarkers in adolescents with or at high-risk for bipolar disorder.* Journal of affective disorders, 2016. **192**: p. 176-183.

40. Guillette, L., et al., *Steroid hormones as biomarkers of endocrine disruption in wildlife,* in *Environmental Toxicology and Risk Assessment: Standardization of Biomarkers for Endocrine Disruption and Environmental Assessment: 8th Volume*. 1999, ASTM International.

41. Linkov, F., Z. Yurkovetsky, and A. Lokshin, *Hormones as biomarkers: practical guide to utilizing luminex technologies for biomarker research.* Tumor Biomarker Discovery: Methods and Protocols, 2009: p. 129-141.

42. Piazza, J.R., et al., *Frontiers in the use of biomarkers of health in research on stress and aging.* The Journals of Gerontology Series B: Psychological Sciences and Social Sciences, 2010. **65**(5): p. 513-525.

43. Ozer, J., et al., *The current state of serum biomarkers of hepatotoxicity.* Toxicology, 2008. **245**(3): p. 194-205.

44. Regoli, F. and G. Principato, *Glutathione, glutathione-dependent and antioxidant enzymes in mussel, Mytilus galloprovincialis, exposed to metals under field and laboratory conditions: implications for the use of biochemical biomarkers.* Aquatic Toxicology, 1995. **31**(2): p. 143-164.

45. Akcha, F., et al., *Enzymatic biomarker measurement and study of DNA adduct formation in benzo [a] pyrene-contaminated mussels, Mytilus galloprovincialis.* Aquatic Toxicology, 2000. **49**(4): p. 269-287.

46. Srinivas, P.R., B.S. Kramer, and S. Srivastava, *Trends in biomarker research for cancer detection.* The lancet oncology, 2001. **2**(11): p. 698-704.

47. Camargo, M.M. and C.B. Martinez, *Biochemical and physiological biomarkers in Prochilodus lineatus submitted to in situ tests in an urban stream in southern Brazil.* Environmental toxicology and pharmacology, 2006. **21**(1): p. 61-69.

48. Vasan, R.S., *Biomarkers of cardiovascular disease.* Circulation, 2006. **113**(19): p. 2335-2362.

49. Thal, L.J., et al., *The role of biomarkers in clinical trials for Alzheimer disease.* Alzheimer disease and associated disorders, 2006. **20**(1): p. 6.

50. Henry, N.L. and D.F. Hayes, *Cancer biomarkers.* Molecular oncology, 2012. **6**(2): p. 140-146.

51. Kakkar, R. and R.T. Lee, *The IL-33/ST2 pathway: therapeutic target and novel biomarker.* Nature reviews Drug discovery, 2008. **7**(10): p. 827-840.

52. Monk, B.J., et al., *Salvage bevacizumab (rhuMAB VEGF)-based therapy after multiple prior cytotoxic regimens in advanced refractory epithelial ovarian cancer.* Gynecologic oncology, 2006. **102**(2): p. 140-144.

53. Srinivas, P.R., et al., *Proteomics for cancer biomarker discovery.* Clinical chemistry, 2002. **48**(8): p. 1160-1169.

54. Kong, A.T., et al., *MSFragger: ultrafast and comprehensive peptide identification in mass spectrometry-based proteomics.* Nature Methods, 2017.

55. Zhou, W., L.A. Liotta, and E.F. Petricoin, *Cancer metabolism and mass spectrometry-based proteomics.* Cancer letters, 2015. **356**(2): p. 176-183.

56. Storey, R., J. Fisher, and A. Smith, *1H-NMR metabonomic profiling for novel pancreaticobiliary biomarker discovery.* Pancreatology, 2015. **15**(3): p. S16.

57. Gil, R.B., et al., *1H NMR-based metabolite profiling workflow to reduce inter-sample chemical shift variations in urine samples for improved biomarker discovery.* Analytical and bioanalytical chemistry, 2016. **408**(17): p. 4683-4691.

58. Tiwari, G., et al., *Drug delivery systems: an updated review.* International journal of pharmaceutical investigation, 2012. **2**(1): p. 2.

59. Cho, K., et al., *Therapeutic nanoparticles for drug delivery in cancer.* Clinical cancer research, 2008. **14**(5): p. 1310-1316.

60. Popovic, N. and P. Brundin, *Therapeutic potential of controlled drug delivery systems in neurodegenerative diseases.* International journal of pharmaceutics, 2006. **314**(2): p. 120-126.

61. Gelperina, S., et al., *The potential advantages of nanoparticle drug delivery systems in chemotherapy of tuberculosis.* American journal of respiratory and critical care medicine, 2005. **172**(12): p. 1487-1490.

62. LaVan, D.A., T. McGuire, and R. Langer, *Small-scale systems for in vivo drug delivery.* Nature biotechnology, 2003. **21**(10): p. 1184-1191.

63. Ferrari, M., *Cancer nanotechnology: opportunities and challenges.* Nature Reviews Cancer, 2005. **5**(3): p. 161-171.

64. Langer, R., *Drug delivery abd targeting.* Nature, 1998. **392**(6679): p. 5-10.

65. Kisak, E., et al., *The vesosome-A multicompartment drug delivery vehicle.* Current medicinal chemistry, 2004. **11**(2): p. 199-219.

66. Xu, P., et al., *Targeted Charge‐Reversal Nanoparticles for Nuclear Drug Delivery.* Angewandte Chemie International Edition, 2007. **46**(26): p. 4999-5002.

67. Leporatti, S., *Halloysite Clay Nanotubes as Nano‐Bazookas for Drug Delivery.* Polymer International, 2017.

68. Sun, T., et al., *Engineered nanoparticles for drug delivery in cancer therapy.* Angewandte Chemie International Edition, 2014. **53**(46): p. 12320-12364.

69. Kipp, J., *The role of solid nanoparticle technology in the parenteral delivery of poorly water-soluble drugs.* International Journal of Pharmaceutics, 2004. **284**(1): p. 109-122.

70. Dobson, J., *Magnetic nanoparticles for drug delivery.* Drug development research, 2006. **67**(1): p. 55-60.

71. Parhi, P., C. Mohanty, and S.K. Sahoo, *Nanotechnology-based combinational drug delivery: an emerging approach for cancer therapy.* Drug discovery today, 2012. **17**(17): p. 1044-1052.

72. Rajput, M.S. and P. Agrawal, *Microspheres in cancer therapy.* Indian journal of cancer, 2010. **47**(4): p. 458.

73. Geschwind, J.F.H., et al., *Yttrium-90 microspheres for the treatment of hepatocellular carcinoma.* Gastroenterology, 2004. **127**(5): p. S194-S205.

74. Khajornjiraphan, N., N.A. Thu, and P.K.H. Chow, *Yttrium-90 microspheres: a review of its emerging clinical indications.* Liver cancer, 2015. **4**(1): p. 6-15.

75. Lewandowski, R.J., et al., *Transcatheter intraarterial therapies: rationale and overview.* Radiology, 2011. **259**(3): p. 641-657.

76. Gil‐Alzugaray, B., et al., *Prognostic factors and prevention of radioembolization‐induced liver disease.* Hepatology, 2013. **57**(3): p. 1078-1087.

77. Campbell, A.M., I.H. Bailey, and M.A. Burton, *Analysis of the distribution of intra-arterial microspheres in human liver following hepatic yttrium-90 microsphere therapy.* Physics in medicine and biology, 2000. **45**(4): p. 1023.

78. Doughty, J., et al., *Intra-arterial administration of adriamycin-loaded albumin microspheres for locally advanced breast cancer.* Postgraduate medical journal, 1995. **71**(831): p. 47-49.

79. Chaurasia, M., et al., *Cross-linked guar gum microspheres: A viable approach for improved delivery of anticancer drugs for the treatment of colorectal cancer.* Aaps Pharmscitech, 2006. **7**(3): p. E143.

80. Azouz, S.M., et al., *Prevention of local tumor growth with paclitaxel-loaded microspheres.* The Journal of thoracic and cardiovascular surgery, 2008. **135**(5): p. 1014-1021.

81. Kumagai, S., et al., *Improvement of Intraperitoneal Chemotherapy for Rat Ovarian Cancer Using Cisplatin‐containing Microspheres.* Japanese journal of cancer research, 1996. **87**(4): p. 412-417.

82. Le Visage, C., et al., *Efficacy of paclitaxel released from bio-adhesive polymer microspheres on model superficial bladder cancer.* The Journal of urology, 2004. **171**(3): p. 1324-1329.

83. Hench, L.L., *The story of Bioglass®.* Journal of Materials Science: Materials in Medicine, 2006. **17**(11): p. 967-978.

84. Wren, A.W., *Vitreous Materials for Dental Restoration and Reconstruction*, in *Biocompatible Glasses*. 2016, Springer. p. 203-225.

85. Hench, L.L., *Bioactive Glass Bone Grafts: History and Clinical Applications.* Handbook of Bioceramics and Biocomposites, 2016: p. 23-33.

86. Baino, F., S. Fiorilli, and C. Vitale-Brovarone, *Bioactive glass-based materials with hierarchical porosity for medical applications: Review of recent advances.* Acta biomaterialia, 2016. **42**: p. 18-32.

87. Chen, S., et al., *In vitro stimulation of vascular endothelial growth factor by borate-based glass fibers under dynamic flow conditions.* Materials Science and Engineering: C, 2017. **73**: p. 447-455.

88. Yang, Q., et al., *In vitro study of improved wound-healing effect of bioactive borate-based glass nano-/micro-fibers.* Materials Science and Engineering: C, 2015. **55**: p. 105-117.

89. Hench, L.L. and J.M. Polak, *Third-generation biomedical materials.* Science, 2002. **295**(5557): p. 1014-1017.

90. Jiang, S., et al., *Amino-functionalized mesoporous bioactive glass for drug delivery.* Biomedical Materials, 2017.

91. Schumacher, M., et al., *Calcium phosphate bone cement/mesoporous bioactive glass composites for controlled growth factor delivery.* Biomaterials Science, 2017. **5**(3): p. 578-588.

92. Urist, M.R., *Biodegradable porous ceramic delivery system for bone morphogenetic protein*. 1986, Google Patents.

93. Wicks, G., L. Heung, and R. Schumacher, *Microspheres and microworlds.* American Ceramic Society Bulletin, 2008. **87**(6): p. 23.

94. Sexton, W., *Porous Wall, Hollow Glass Microspheres*. 2012, SRS.

95. Newell, J., S. Patankar, and D. Edwards, *Porous microspheres as additives in lead–acid batteries.* Journal of Power Sources, 2009. **188**(1): p. 292-295.

96. Liu, J., et al., *Morphological and structural evolution of mesoporous silicas in a mild buffer solution and lysozyme adsorption.* Langmuir, 2007. **23**(13): p. 7255-7262.

97. Wu, Z., et al., *Hematite hollow spheres with a mesoporous shell: controlled synthesis and applications in gas sensor and lithium ion batteries.* The Journal of Physical Chemistry C, 2008. **112**(30): p. 11307-11313.

98. Heung, L.K., R.F. Schumacher, and G.G. Wicks, *Hollow porous-wall glass microspheres for hydrogen storage*. 2010, Google Patents.

99. Thompson, F., G. Wicks, and G. Crawford. *Porous-wall Hollow Glass Microspheres for Security Printing Applications*. in *NIP & Digital Fabrication Conference*. 2015. Society for Imaging Science and Technology.

100. Li, S., et al., *Porous-wall hollow glass microspheres as novel potential nanocarriers for biomedical applications.* Nanomedicine: Nanotechnology, Biology and Medicine, 2010. **6**(1): p. 127-136.

101. Wei, W., et al., *Preparation of hierarchical hollow CaCO3 particles and the application as anticancer drug carrier.* Journal of the American Chemical Society, 2008. **130**(47): p. 15808-15810.

102. Moosavi, S.S. and P. Alizadeh, *Effect of acid leaching time on pore diameter and volume of porous hollow glass microspheres.* Materials Letters, 2016. **167**: p. 98-101.

103. Zhu, Y., et al., *Preparation of novel hollow mesoporous silica spheres and their sustained-release property.* Nanotechnology, 2005. **16**(11): p. 2633.

104. Cai, Y., et al., *Porous microsphere and its applications.* International journal of nanomedicine, 2013. **8**: p. 1111.

105. Lepre, C.A., J.M. Moore, and J.W. Peng, *Theory and applications of NMR-based screening in pharmaceutical research.* Chemical reviews, 2004. **104**(8): p. 3641-3676.

106. Malet-Martino, M. and U. Holzgrabe, *NMR techniques in biomedical and pharmaceutical analysis.* Journal of pharmaceutical and biomedical analysis, 2011. **55**(1): p. 1-15.

107. Günther, H., *NMR spectroscopy: basic principles, concepts and applications in chemistry*. 2013: John Wiley & Sons.

108. Williams, T.J., et al., *An Inversion Recovery NMR Kinetics Experiment.* Journal of chemical education, 2011. **88**(5): p. 665.

109. Gossert, A.D. and W. Jahnke, *NMR in drug discovery: A practical guide to identification and validation of ligands interacting with biological macromolecules.* Progress in nuclear magnetic resonance spectroscopy, 2016. **97**: p. 82-125.

110. Shaw, D., et al., *IUPAC Solubility Data Series: Hydrocarbons with Water and Seawater, Part II: Hydrocarbons C8 to C36*. 1989, Pergamon, Oxford.

111. Mackay, D., et al., *Relationships between aqueous solubility and octanol-water partition coefficients.* Chemosphere, 1980. **9**(11): p. 701-711.

112. Ineman, J. and J. Schultz, *Emulsifiers 101: Who says oil and water don't mix?* Tribology & Lubrication Technology, 2013. **69**(9): p. 32.

113. O'Neil, M., et al., *éditeurs. The Merck Index: An Encyclopedia of Chemicals, Drugs, and Biologicals, 13 e édition. Whitehouse Station (NJ): Merck & Co*. 2001, Inc.

114. O'Neil, M.J., *The Merck index: an encyclopedia of chemicals, drugs, and biologicals*. 2013: RSC Publishing.

115. Cavcar, M., *The international standard atmosphere (isa).* Anadolu University, Turkey, 2000. **30**: p. 9.

116. Di, L. and E.H. Kerns, *Drug-like properties: concepts, structure design and methods from ADME to toxicity optimization*. 2015: Academic Press.

117. Kerns, E.H. and L. Di, *Pharmaceutical profiling in drug discovery.* Drug discovery today, 2003. **8**(7): p. 316-323.

118. Forbes, G.B., *Human body composition: growth, aging, nutrition, and activity*. 2012: Springer Science & Business Media.

119. Marieb, E.N., et al., *Anatomie et physiologie humaines (4e éd.).* Saint-Laurent (QC), éditions du Renouveau pédagogique, 2010.

120. Zega, J.A., *Spin-lattice relaxation in normal alkanes at elevated pressures*. 1991, Rice University.

121. Kumar, M., *Nano and microparticles as controlled drug delivery devices.* J. Pharm. Pharm. Sci, 2000. **3**(2): p. 234-258.

122. Siepmann, J., et al., *HPMC-matrices for controlled drug delivery: a new model combining diffusion, swelling, and dissolution mechanisms and predicting the release kinetics.* Pharmaceutical Research, 1999. **16**(11): p. 1748-1756.

123. Colombo, P., et al., *Swellable matrices for controlled drug delivery: gel-layer behaviour, mechanisms and optimal performance.* Pharmaceutical science & technology today, 2000. **3**(6): p. 198-204.

124. Lai, C.-Y., et al., *A mesoporous silica nanosphere-based carrier system with chemically removable CdS nanoparticle caps for stimuli-responsive controlled release of neurotransmitters and drug molecules.* Journal of the American Chemical Society, 2003. **125**(15): p. 4451-4459.

125. Gong, C.Y., et al., *Thermosensitive PEG–PCL–PEG hydrogel controlled drug delivery system: sol–gel–sol transition and in vitro drug release study.* Journal of pharmaceutical sciences, 2009. **98**(10): p. 3707-3717.

126. Cuna, M., J.V. Jato, and D. Torres, *Controlled-release liquid suspensions based on ion-exchange particles entrapped within acrylic microcapsules.* International Journal of Pharmaceutics, 2000. **199**(2): p. 151-158.

127. Guo, X., R.K. Chang, and M.A. Hussain, *Ion‐exchange resins as drug delivery carriers.* Journal of pharmaceutical sciences, 2009. **98**(11): p. 3886-3902.

128. Holowka, E. and S.K. Bhatia, *Drug Delivery: Materials Design and Clinical Perspective*. 2014: Springer.

129. von Burkersroda, F., L. Schedl, and A. Göpferich, *Why degradable polymers undergo surface erosion or bulk erosion.* Biomaterials, 2002. **23**(21): p. 4221-4231.

130. Kamaly, N., et al., *Degradable controlled-release polymers and polymeric nanoparticles: mechanisms of controlling drug release.* Chemical reviews, 2016. **116**(4): p. 2602-2663.

131. Kulkarni, R.K., et al., *Biodegradable poly (lactic acid) polymers.* Journal of Biomedical Materials Research Part A, 1971. **5**(3): p. 169-181.

132. Fredenberg, S., et al., *The mechanisms of drug release in poly (lactic-co-glycolic acid)-based drug delivery systems—a review.* International journal of pharmaceutics, 2011. **415**(1): p. 34-52.

133. Allcock, H.R., et al., *Contemporary polymer chemistry*. 2003: Pearson/Prentice Hall Upper Saddle River, N. J.

134. Xu, Q., et al., *Mechanism of drug release from double-walled PDLLA (PLGA) microspheres.* Biomaterials, 2013. **34**(15): p. 3902-3911.

135. Lu, L., et al., *In vitro and in vivo degradation of porous poly (DL-lactic-co-glycolic acid) foams.* Biomaterials, 2000. **21**(18): p. 1837-1845.

136. Mittal, G., et al., *Estradiol loaded PLGA nanoparticles for oral administration: effect of polymer molecular weight and copolymer composition on release behavior in vitro and in vivo.* Journal of Controlled Release, 2007. **119**(1): p. 77-85.

137. Stevenson, C.L., J.T. Santini, and R. Langer, *Reservoir-based drug delivery systems utilizing microtechnology*. Advanced drug delivery reviews, 2012. **64**(14): p. 1590-1602.

# VITA

Sisi Chen was born in Beijing, China. She completed her primary and secondary education in Beijing, China. In 2008, she was admitted by School of Chemical Biology and Pharmaceutical Sciences, Capital Medical University, Beijing, China. After she received her B.S. degree in 2012, she joined Missouri University of Science and Technology to continue her study and received her Master of Science with thesis in Chemistry from the Missouri University of Science and Technology in December 2015. Then she joined Dr. Klaus Woelk's research group for further research and study, where she received her Ph.D. degree in Chemistry in July 2017 with seven peer reviewed publications and eighteen conference presentations.